Cockpit Design and Integration into the Flying V

R. van der Pluijm

Technische Universiteit Delft

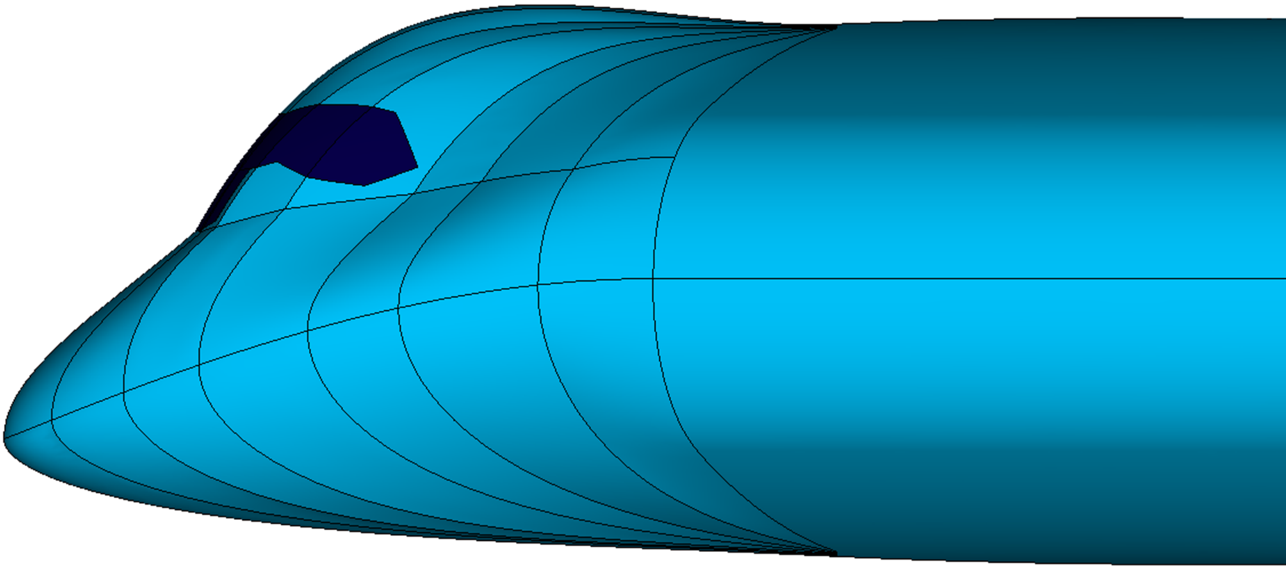

Delft University of Technology

Challenge the future

COCKPIT DESIGN AND INTEGRATION INTO THE FLYING V

by

R. van der Pluijm

in partial fulfillment of the requirements for the degree of

Master of Science
in Aerospace Engineering

at the Delft University of Technology,
to be defended publicly on Thursday February 4, 2021 at 01:00 PM.

Equivalent number of words:	28,362	
Supervisor:	Dr. ir. R. Vos	TU Delft
Thesis committee:	Dr. ir. G. la Rocca,	TU Delft
	Dr. R. Dwight,	TU Delft

SUMMARY

The Flying V is an innovative new aircraft concept currently being developed by the faculty of Aerospace Engineering at Delft University of Technology. This aircraft is a flying wing having a large sweep on the inner section, and a small sweep angle at the outer, giving the aircraft its characteristic V shape. An early cockpit design has been made, however, it does not satisfy a number of requirements. Additionally, the root effect, present due to the high inboard sweep angle, creates the need too adapt the root airfoil. The objective of this research is to create a parameterisation of the cockpit and aft center fairing for the Flying V that includes an integration of pilot anthropometry, satisfies visibility certification constraints, ensures positioning of nose landing gear and radar, while ensuring a high probability of good aerodynamic performance and being able to be used in an aerodynamic design optimization. To accomplish this, a parameterisation of the cockpit and aft center fairing models is made. Both consist of a number of cross-sectional profiles which are placed on a rail. After the curves are positioned, a loft will be made. The geometry that results is then inserted in the original wing geometry to fuse both shapes, forming the outer mold line. After this, constraints are applied on the cockpit model, consisting of those imposed by pilot anthropometry, pilot visibility certification, and the positioning of the nose landing gear and weather radar. This allowed the model to ensure that enough room was provided for the separate components, but also that the pilot can see the runway during landing. Lastly, the geometrical model is coupled with an aerodynamic model to analyse the aerodynamic performance.

A qualitative case study has been performed by means of three cases. First is a case where the root airfoil is changed such that it complies with a set of measures that can be taken to reduce the root effect. The purpose of this model was purely aerodynamic. The lift generated at the root was increased by 11%, however, the increase in lift to drag ratio of this configuration was 0.39%, a small increase relative to the original wing geometry. The second case displayed a successful integration of the cockpit in the wing geometry. All constraints imposed on the cockpit model were satisfied, while the lift generated at the root was decreased by 20%. The lift to drag ratio of the total aircraft configuration was decreased by 0.8%. The third and final case included only the aft center fairing to demonstrate an increase of 13.5% in lift at the root, resulting in a total lift to drag increase of the aircraft of 0.94%. This displays the potential to increase the aerodynamic performance of the Flying V, however, to exploit this potential an optimization might need to be performed.

Finally, the robustness of the geometrical model is analysed by taking a large number of samples from a defined sample space, and determining the number of samples that can successfully generate a geometry. The robustness for the cockpit outer mold line generation consists of two parts. The first is an accurate geometrical model which follows the defined rail. This model had a robustness of 20.3% Second is a less accurate geometrical model that does not always follow the defined rail as accurately. This model is intended for coarse optimizations and has a robustness of 50.4%. Lastly, the aft center fairing had a robustness of 39.9%. A robustness of 40% is rather low and care must be taken when optimizing the models, that for over half of the sample domain no geometry can be generated.

PREFACE

This document serves as the final part of my Master degree in Flight Performance at the faculty of Aerospace Engineering at Delft University of Technology. It has been a long road, and a lot has happened since I started my studies in Delft. I have learnt a lot, and have grown personally. For this I would like to thank a number of people in this traditional section.

And even though it is tradition to start with the thesis supervisor, I feel like this person has thought me most of what I know in the field of aerospace engineering. Yes, Roelof Vos, I am talking about you. In the classroom I followed your lectures on (combat) aircraft design, but you have also helped me get that awesome internship at the National Aerospace Laboratory. Your insights and great advice have helped me a lot during my thesis, for which I want to thank you, we will stay in touch. Besides Roelof, I want to thank my friends from the FPP office, Kar Chun, Stanley, Marleen, you have helped me when I got stuck, and we had great fun together when we could. Not only my friends at the faculty deserve my thanks, also my friends from all around the world, from Breda to Varna and Tokyo and back. The Bulgarian company, you wonderful gents have introduced me to a great cuisine, culture and I want to say to you as well, blagodarya priyateli. A special thanks to the gentlemen from the Excellent Server, especially Kevin, Phat, Danny, Huy and Alex. You always found a way to get me on Interesting ideas, have a laugh, and provide some well earned distraction from time to time. Now last, but certainly not least, I really want to thank my mom and dad for their never ending support, love and care. There is nobody that I respect and love more than the two of you, you always have my back, and I want to thank you for that.

Reader, please enjoy the report you are about to read. I have been working towards this for a long time.

R. van der Pluijm
Delft, January 2021

CONTENTS

List of Figures ix

List of Tables xi

1 Introduction 1
- 1.1 Problem indication 2
- 1.2 Problem statement 4
- 1.3 Scope of the study 4
- 1.4 Research method 4
- 1.5 Relevance 5
- 1.6 Thesis outline 5

2 Model Requirements 7
- 2.1 Compatibility and integration in previous work 7
- 2.2 Root airfoil 7
- 2.3 Optimization 8

3 Geometrical Model 9
- 3.1 Outer Mold Line 10
  - 3.1.1 Shape Insertion Method 10
  - 3.1.2 Cockpit parameterisation 11
  - 3.1.3 Fairing parameterisation 16
  - 3.1.4 Robustness 20
- 3.2 Cockpit constraints 22
  - 3.2.1 Pilot compartment view 23
  - 3.2.2 Pilot Anthropometry 27
  - 3.2.3 Nose Landing Gear 28
  - 3.2.4 Radar 29

4 Aerodynamic Analysis 31
- 4.1 Inviscid method 31
  - 4.1.1 Mesh generation 31
  - 4.1.2 Configuration 32
  - 4.1.3 Verification 33
- 4.2 Viscous method 34
  - 4.2.1 Friction coefficient 34
  - 4.2.2 Form factor 35
  - 4.2.3 Profile drag coefficient 35
  - 4.2.4 Limitations 35
- 4.3 Root effect 36

5 Results 37
- 5.1 Robustness 37
- 5.2 Application of the Model 38
  - 5.2.1 Case I: Root Effect 38
  - 5.2.2 Case II: Cockpit Integration 41
  - 5.2.3 Case III: Center Fairing Integration 44

6 Conclusion and Recommendations 47
- 6.1 Conclusion 47
- 6.2 Recommendations 48

A Appendix A: UML class diagram 49

B Appendix B: Robustness Design Space Bounds 51

C Appendix C: Anthropometric Data 53

D Appendix D: Mesh Convergence Settings and Results 55

E Appendix E: Design Space Impression 57

F Appendix F: Case Input Data 63
- F.1 Case I: Root Effect . . . 63
- F.2 Case II: Cockpit Integration . . . 64
- F.3 Case III: Fairing Integration . . . 64

G Appendix G: Large contour plots 65

Bibliography 69

LIST OF FIGURES

1.1 Examples of blended wing bodies and their cockpits 2
1.2 Flying V with an early cockpit design [1] 2
1.3 Results from an earlier optimization performed by Faggiano (after [3]) 3
1.4 The Aérospatiale/BAC Concorde with its droop nose lowered to provide the pilots a higher over-nose angle 3

3.1 UML class diagram of the Flying V with integrated cockpit and fairing 9
3.2 Shape insertion method 10
3.3 UML class diagram of the cockpit geometric model 11
3.4 Flying V cockpit buildup with the cross-sectional components indicated with thick blue lines and the rail indicated by the thick cyan line 11
3.5 Top-view of the parameterisation for the cockpit and center fairing outer mold lines 12
3.6 Rail curve definition as seen in the xy-plane and the yz-plane. 13
3.7 Cockpit cross-section curve definition together with the definition of the design eye point (DEP) 14
3.8 The cockpit cross-sections are placed equispaced on the rear rail at an angle ϕ_{cockpit} defined by the parameter $f_{cockpit}$ and the sweep angle Λ 15
3.9 Lofting of the cockpit shell. It is composed of multiple panels that are each constituted of three separate lofts 16
3.10 UML class diagram of the center fairing geometrical model 17
3.11 Fairing geometry definition with the cross-sectional components indicated with thick blue lines and the rail indicated by the thick cyan line 17
3.12 Cross-section used for the generation of the center fairing. The points $p_{\text{f,top}}$ and $p_{\text{f,bottom}}$ are connected to the main wing geometry where the curves are required to follow the local tangent 19
3.13 Positioning of center fairing cross-sections. Where $l_{\text{f,section}}$ is the length along the trailing edge rail of the fairing, and ϕ_{fairing} is the angle at which the cross-sections are oriented. 19
3.14 Interpolated fairing cross-sections (red) made from the basis cross-section curves (dark blue) placed along the trailing edge rail 20
3.15 A transition surface is required between the fairing shell and the remaining wing geometry in order to prevent a gap from occurring 21
3.16 Latin hypercube samping (LHS). All points are spread over the rows and columns so that no two points are in the same interval 22
3.17 UML class diagram of the flightdeck constraints 22
3.18 Minimum view angles from the design eye point 23
3.19 Required view angle at the pilot seat during landing 24
3.20 Pilot position with respect to the aircraft lowest point 25
3.21 The minimum required windshield is made using the common surface between the solid pilot view-field and the cockpit shell 26
3.22 Realistic windshields using different start and end heights, as well as changing center points as seen from the front of the aircraft 26
3.23 An example of a pilot model (blue) including a 30cm headroom margin (green) 27
3.24 Positioning of the design eye point, cockpit floor, nose landing gear and radar antenna 29

4.1 A mesh generated for the Flying V with integrated cockpit and center fairing using a low element count 32
4.2 Computational domain used in the CFD calculations showing the three categories of boundaries: the outer domain, symmetry wall and the object (Flying V) 33
4.3 Grid convergence carried out for the original Flying V, showing the convergence of the inviscid drag coefficient computed by SU2 against the amount of volume elements in the grid. The error is relative to the result of the finest mesh 33

4.4 A reattached nose and center fairing to the base geometry used in this research 34

5.1 Robustness sample study for the cockpit and center fairing geometry using LHS sampling. The cockpit robustness is shown with the try_fix option set on or off 37
5.2 Change in camber line required as per [14], together with the original and achieved camber . . 39
5.3 Design of the cockpit and center fairing when resolving the airfoil changes required to reduce the root effect 39
5.4 Pressure coefficient plot for the Flying V using an adapted root airfoil to reduce the root effect (M=0.85, h=13,000m, $C_{L_{\text{ref}}}$=0.266) 40
5.5 Isobars for the original geometry and the geometry using an adapted airfoil to satisfy the airfoil changes required to reduce the root effect (M=0.85, h=13,000m, $C_{L_{\text{ref}}}$=0.266) 41
5.6 Drag coefficient and lift distribution over the halfspan of the original Flying V geometry (blue), and the Flying V where the root airfoil is adapted to reduce the root effect (orange), a cockpit is integrated (green) and with an integrated center fairing (red) (M=0.85, h=13,000m, $C_{L_{\text{ref}}}$=0.266) 41
5.7 The cockpit design integrated in the original geometry used for the second case 42
5.8 View angles attained from the design eye point at the captain's seat 42
5.9 Cross section of the cockpit showing the pilots, floor, nose landing gear and radar installation . 43
5.10 Pressure coefficient plot for the Flying V with integrated cockpit design (M=0.85, h=13,000m, $C_{L_{\text{ref}}}$=0.266) 43
5.11 Close up of the 3D aerodynamic results for the integrated cockpit design (M=0.85, h=13,000m, $C_{L_{\text{ref}}} = 0.266$) 44
5.12 The center fairing design integrated in the original geometry used for the third case 45
5.13 Pressure coefficient plot for the Flying V with integrated center fairing design (M=0.85, h=13,000m, $C_{L_{ref}} = 0.266$) 45
5.14 Aerodynamic results for the Flying V with integrated center fairing 46

G.1 Isobars for the original geometry (M=0.85, h=13,000m, $c_{L_{\text{ref}}} = 0.266$) 65
G.2 Isobars for the first case geometry, using an adapted airfoil to satisfy the airfoil changes required to reduce the root effect (M=0.85, h=13,000m, $c_{L_{\text{ref}}} = 0.266$) 66
G.3 Close up of the pressure contours for the integrated cockpit design (M=0.85, h=13,000m, $c_{L_{\text{ref}}} = 0.266$) 66
G.4 Close up of the Mach contours for the integrated cockpit design (M=0.85, h=13,000m, $c_{L_{\text{ref}}} = 0.266$) 67
G.5 Aerodynamic results for the Flying V with integrated center fairing (M=0.85, h=13,000m, $C_{L_{\text{ref}}} = 0.266$) 67
G.6 Aerodynamic results for the Flying V with integrated center fairing (M=0.85, h=13,000m, $C_{L_{\text{ref}}} = 0.266$) 68

LIST OF TABLES

3.1 Parameters used for the cockpit planform . . . 13
3.2 Parameters used for the cross-section definition. . . . 15
3.3 Parameters used to define the planform of the center fairing . . . 18
3.4 Parameters used in the definition of the center fairing cross-section . . . 18

4.1 Parameters used to create a mesh with their default value and element to which these apply . . 32
4.2 Parameters used for aerodynamic validation where the cockpit and fairing domains are cut and reinserted into the cut geometry. . . . 34

5.1 Various airfoil parameters for the root airfoil of the original and adapted geometry and the goal set by the root effect equations described above . . . 39
5.2 Results of the aerodynamic analyses for multiple cases. Percentages are relative to the original case . . . 46

B.1 Design space bounds for parameters used to determine the robustness of the cockpit outer mold line . . . 51
B.2 Design space bounds for parameters used to determine the robustness of the center fairing outer mold line . . . 51

C.1 Anthropometric data from the Human Factors Design Guide [24] . . . 53
C.2 Anthropometric data from Man-System Integration Standards [25] . . . 54

D.1 Mesh control values used for the mesh convergence together with the results these have produced. The error is defined as the drag coefficient of a mesh divided by the drag coefficient of the finest mesh . . . 55

F.1 Cockpit parameters for the Flying V with adaptations made to reduce the root effect (first case of the results chapter) . . . 63
F.2 Fairing parameters for Flying V with adaptations made to reduce the root effect (first case of the results chapter) . . . 63
F.3 Cockpit parameters for the Flying V using the integrated cockpit (second case of the results chapter) . . . 64
F.4 Parameters used to describe the center fairing for the Flying V using the integrated center fairing (third case of the results chapter) . . . 64

NOMENCLATURE

Roman

a	free parameter of a rail
b	span or spanwise length
c	chord length
C_p	pressure coefficient
C_D	aircraft drag coefficient
C_f	friction coefficient
C_L	aircraft lift coefficient
C_{D_p}	aircraft profile drag coefficient
c_{d_p}	strip profile drag coefficient
f	fraction of a length or angle used to position a cross-section
f	optimization function
g	inequality constraint
h	altitude
h	equality constraint
h	geometric height
l	geometric length
M	Mach number
N	number or an amount
p	a free parameter for one of the cockpit or fairing cross-section curves
R	Reynolds number
R	vertical displacement of the rail at the root
r	robustness
R_cutoff	cutoff Reynolds number
t/c	thickness to chord ratio
V	Volume
V	approach velocity
X	design/sample space
x_cockpit	x-coordinate of the cockpit end
z	z-coordinate

z_{Λ_1}	downward z-coordinate of the camber line
F	Female
M	Male

Greek

α	angle of attack
Δx	change in location of the thickest point in fraction of the chord
δ_{fairing}	aft displacement of the trailing edge of the center fairing
ϵ	error between two values
Λ	sweep angle
ϕ	angle of a curve at a specified point
ϕ	sweep angle
Φ_{end}	angle between the end of the fairing and the free-stream direction
τ	reduction factor for the root effect
θ	pitch angle or twist angle

Subscripts

Λ_1	indicating a value of the root airfoil after adaptation for the root effect
aft	the element located at the highest x-coordinate of a set
approach	property during landing
bottom	at the bottom of a cross-section curve
cockpit	indicating a variable is related to the cockpit
DEP	indicating the design eye point
e	effective
end	end point or value
fairing	indicating a variable is related to the fairing
feasible	indicating a feasible design
front	the element located at the lowest x-coordinate of a set
inv	inviscid component
landing	related to main landing gear
LE	leading edge
NLG	variable related to the nose landing gear
nose	nose point of the cockpit
rail	indicating a variable is related to a rail
ref	reference value used for setting a goal for the CFD
s	at the outboard section

section	indicating a variable is related to a section
start	start point or value
top	at the top of a cross-section curve
view	view angle or overnose angle
viewpoint	point located on the windshield ahead of the pilot
visc	viscous component
window	indicating a variable is related to the window point

Superscripts

n	indicating a cross-section out of a set
n	indicating dimensionality
fine	the finest mesh

1

INTRODUCTION

The design of the Flying V started as a thesis in Germany in the hands of Benad [1]. This aircraft had shown the potential to be more efficient in flight than its reference aircraft, the A350-900. Having a design lift over drag ratio that is 10% higher, and being 2% lighter, than the tube-and-wing aircraft, the flying wing has drawn the attention of the faculty of Aerospace Engineering at Delft University of Technology. Here, research continues on this new aircraft concept in the field of engine integration [2], aerodynamics [3], structures [4, 5] and wind tunnel tests [6, 7]. Faggiano has worked on a parameterisation of the Flying V which he optimised [3]. An improvement on this parameterisation was recently proposed by Hillen [8]. This improvement lies mainly in making the resulting shape of the Flying V fit for manufacturing, and a main difference was found in the orientation of the defining surface kinks, with as a result a more consistent design where the structural efficiency was ensured by using oval cabin sections.

A number of studies have been performed in the past in which the design of the front fuselage and cockpit of an aircraft were presented. One of these is a research performed on the D8[9], a double bubble aircraft featuring a complex but non-round fuselage. Here, a cockpit was designed with the pilot visibility and weather radar allocation requirements included, after which a Computational Fluid Dynamics (CFD) calculation was performed. In this research, use was made of a 95th percentile male to model the human anthropometry.

Other researches have focused more on the parameterisation of the front fuselage. Daumas[10] used a number of profiles defining the cross-section of the fuselage using their relative position, thickness and scale. This was lofted to make a fuselage, which was optimized together with the wing for sonic boom reduction. A study presented by Mestriner[11] focused more on the exterior design of a cockpit and the aerodynamic influence thereon. The cross-section of this design was dependent on the total length, width and height, but also the nose droop angle, nose radius, curve shape factors and the windshield base angle. Results have shown that the windshield angle mainly determines the location of the Mach supervelocity region, where the curvature of the defined curves influenced its magnitude. Finally, a research by Nicolisi[12] provided a fuselage drag prediction by means of the nose fineness ratio and the windshield angle.

It is noted that the aforementioned studies have been performed on tubular fuselages, while the Flying V is a flying wing with an internal cabin. Not many studies have been performed that show the design of a cockpit in detail, and it is especially rare to find one that treats the design for a flying wing. However, many Blended Wing Bodies (BWB) have a similar front fuselage shape, since their fuselage blends in with the wing. A small number of cockpit designs for this type of aircraft are shown in fig. 1.1.

(a) Airbus Maveric[1] (b) Boeing X-48[2] (c) Airbus ZEROe [3]

Figure 1.1: Examples of blended wing bodies and their cockpits

1.1. PROBLEM INDICATION

A cockpit design of the Flying V has previously been designed, as seen in fig. 1.2. However, this design can be improved in a number of ways, which are provided in this section.

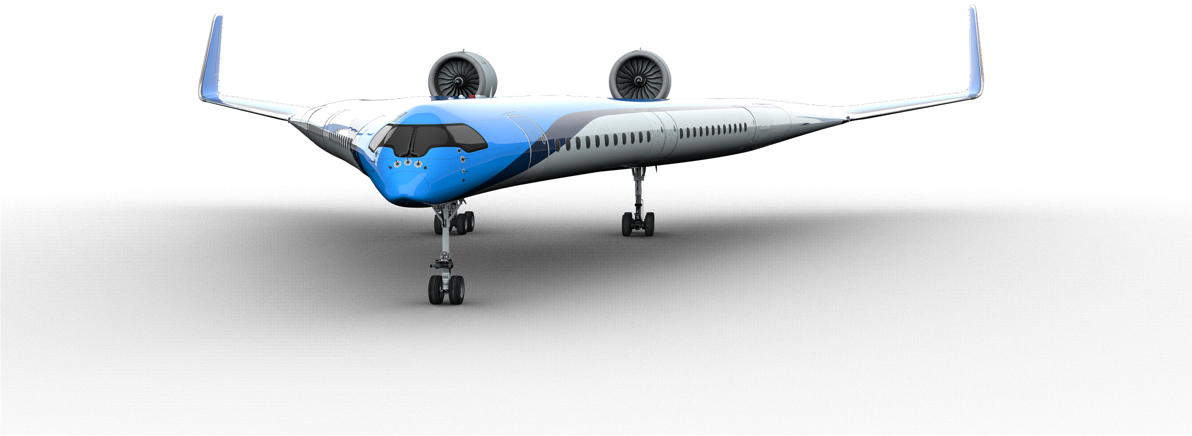

Figure 1.2: Flying V with an early cockpit design [4]

Firstly, the root of a wing featuring a high sweep angle will display an aerodynamic phenomenon: the root effect [13, 14]. The result of the root effect is that the isobars migrate towards the trailing edge, reducing the lift generated by the center of the wing and increasing pressure drag. Figure 1.3a shows that this problem is also seen in an optimized solution for the Flying V [3], as the Mach contours, and so the isobars, in the figure are swept aft. Furthermore, fig. 1.3b shows a steep drop in the lift generated at the root. The root effect can be reduced by changing the root airfoil by applying negative camber, twist and by moving the thickest point forward, as well as increasing the thickness to chord ratio.

---

[1] Airbus. https://www.airbus.com/newsroom/stories/Imagine-travelling-in-this-blended-wing-body-aircraft.html (Retrieved Januari 20, 2021)

[2] Tony Landis for NASA. http://www1.dfrc.nasa.gov/Gallery/Photo/X-48B/HTML/ED06-0198-62.html (Retrieved Januari 20, 2021)

[3] Airbus. https://www.airbus.com/innovation/zero-emission/hydrogen/zeroe.html (Retrieved Januari 20, 2021)

[4] Edwin Wallet for TU Delft. https://www.tudelft.nl/lr/flying-v/ (Retrieved September 1, 2020)

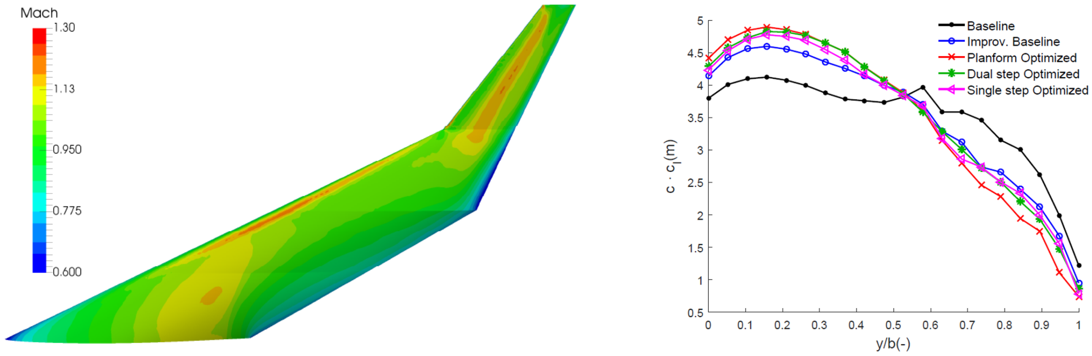

(a) Contours of equal Mach number of the Flying V (after[3])

(b) Lift distributions of optimized Flying V geometries (after [3])

Figure 1.3: Results from an earlier optimization performed by Faggiano (after [3])

Secondly, the root of the Flying V features a seam that is formed when the starboard wing geometry is mirrored in the xz-plane. This seam creates a transition between two wing halves that is not smooth. Especially near the trailing edge this may cause additional drag due to interference. Smoothing this surface reduces this effect.

Thirdly, the cockpit is the pilot's workstation. They need to have space allocated for them so that they can perform their work, which was not guaranteed in the design seen in fig. 1.2. Therefor, it needs to be known how large a pilot can be and what additional tolerances are required to allocate them. This is where pilot anthropometry provides a solution. Anthropometry is "the science of obtaining systematic measurements of the human body"[5], and is included in the design to understand how much room needs to be reserved for the pilots. Additionally, it is a certification requirement to be able to house pilots ranging in standing height from 1.58m to 1.91m [15], so it is required to not only reserve room for the smaller pilots, but also the larger end of the population. Additionally, a number of recommendations are given regarding planning room for the pilot in the books by Torenbeek[16] en Roskam[17]. These include, for example, the amount of headroom one must account for, and do not represent hard requirements but are instead best practices.

Fourth, due to the high sweep angle featured on the Flying V, a high angle of attack is required during landing[18]. This causes the aircraft to attain a high pitch angle, in turn requiring a large overnose angle in order to let the pilots have vision on the runway. The minimum required view-field from the captain's seat is set forth by the Federal Aviation Administration (FAA)[19]. This advisory circular describes the view that is required at all times, but also the special case of landing. However, the problem of a high overnose angle is not new. The Concorde also had a similar problem, which was solved by the use of a droop nose, as seen in fig. 1.4.

Figure 1.4: The Aérospatiale/BAC Concorde with its droop nose lowered to provide the pilots a higher overnose angle[6]

---

[5] `https://biologydictionary.net/anthropometry/` Retrieved: 10 January 2021

[6] Steve Fitzgerald. *Aerospatiale-BAC Concorde.* `http://www.airliners.net/photo/British-Aircraft-Corporation/Aerospatiale-BAC-Concorde/1804269/L/` (Retrieved January 20, 2021)

The fifth and final factor is that of system integration. The front fuselage is often home to the pilots, but also the nose landing gear and the weather radar. The nose landing gear has been designed by Bourget[18], together with the landing gear well required to house the wheel. Placing the well in the cockpit puts a geometrical constraint on the model which needs to be accounted for. Furthermore, the weather radar is modelled after the Honeywell flat plate antenna[20] and needs to be placed in front of the pilots, also putting its own geometrical constraints on the model.

1.2. PROBLEM STATEMENT

It is apparent that it is necessary to come with a model to integrate a cockpit design into the current parameterisation of the Flying V, together with a model for the center fairing behind the cabin. This should be done without compromising the aerodynamic performance of the aircraft. To come to such integration, the research objective is formulated *to create a parameterisation of the cockpit and aft center fairing for the Flying V that includes an integration of pilot anthropometry, satisfies visibility certification constraints, ensures positioning of nose landing gear and radar, while ensuring a high probability of good aerodynamic performance and being able to be used in an aerodynamic design optimisation.*

To achieve this objective, the following research question will be answered:

What is the cockpit and aft center fairing parameterisation that follows from pilot anthropometry, visibility certification constraints, system allocation requirements and ensures a high probability for good aerodynamic performance, while being able to be used in an aerodynamic design optimization?

The following sub-questions will be used to support the main research question:

1. How is the parameterisation of the cockpit and aft center fairing defined?
2. What constraints are imposed by pilot anthropometry, visibility certification constraints and the allocation of the radar and nose landing gear?
3. What is the influence of cockpit and aft center fairing integration on the aerodynamic performance of the Flying V?
4. What is the robustness of the cockpit and aft center fairing models?

1.3. SCOPE OF THE STUDY

The cockpit and aft center fairing are to be modelled and integrated into the Flying V. The resulting models are therefor meant to be applied to the Flying V, and not to any aircraft in general. These models are made with the purpose to be optimized, however, the optimization itself is not performed in this study.

The model used for the cockpit outer mold line will be used in an aerodynamic analysis, for which a number of objects are placed inside the cockpit, such as the pilots, nose landing gear and the weather radar. However, a detailed design of the instrument panel or controls is not deemed in the scope of this research. Similarly, the aft center fairing OML is used for aerodynamic analysis, however, moving parts such as high lift devices are not used. Furthermore, aerodynamic analysis is performed at cruise, where the free stream Mach number $M = 0.85$, at an altitude of $h = 13,000$m while flying at a lift coefficient of $C_L = 0.266$[3]. The atmospheric conditions are calculated using the International Standard Atmosphere (ISA).

Finally, pilot visibility is assessed at landing and even though the windshield needs to be able to resist a bird strike, no structural calculations are made in this research.

1.4. RESEARCH METHOD

The first research question will be answered by making a parameterisation for the outer mold line, consisting of the cockpit and the aft center fairing model (from hereon also named 'center fairing'). This will be done by making an application using Python in combination with Parapy[7]. The Parapy platform uses a suite of tools that allow 3D modelling, aerodynamic analysis and more. Following the parameterisation of the cockpit and center fairing is the research question dealing with the constraints imposed on the cockpit. The constraints put on the model by pilot anthropometry will be provided by using anthropometric data, after which is determined whether or not there is enough room for the pilot in the cockpit. Pilot visibility certification constraints

---

[6] Parapy. *Parapy: Knowledge Base Engineering Platform.* Retrieved December 02, 2020, from `https://www.parapy.nl/`

are to be assessed by using the required view-field to intersect the cockpit geometrical shape. This results in a windshield which can be expanded to form a more realistic version of the minimum. The nose landing gear will be positioned together with the radar after which it will be determined whether or not these geometries reside fully in the cockpit.

After the parameterisation and constraints are set, the model is ready to be analysed. This can be done in an optimization routine to determine the aerodynamic performance in cruise. To do this, the lift over drag ratio is often taken as the objective function. Because of this reason, the aerodynamic performance is analysed in cruise conditions. This is done using Stanford University Unstructured (SU2), an open source CFD tool that features the possibility of performing Euler calculations, which are relatively fast, making it useful for optimization. However, Euler calculations are inviscid and do not provide the viscous component of the drag coefficient. Therefor, semi-empirical methods are used to add an estimation for the viscous part.

Additionally, after the geometrical model is made, it can be tested for robustness. This will be done by sampling many points in a sample space using a Latin Hypercube Sampling method (LHS), spreading the samples evenly across the sample space. These points provide the parameters to be used in the model so that it can be tested to whether it provides a valid geometrical result or not.

1.5. RELEVANCE

This research is aimed at developing an engineering application to automatically design a cockpit and center fairing for the Flying V. The automation allows the application to be optimized, after which a new cockpit is designed for the Flying V which complies to the constraints put forth in this research. In this cockpit there will be enough room for the pilots, nose landing gear and the radar. Additionally, the pilots will have a large enough view-field during all stages of flight. Furthermore, the application developed in this research will contribute to the maturing of the Flying V outer mold line as a whole, since it assures the cockpit and center fairing provide a smooth and symmetric transition between the two half wings (port and starboard). Also, it adds more design freedom in defining the outer mold line.

Lastly, not much detailed information can be found on the design of a cockpit. Most studies either only focus on the outside geometry or the flight deck. This research will combine both to contribute to the knowledge base of the community.

1.6. THESIS OUTLINE

First, the model requirements are laid out in chapter 2. After this the geometrical model of the cockpit and center fairing is made in chapter 3, where also the constraints applicable to the cockpit can be found. Chapter 4 deals with the aerodynamic model and a deeper explanation of the root effect. Following the aerodynamics is a discussion of the results in chapter 5, containing a discussion of the robustness of the geometrical models and an application of the complete model. The latter is constituted of three cases, dealing with the aerodynamic results of the application but also the geometrical results. Finally, a conclusion is given and recommendations are provided in chapter 6.

2

MODEL REQUIREMENTS

Previous work has dealt with a multitude of aspects of the Flying V where it has shown great potential. It has shown to have a lift over drag ratio 10% higher than its reference aircraft, the A350-900. However, the need arose for a cockpit integration as the pilot and system integration were one of the next steps of the process of development. Usually, for a tube and wing aircraft, the basis geometry behind the cockpit consists of one or multiple ellipses. However, this is different for the Flying V because of the flying wing configuration. This causes the wing and cockpit aerodynamics to be closely linked. One result is that the root effect, which causes the wing to lose lift at the root of the wing, can be influenced by the design of the cockpit. To aid in increasing lift at the root of the flying wing, a trailing edge fairing is designed as well. This allows a more precise adjustment to the geometry at the root to help reducing the adverse effects of the root effect. These models will have to be integrated in previous work. An explanation of how this is done will be given in section 2.1. The requirements at the root profile are discussed in section 2.2. Finally, the requirements for optimization are treated in section 2.3.

2.1. COMPATIBILITY AND INTEGRATION IN PREVIOUS WORK

The model made for this research must be able to be integrated in the previous work by Hillen[8]. The integration is two-fold. Firstly, it must be integrated code-wise. This means that the original code made to generate the Flying V model will be expanded by means of Object Oriented Programming (OOP). Object oriented programming is a method of programming in which classes and objects are made that can be easily expanded upon. This method is used in combination with the Knowledge Based Engineering (KBE) software Parapy, which combines the OOP approach and a geometrical toolbox in a smart way, by only computing what is requested.

The second part of integrating the current model into the previous is of a geometrical nature. The cockpit or center fairing model must provide a connection to the original geometry that is as smooth as possible, while providing enough design freedom. Additionally, it must not compromise on the previous work performed. For example, because of advantages in the field of manufacturability, the definition of the wing profiles are perpendicular to the local sweep angle[8]. If the models developed in this research are to be made compatible with this definition, it is logical to align the profiles, or interface, connecting the two in the same way. This will help in making the transition smoother than it would when the definition of this interface is different.

2.2. ROOT AIRFOIL

Since the root effect is present on the Flying V due to its large sweep angle, the root airfoil can be adjusted to counter this effect. For this reason the model will make use of a cockpit and a center fairing that will be capable of increasing the lift generated at the root, bringing the lift distribution closer to an elliptical one. Defining the root airfoil in this way allows the cabin to remain largely unchanged at the fairing side, since a similar profile definition is used. Furthermore, the outer mold line of the Flying V presents a seam across the root airfoil. This causes additional concave curvature behind the thickest point of the airfoil, increasing super-velocities and drag due to interference. This seam can be removed at the location of the cockpit and center fairing, providing a smooth symmetric solution.

Furthermore, the cockpit is a functional shape. This means that it must house a number of systems, but also the pilots that control the aircraft. To be able to provide enough vision to the pilots during landing, it is often seen that an overnose angle is introduced below the start of the windshield. Including such a kink in the profile of the cockpit can result in additional drag, but is necessary to provide that the pilots can see enough of their surroundings.

2.3. OPTIMIZATION

Lastly, the intend of the presented model is to be optimized aerodynamically, while satisfying a number of geometrical constraints. This means that the amount of time it takes to evaluate a single geometry should be taken to a minimum. Decreasing the time required to evaluate a single iteration in the optimization results in a large time saving at the end of the total optimization effort. Besides the time required to run an evaluation, the curse of dimensionality comes into effect. First defined by Bellman, it describes the exponential increase in the search space when additional parameters are added[21]. This means that the more parameters are present in a model, the longer it takes to optimize, as there are more directions for the optimizer to look in. Therefor, the total amount of parameters should be limited as much as possible, while still being able to describe a complex geometry.

3

Geometrical Model

To develop the geometrical model of the Flying V cockpit and center fairing, use has been made of the Parapy software. This software allows the application to generate the geometrical model automatically using a number of inputs, and link this to other disciplines. One requirement is that the model is to be written using an Object Oriented Programming (OOP) approach, in which different parts of the model are represented by classes.

The geometrical model is structured according to fig. 3.1, of which a more detailed version can be seen in appendix A. As discussed before, the cockpit and center fairing models are to be developed for the Flying V parameterisation made by Hillen [8]. The components from that originate from this parameterisation are shown in yellow, where the classes developed for the current model are shown in blue. For a more in-dept discussion of the previous parameterisation, the reader is referred to the corresponding document[8]. The geometrical model consists of two main components, namely the wing and the fuselage. The wing in turn is made by the `IntegratedSemiWing` class. Instances of this class represent the entire starboard wing, which is composed of the base wing, cockpit and fairing geometry. These components are represented by the classes `SemiWing`, `CockpitOML` and `AftFairingOML` respectively. Furthermore, `FlightDeck` contains the flight deck geometry and constraints that apply to the cockpit. Lastly, `CockpitShape`, `FairingShape` and `FlightDeckShape` provide the inputs required for their respective classes.

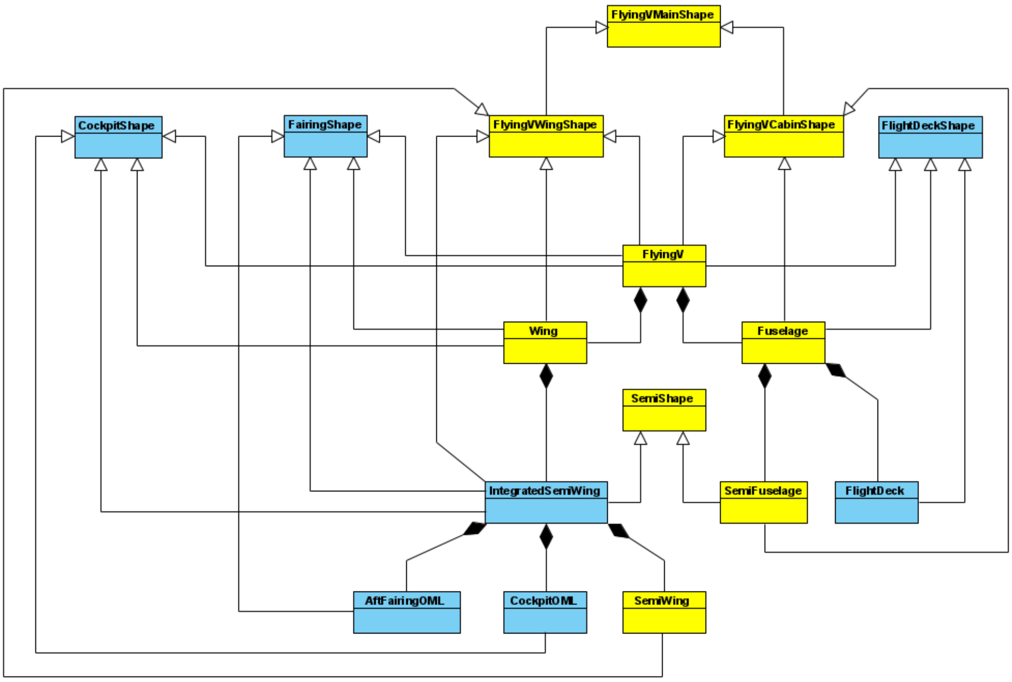

Figure 3.1: UML class diagram of the Flying V with integrated cockpit and fairing

The cockpit and center fairing outer mold lines provide the geometry as seen by the exterior flow. The method by which the outer mold line is defined will be discussed in section 3.1. Following the outer mold line definition are the cockpit constraints. These will include the modelling of the windshield, pilot, radar and nose landing gear and the constraints they impose on the model in mathematical form. This will be provided in section 3.2.

3.1. OUTER MOLD LINE

The outer mold line of the Flying V is defined by three parts: the base wing geometry, the cockpit and the center fairing. The cockpit and center fairing are made using a similar method of cutting and replacing portions of the base wing geometry, which is discussed in section 3.1.1. The cockpit shape that replaces the cut nose portion is modelled and parameterised in section 3.1.2. Finally, the center fairing parameterisation is shown in section 3.1.3.

3.1.1. SHAPE INSERTION METHOD

Since the current model needs to fit the geometry provided by the model developed by Hillen, it was chosen to cut out a designated area in which a replacing geometry can be placed. This was done by first defining the area to cut, as seen in fig. 3.2. For the cockpit this means that the cutting line is defined by two planes. One denotes the end of the cockpit along the aircraft x-axis, where the other is oriented perpendicular to the sweep angle. This was chosen to align the cutting plane in the same direction as the cross-sections of the base geometry, making it easier to provide continuity. The cutting planes are then used to define a `HalfSpaceSolid`, which is an infinite solid in the direction of the arrows shown below, and is only limited by the provided plane. This can then be used to cut out the section in which the new cockpit shape will be placed. One note that must be made is that the axis system is defined in the leading edge of the base wing, and this is the convention for the entirety of this document unless stated otherwise. The part of the wing from which the portions are removed is also called the base wing geometry for the remainder of this research.

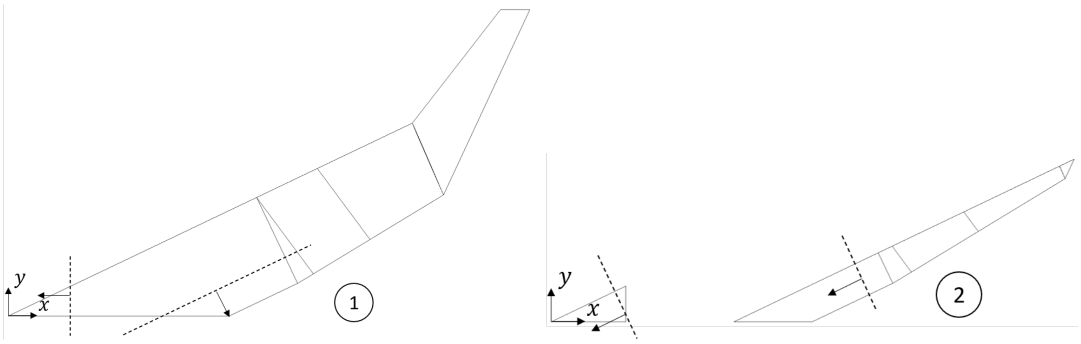

(a) Step 1: cut the wing at a position on the x-axis

(b) step 2: cut the geometry of interest along the span

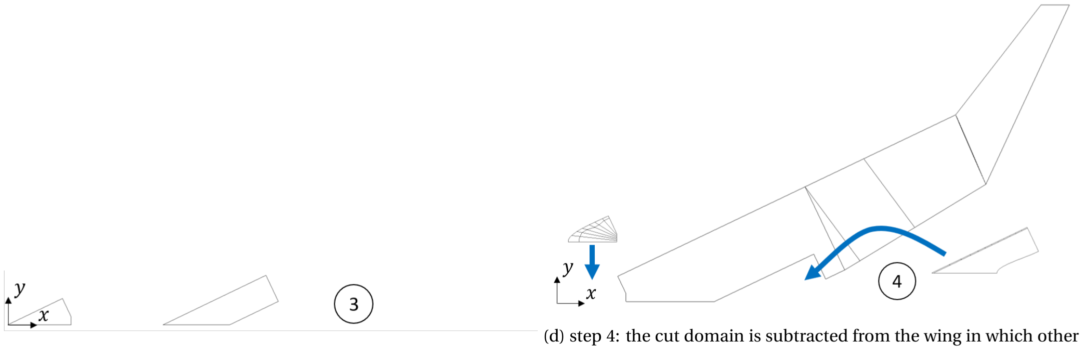

(c) step 3: the geometry of interest is cut from the wing

(d) step 4: the cut domain is subtracted from the wing in which other geometries are placed

Figure 3.2: Shape insertion method. First the geometry of interest (cockpit or center fairing) is extracted from the wing from which information can be gathered (step 1-3). Then these shapes can be subtracted to be able to insert new geometries (step 4). Dotted lines indicate a plane, arrows indicate direction in which a HalfSpaceSolid is present

For the fairing the same principle applies, however, the plane definition is slightly different. The first plane is placed at a defined fraction along the chord in the span direction, and denotes the front of the fairing. The second plane defines the end of the fairing and is placed at an angle relative to the xz-plane.

3.1.2. COCKPIT PARAMETERISATION

The parameterisation of the cockpit model consists of four parts. First, the class `CutOutCockpit` cuts the cockpit design space from the base geometry, as shown in section 3.1.1. After this, a leading edge rail is created using `Rail`, fully defining the planform of the cockpit. Along the rail, cross-sectional curves are placed by means of `CockpitCrossSection`, after which the class `CockpitInterpolation` creates an interpolation between these curves. Lastly, a shell is made by using the aforementioned curves. The result of this process can be seen in fig. 3.4. Furtermore, the class `FitCockpitCurve` represents the final cross-section and is used to make the final loft. This cross-section can not be changed since it is shaped by cutting the wing.

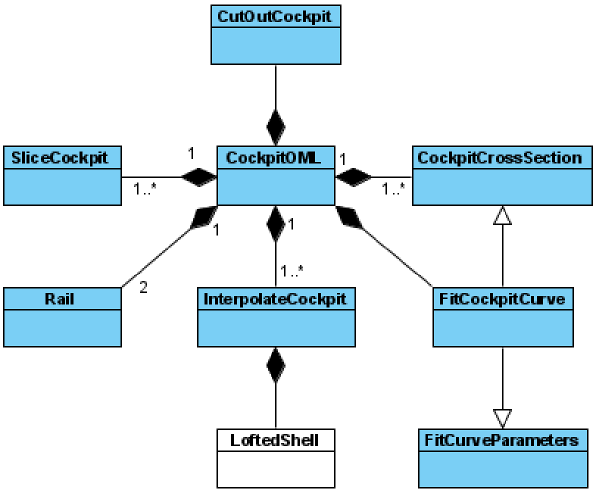

Figure 3.3: UML class diagram of the cockpit geometric model

This method was chosen because it results in continuous curves in the plane the cross-sections lie. It also makes sure that the last cross-section is defined in the same plane as used for the definition of the wing profiles. This helps in fitting the cockpit geometry in the base wing geometry. An alternative could have been to cut the wing using a plane having its normal vector in x-direction, however, then the transition between the cockpit and wing would have been less smooth.

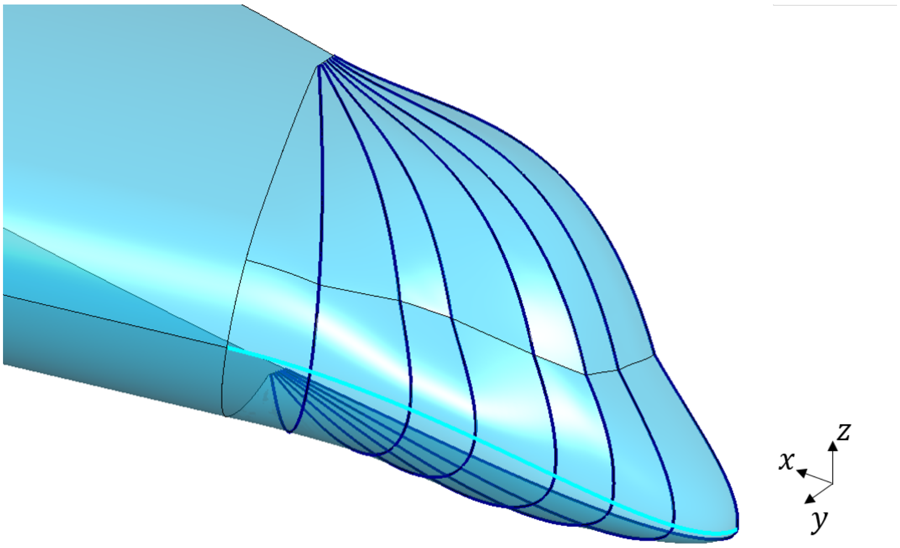

Figure 3.4: Flying V cockpit buildup with the cross-sectional components indicated with thick blue lines and the rail indicated by the thick cyan line

PLANFORM

Before a shell can be made that defines the cockpit exterior shape, a cut is made using the method discussed in fig. 3.2. In fig. 3.5, it can be seen that the cut is defined by 2 variables. First is the cockpit end position along the x-axis, x_{cockpit}. This defines the first cutting plane. The second cutting plane is offset in y-direction by a small distance δ_{cockpit}. The offset preferred over a situation where the cross-sections are positioned in one point, because the latter would later result in an inability to create a mesh due to multiple lines coming in a singular point. Therefor, an offset is included to create a situation where a mesh can be generated and aerodynamic analysis is possible. The aft rail upon which the cockpit cross-sections are positioned is defined by this offset line.

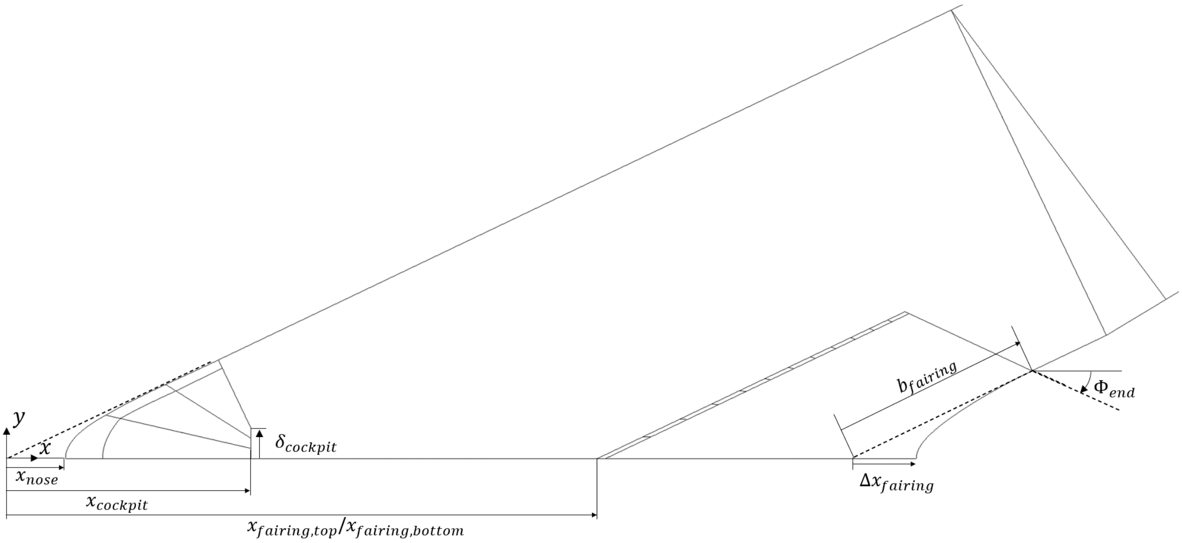

Figure 3.5: Top-view of the parameterisation for the cockpit and center fairing outer mold lines

After the cockpit design space has been cut from the base wing geometry, a leading edge rail can be inserted. This rail is described by two points, namely the start and end point. The start point is given by the nose point, which is located at x_{nose} from the original nose point along the x-axis. The end point is located at the connection to the cut geometry and assures a continuity in the planform. Furthermore, the rail must be tangent to the cut geometry at the end point and must have the tangent in y-direction at $y = 0$. The rail definition is defined in two planes: the xy-plane and yz-plane. The former is defined by the following equation, upon which the point and tangent continuity conditions are applied:

$$x_{\text{start}} = -(ay_{\text{start}}^4 + by_{\text{start}}^3 + cy_{\text{start}}^2 + dy_{\text{start}} + e) \tag{3.1}$$

$$x_{\text{end}} = -(ay_{\text{end}}^4 + by_{\text{end}}^3 + cy_{\text{end}}^2 + dy_{\text{end}} + e) \tag{3.2}$$

$$\left(\frac{dx}{dz}\right)_{\text{start}} = -(4ay_{\text{start}}^3 + 3by_{\text{start}}^2 + 2cy_{\text{start}} + d) \tag{3.3}$$

$$\left(\frac{dx}{dz}\right)_{\text{end}} = -(4ay_{\text{end}}^3 + 3by_{\text{end}}^2 + 2cy_{\text{end}} + d) \tag{3.4}$$

Here, x and y are the coordinates of the rail and the variables a to e are polynomial parameters. However, there is one free variable since there are four equations and five unknowns. It is chosen to have the parameter a free to be changed to allow freedom in the curvature of the rail, where the other four are set using point and tangent continuity by using the above equations. For the leading edge rail of the cockpit, the free variable is written as $a_{\text{rail,cockpit}}$. The rail is defined in the yz-plane by use of a cosine function. This was chosen because it assures a smooth symmetric curve definition at the center, and allows a tangent condition at the end point. Furthermore, the amplitude is easily changed to define the effective downward droop of the nose. The equation is given by:

$$z = -0.5R\left(\cos\left(\pi\frac{y - y_{start}}{y_{end} - y_{start}}\right) + 1\right) \tag{3.5}$$

Where, y and z are the coordinates of the rail, and y_{start} and y_{end} are the y-coordinates of the start and end points respectively. Furthermore, R is the amplitude of the cosine function and changes the effective downward droop of the nose of the aircraft and is called R_{cockpit} for the cockpit rail. An example of the shape of these curves is given in fig. 3.6:

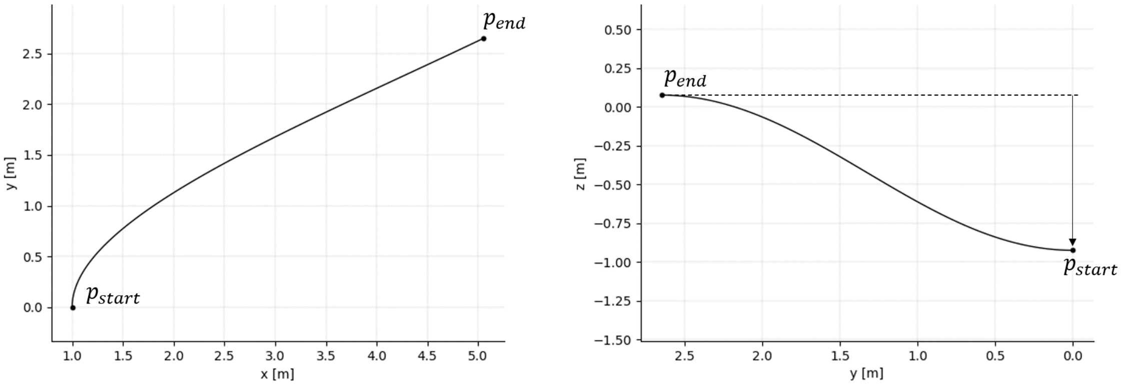

(a) Rail example in the xy-plane, The rail attaches at the end point to the wing where the start point is on the x-axis

(b) Rail example in the yz-plane, where R is the downward displacement of the nose relative to the attachment point

Figure 3.6: Rail curve definition as seen in the xy-plane and the yz-plane.

In fig. 3.6, it can be seen that the rail is largely defined by the position of the start and end point, as well as the tangent at both points, defined by ϕ_{start} and ϕ_{end} respectively. From a front view, as seen in fig. 3.6b, the R parameter describes the vertical displacement of the start point relative to the end point. For the cockpit this means that it describes the vertical displacement between the leading edge at the cutting plane and the nose of the cockpit.

The parameters used for defining the planform are shown in table 3.1:

Table 3.1: Parameters used for the cockpit planform

parameters	symbol	unit
nose x-location	x_{nose}	[m]
cockpit end location	x_{cockpit}	[m]
aft tolerance	δ_{cockpit}	[m]
rail z-displacement	R_{cockpit}	[-]
rail free parameter	$a_{\text{rail,cockpit}}$	[-]

After the rail is fully defined, the cockpit cross-sectional curves can be defined so that these can be placed on the rail. The cockpit cross-sectional curve definition is shown in the following section.

COCKPIT CROSS-SECTION

After the rail has been defined, the cockpit cross-sections can be made. The cross-section for the cockpit is defined in the xz-plane by means of three curves, called curve elements. Each of these curves is defined by a start and end point, as shown in fig. 3.7. This setup divides the top and bottom of the cockpit, while keeping a continuous shape at the leading edge. The top is further divided in two parts. This creates a typical shape seen in other aircraft and provides the possibility of adding an overnose angle, ϕ_{window}, for the pilot to see the runway at landing.

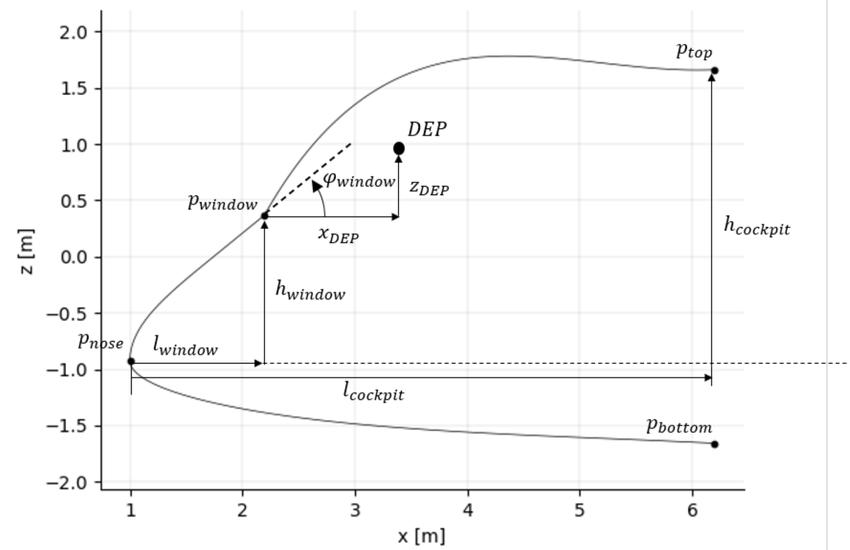

Figure 3.7: Cockpit cross-section curve definition together with the definition of the design eye point (DEP)

Each curve element is defined by four cone variables, and is constrained at their own start and end points, but also by using the tangent at the end point. For simplicity, the start and end points are named p_{start} and p_{end} respectively, and are different for each curve element. The equation is shifted horizontally so that the nose of the cross-section is at x=0. The resulting system of equations is as follows:

$$z_{\text{start}} = a\sqrt{x_{\text{start}} - x_{\text{nose}}} + d(x_{\text{start}} - x_{\text{nose}})^2 + e(x_{\text{start}} - x_{\text{nose}}) + b \tag{3.6}$$

$$z_{\text{end}} = a\sqrt{x_{\text{end}} - x_{\text{nose}}} + d(x_{\text{end}} - x_{\text{nose}})^2 + e(x_{\text{end}} - x_{\text{nose}}) + b \tag{3.7}$$

$$\left(\frac{dz}{dx}\right)_{\text{end}} = \frac{a}{2\sqrt{x_{\text{end}} - x_{\text{nose}}}} + 2d(x_{\text{end}} - x_{\text{nose}}) + e \tag{3.8}$$

This equation is constrained at the start and end points, together with the tangent at the end point. This means that there is still one free and controllable variable. It was chosen to use $a \cdot e = p$ as a free variable to influence the general curvature of the curve. The $\sqrt{x}$ term allows the front top curve and the bottom curve to have the same tangent at $x = 0$.

It follows that for the cross-section definition, there are 6 free design variable. The first three are the free variables, p, defined per curve. Furthermore, the window point is defined by the ratio's $\overline{l}_{\text{window}} = \frac{l_{\text{window}}}{l_{\text{cockpit}}}$ and $\overline{h}_{\text{window}} = \frac{h_{\text{window}}}{h_{\text{cockpit}}}$. The final design variable is given by the overnose angle ϕ_{window} and influences the front top curve. This is not provided for the other two curves as these are defined to be tangent to the original geometry. Furthermore, there is the definition of the Design Eye Point (DEP), which positioned by the x- and z-positions (x_{DEP} and z_{DEP} respectively). This point will be further explained in section 3.2.1.

The parameters used to create a single cross-section are shown in table 3.2. These are used for every cross-section, so when one is added, the total parameter count increases by 7. The positioning of the cross-section as described in the following paragraph, is also included.

Table 3.2: Parameters used for the cross-section definition.

parameters	symbol	unit
horizontal window position	$\overline{l}_{\text{window}}$	[-]
vertical window position	$\overline{h}_{\text{window}}$	[-]
view angle	ϕ_{window}	[°]
free variable aft top curve	$p_{\text{top,aft}}$	[-]
free variable front top curve	$p_{\text{top,front}}$	[-]
free variable bottom curve	p_{bottom}	[-]
cross-section position	f_{cockpit}	[°]

CROSS-SECTION POSITIONING

After the cross-section is defined it can be placed to form the start of the cockpit wireframe. The cross-sections are placed onto the rear rail at equispaced lengths, as shown in fig. 3.8. At this point, the curves are placed at an angle defined by a fraction of the sweep angle using $\phi^n_{\text{cockpit}} = f^n_{\text{cockpit}}\Lambda$. Here, the parameter $f^n_{cockpit}$ is set for every cross-section n and represents the fraction of the sweep angle Λ, since this is also the angle of the starboard cutting plane.

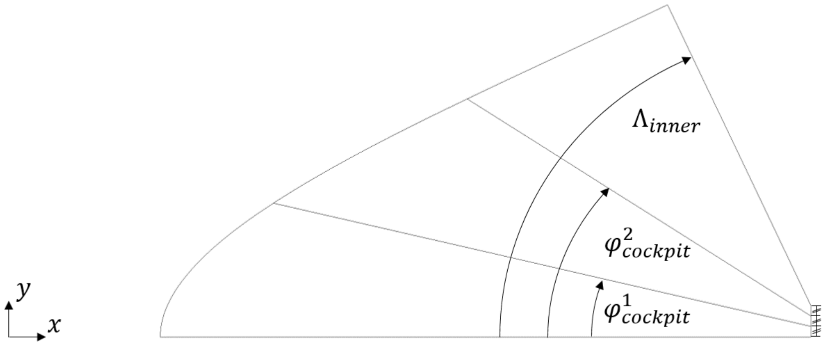

Figure 3.8: The cockpit cross-sections are placed equispaced on the rear rail at an angle ϕ_{cockpit} defined by the parameter $f_{cockpit}$ and the sweep angle Λ

CURVE INTERPOLATION

Before a loft can be made, a custom curve interpolation is made. This is done to make sure the CAD software can follow the leading edge rail properly and does not deviate much from this. The interpolation is performed between each pair of cross-sections, and for each of the three curve elements defined above. First, the cross-sections were normalised in x-direction. This allows for an easier interpolation between the different them. After the normalisation, a number of points are sampled on each curve element of the cross-sections using a cosine sampling, accumulating more points at the ends and less in the center. After the points are sampled for each curve element of the two cross-sections, the points can be interpolated in x- and z-direction. Then, the three-curve-setup is used on the resulting point-sets and these curves are placed between the basis cross-sections. The result can be seen in fig. 3.9a.

A total of three interpolated curve-sets are shown per cross-section combination which provides are good approximation of the leading edge rail when making a shell. A final note should be made that the point interpolation could have been replaced by an interpolation of the cross-sectional parameters. However, it was determined experimentally that this method would result in unexpected behaviour because of the scaling of the cross-sections, in combination with the use of the windshield point.

SHELL CONSTRUCTION

The creation of the shell is the final step towards making the cockpit outer mold line. First, a loft is made through the interpolated curves and their basis cross-section pairs by means of the `LoftedShell` class, as shown in fig. 3.9a. The loft is not made through the entire curve at once, but three times, once through every cross-section element. This results in a distinct window line at which the windshield can be placed. Running a loft through all curves at once would result in an inaccurate and erratic loft at the discontinuity of the windshield point.

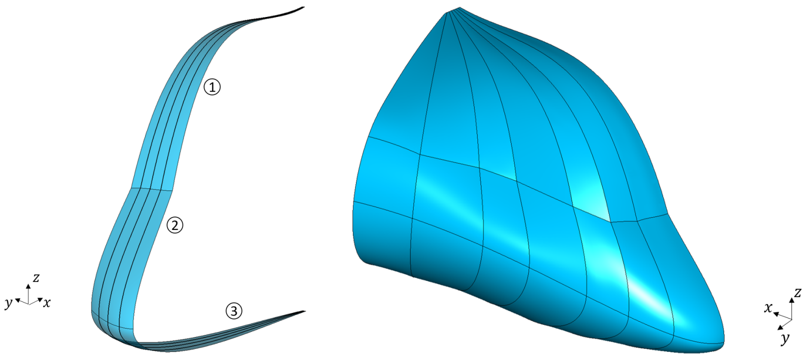

(a) A panel composed of three lofts through the interpolated curves and their basis cross-sections

(b) Multiple loft panels combined to form the cockpit shell

Figure 3.9: Lofting of the cockpit shell. It is composed of multiple panels that are each constituted of three separate lofts

This method is repeated for each pair of cross-sections. This method was preferred over a single loft over all pairs at once, because the latter would result in a less robust model and a mismatch in the common edges of the three shells. An advantage of such method would be that the resulting shell is smoother. However, the penalty to robustness was deemed too large to afford this luxury.

Finally, the center panel is created using not only the relevant starboard cross-section pair and their interpolations, but also their mirrored counterparts. This is required to ensure a smooth symmetric center panel shell. Furthermore, to increase the robustness of the model, it was found that the center panels break a possible solution for the shell at more exotic parameter inputs, commonly seen in optimizations. For this reason a `try_fix` option is provided that, when the original method fails, uses only the cross-section pair and the mirrored counterpart, without the interpolations in between. This increases the error between the leading edge rail and the cockpit shell, however, it is possible to analyse the geometry and find out if this is a direction the optimizer should look in.

The final result can be seen in fig. 3.9b, where the lofted shell panels are combined in one shell using the `SewnShell` class.

3.1.3. FAIRING PARAMETERISATION

The parameterisation of the fairing is performed in a similar manner as for the cockpit, for which the class diagram is shown in fig. 3.10. First, the fairing area is cut using the method described in section 3.1.1, by means of the class `CutOutFairing`. Then, the trailing edge rail is defined by `Rail`, setting the planform of the center fairing. After this the cross-sections can be made with `FairingCrossSection` which is placed along the trailing edge rail to form the skeleton of the fairing shell using `SpreadFairing`, as seen in fig. 3.11. To aid in the accuracy between the defined rail and the resulting shell, `InterpolateFairing` is used to interpolate the defined cross-sections. Finally, using the interpolated cross-sections, the shell can be constructed that forms the outer mold line of the center fairing.

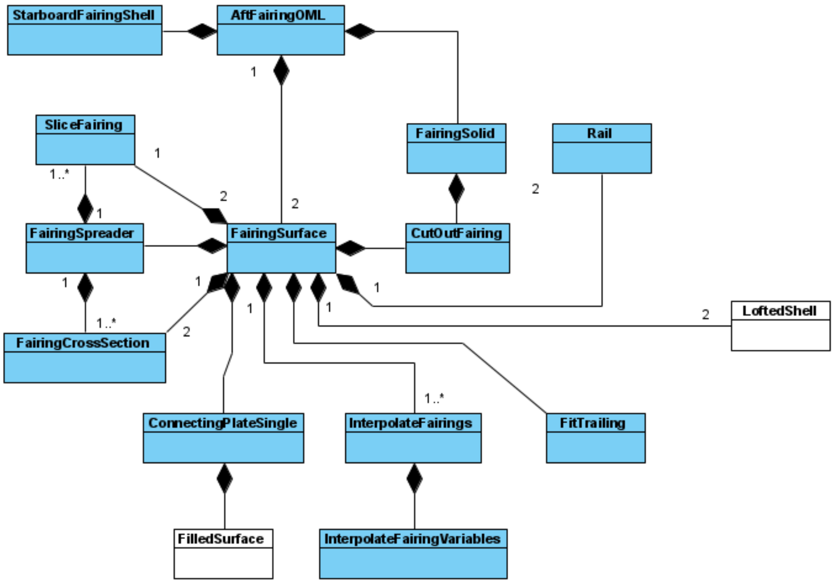

Figure 3.10: UML class diagram of the center fairing geometrical model

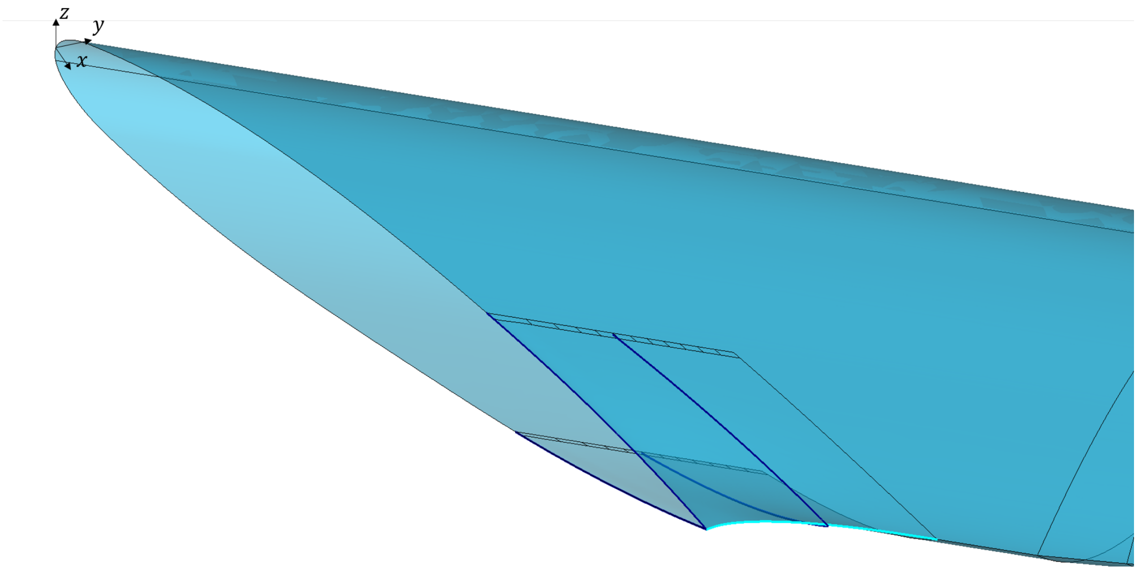

Figure 3.11: Fairing geometry definition with the cross-sectional components indicated with thick blue lines and the rail indicated by the thick cyan line

PLANFORM

The fairing consists of two surfaces, a top and a bottom surface. Each can start at a different fraction along the chord, which is defined by $x_{\text{fairing,top}}$ and $x_{\text{fairing,bottom}}$, as shown in fig. 3.5. The trailing edge of the root chord is defined by δ_{fairing}, being the change in x-coordinate between the original trailing edge and that of the fairing. The length is defined by the spanwise distance b_{fairing}, defining the cutting plane at the starboard end of the center fairing. Here, the plane is oriented at an angle Φ_{end}, which represents the angle relative to the flight direction.

After the cut is made, the trailing edge rail can be defined. The rail uses the same equations shown in section 3.1.2, but here the start point it represented by the trailing edge point in the symmetry plane. The end point of the fairing corresponds to the trailing edge at the starboard cutting plane. Also for this rail, the free parameter $a_{rail,fairing}$ describes the curvature as seen in the xy-plane. Additionally, $R_{fairing}$ describes the downward displacement of the trailing edge at the center. An overview of the parameters used for the definition of the center fairing planform can be seen in table 3.3.

Table 3.3: Parameters used to define the planform of the center fairing

parameters	symbol	unit
start location top	$x_{\text{fairing,top}}$	[m]
start location bottom	$x_{\text{fairing,bottom}}$	[m]
aft displacement	$\Delta x_{\text{fairing}}$	[m]
spanwise start location	b_{fairing}	[m]
end angle	Φ_{end}	[°]
rail z-displacement	R_{fairing}	[m]
rail free parameter	$a_{\text{rail,fairing}}$	[-]

FAIRING CROSS-SECTION

As the fairing is divided in two surfaces, the cross section of the fairing, defined in the xz-plane, is divided in two curves: a top and bottom curve. The two curves are fourth order polynomial functions as defined below and shown in fig. 3.12. The curves are attached to the original geometry and tangency continuity is imposed as well as curvature continuity. After defining the trailing edge point of the cross section, one parameter still remains. The free parameter can be changed and it represents the a parameter in the equation. This results in the following set of equations:

$$\begin{aligned}
z_{\text{start}} &= a(x_{\text{start}}-x_{\text{LE}})^4 + b(x_{\text{start}}-x_{\text{LE}})^3 + c(x_{\text{start}}-x_{\text{LE}})^2 + d(x_{\text{start}}-x_{\text{LE}}) + e \\
z_{\text{end}} &= a(x_{\text{end}}-x_{\text{LE}})^4 + b(x_{\text{end}}-x_{\text{LE}})^3 + c(x_{\text{end}}-x_{\text{LE}})^2 + d(x_{\text{end}}-x_{\text{LE}}) + e \\
\left(\frac{dz}{dx}\right)_{\text{start}} &= 4a(x_{\text{start}}-x_{\text{LE}})^3 + 3b(x_{\text{start}}-x_{\text{LE}})^2 + 2c(x_{\text{start}}-x_{\text{LE}}) + d \\
\left(\frac{d^2z}{dx^2}\right)_{\text{start}} &= 12a(x_{\text{start}}-x_{\text{LE}})^2 + 6b(x_{\text{start}}-x_{\text{LE}}) + 2c
\end{aligned}$$

Where x_{start} and z_{start} represent the coordinates of the forward end point of the curve, which is connected to the main geometry. Furthermore, x_{end} and z_{end} are the coordinates of the trailing edge of the curve. Additionally, a to e are the polynomial coefficients, of which a is free. It can be seen that the curve is shifted by x_{LE}, the x-coordinate of the leading edge of the local airfoil. This is done to maintain the same parameterisation for different positions of the cross-section. For example, the most starboard cross-section has a larger leading edge x-coordinate than the most inward section, resulting in a different fairing shape for the same parameters if such a shift was not included.

An overview of the parameters used in the definition of the center fairing cross-section is given in table 3.4. These parameters are required for each cross-section. So, if a cross-section is added, the total parameter count will increase by 3. However, since f_{fairing} is optional, the parameter count can also be increased by 2.

Table 3.4: Parameters used in the definition of the center fairing cross-section

parameters	symbol	unit
free variable top curve	$a_{\text{fairing,top}}$	[-]
free variable bottom curve	$a_{\text{fairing,bottom}}$	[-]
cross-section location	f_{fairing}	[-]

CROSS-SECTION POSITIONING

The positioning of the cross-sections is done in a similar way as is done for the cockpit. First, the position on the trailing edge is chosen using a fraction $f^n_{\text{fairing}} = \frac{l^n_{\text{f,section}}}{l_{\text{rail}}}$ of the total rail length, for each cross-section n, as can be seen in fig. 3.13. However, it can also be chosen to have the cross-sections spread evenly over the rail length, in which case no input is required. After the position is known, the cross-section can be oriented using the same fraction applied to the angular position: $f^n_{\text{fairing}} = \frac{\phi^n_{\text{fairing}}}{\Phi_{\text{end}}}$. This approach was not included for the cockpit since it was assumed that δ_{cockpit} remains as small as possible, therefor a consistent and even spread was preferred.

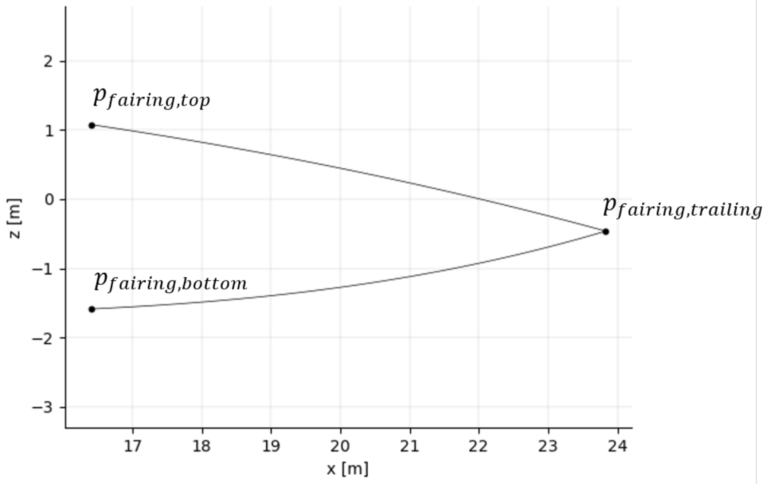

Figure 3.12: Cross-section used for the generation of the center fairing. The points $p_{\mathrm{f,top}}$ and $p_{\mathrm{f,bottom}}$ are connected to the main wing geometry where the curves are required to follow the local tangent

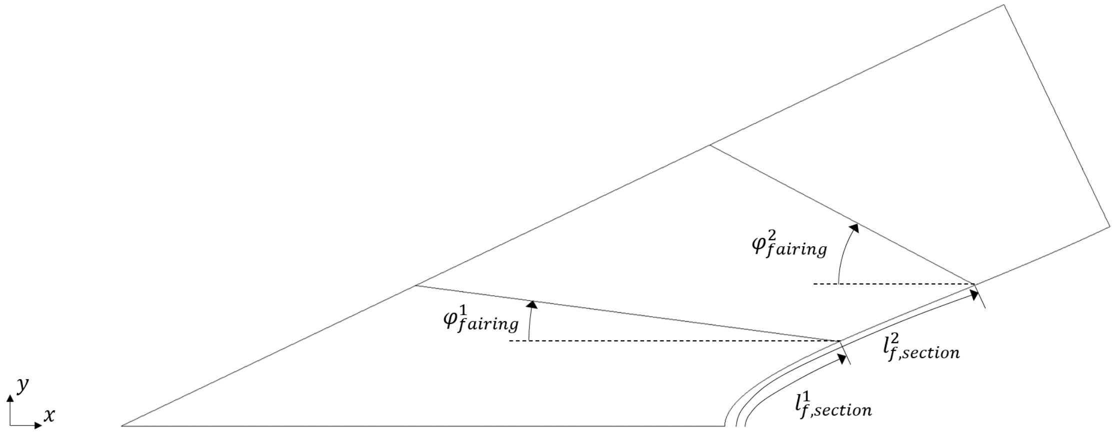

Figure 3.13: Positioning of center fairing cross-sections. Where $l_{\mathrm{f,section}}$ is the length along the trailing edge rail of the fairing, and ϕ_{fairing} is the angle at which the cross-sections are oriented.

CURVE INTERPOLATION

After the cross-sections are placed, an interpolation can be performed between each pair of curves. This is done to increase the accuracy of the loft with respect to the defined rail. The curves are interpolated by means of linear interpolations between the free variables $a_{\mathrm{fairing,top}}$ and $a_{\mathrm{fairing,bottom}}$, of the cross-section curves. The result is shown in fig. 3.14, where the interpolated curves are shown in red and the defined cross-sections are displayed in dark blue.

SHELL CONSTRUCTION

The cross-sections, together with the interpolated curves, form the skeleton of the shell loft. Additionally, to create a symmetric shell, all the cross-sections and interpolated curves are also mirrored. This causes a smooth and symmetric shell to form. However, when a shell is made by use of the `LoftedShell` class, a deviation occurs at the front of the fairing shell, as seen in fig. 3.15a. The issue is that the method only uses the supplied profiles, but does not recognise that the front rail is discontinuous. This causes a gap between the shell and the line that connects the fairing and base wing geometry. Because of this behaviour, it is difficult in most cases to combine both geometries into one and perform an analysis.

To remedy this problem, a transition surface is made, as seen in fig. 3.15b in green. For this, the fairing is cut along the sweep direction at a small distance aft of the connecting line, and a transition surface is defined.

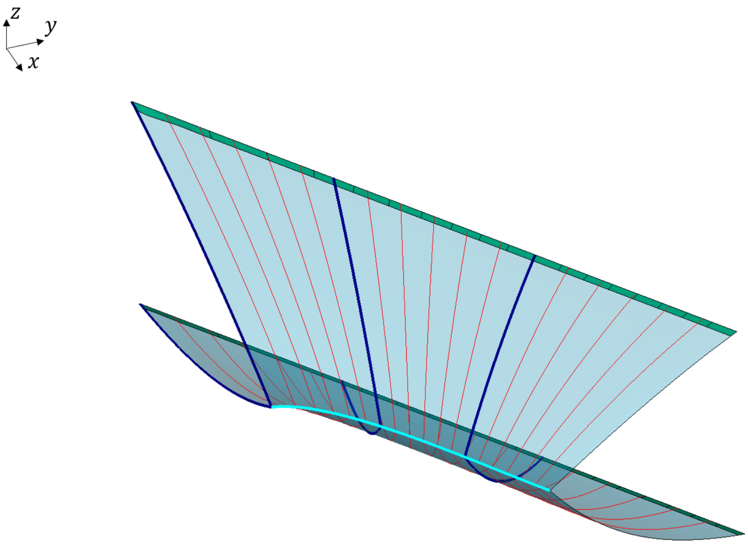

Figure 3.14: Interpolated fairing cross-sections (red) made from the basis cross-section curves (dark blue) placed along the trailing edge rail (cyan). Additionally, the transition surface can be seen (dark green)

This surface is made up of multiple `Face` instances which provide a tangent and curvature continuous solution between the original geometry and that of the inserted fairing. The resulting fairing shell can be seen in fig. 3.11, together with the defined cross-sections in dark blue.

3.1.4. ROBUSTNESS

After the geometric models are made, their robustness can be evaluated. The robustness of the models will be assessed by taking a large number of design points, and computing the volume of the total wing geometry. This forces the program to generate the geometry assures that the cockpit or center fairing can be made using the supplied parameters, and that it can be combined with the base wing geometry. The robustness, r, is then given by the fraction of feasible geometries over the total amount of samples taken:

$$r = \frac{N_{feasible}}{N_{total}} \tag{3.9}$$

First, the sample space is defined. After this, the sample space will be sampled using the Latin Hypercube Sampling method, a popular method in Monte Carlo-type simulations [22].

SAMPLE SPACE

Since the models are intended to be optimized, it needs to be known what the robustness is for each model. For this, the design space of such optimization needs to be sampled. The design space is defined in the negative null form of an optimization:

$$\begin{aligned} &\text{minimize } f(\mathbf{x}) \\ &\text{subject to } \mathbf{h}(\mathbf{x}) = \mathbf{0}, \\ &\mathbf{g}(\mathbf{x}) \leq \mathbf{0}, \\ &\text{and } \mathbf{x} \in X \subset R^n \end{aligned} \tag{3.10}$$

Here, $f(\mathbf{x})$ is the objective function to be optimized, $\mathbf{h}(\mathbf{x})$ and $\mathbf{g}(\mathbf{x})$ are the equality and inequality constraints respectively, x is the design vector containing the n design variables and X is the design space. Here X needs to be sampled if the robustness is to be calculated, which is treated in the following paragraph. For this the constraints imposed by the cockpit, as discussed in section 3.2, are not taken into account, since this would not make a difference in the robustness figures and only add to the parameter count, expanding the sample space.

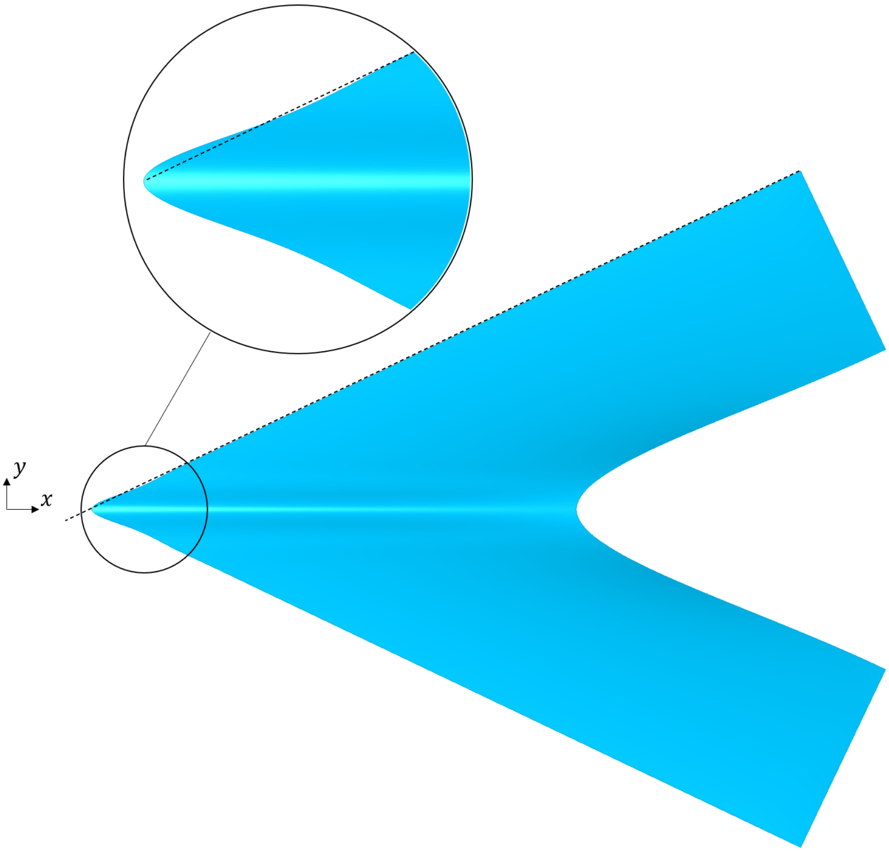

(a) A gap is created between the fairing shell and the remaining geometry when a symmetric loft is made, preventing a closed shell when attempting to combine the two (dotted line shows the attachment line of the base wing geometry)

(b) A transition surface (green) is made that connects the fairing and wing geometry

Figure 3.15: A transition surface is required between the fairing shell and the remaining wing geometry in order to prevent a gap from occurring

SAMPLING METHOD

The design space X is defined by its bounds, which are defined for the n design variables. The values for these bounds are given in appendix B. The design space can then be sampled within the provided bounds. In order to do this, a Latin Hypercube Sampling (LHS) method is used by means of the pyDOE package for Python[1]. This method divides the sample space in a number of intervals across each dimension/parameter, as seen in fig. 3.16. Each row or column (interval) can only have one data point. This assures that the samples are spread out as opposed to a fully random sampling, where it can occur that the data points are clustered.

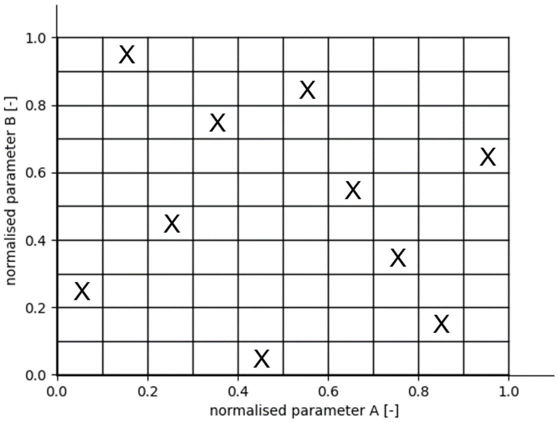

Figure 3.16: Latin hypercube samping (LHS). All points are spread over the rows and columns so that no two points are in the same interval

After the sample space is sampled, the robustness can be calculated. The criteria for determining whether a sample point results in a success or a fail is that it must provide a valid geometry. For this the volume of the geometry is calculated that combines the base wing geometry and that of the cockpit or fairing. This assures that there are no self-intersecting airfoils or geometries that the software can not generate.

3.2. COCKPIT CONSTRAINTS

In order to come up with a successful cockpit design, a number of requirements need to be satisfied. Some of these are imposed by the presence of the pilots. An example is the minimum unobstructed view field from the captain's seat, but also the physical size of the pilot plays a role in the definition of the requirements. These requirements put constraints on the outer mold line of the cockpit geometry, and can be formulated in a mathematical form. The constraints and requirements that apply are treated in this section, and are structured as in the code as seen in fig. 3.17.

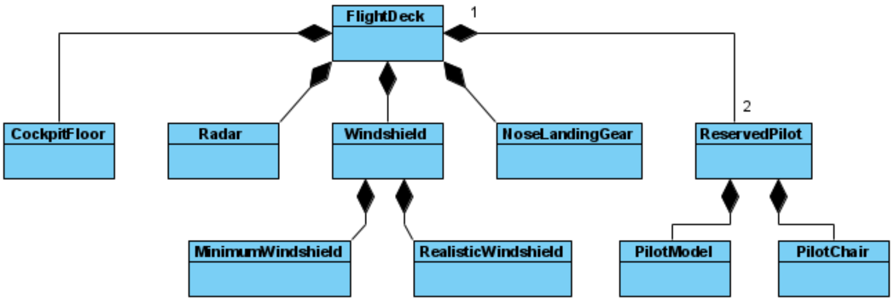

Figure 3.17: UML class diagram of the flightdeck constraints

First, the pilot's compartment view is discussed in section 3.2.1. Following the pilot compartment view is a review of pilot anthropometrics, which will be discussed in section 3.2.2. The nose landing gear needs to be allocated in the cockpit as well. The nose landing gear model is provided in section 3.2.3, as well as the

---

[1] pyDOE. `https://pypi.org/project/pyDOE/` (Retrieved 19/01/2021)

constraints it puts on the cockpit design. Finally,section 3.2.4 treats the modelling and constraints imposed by the weather radar on the cockpit design.

3.2.1. PILOT COMPARTMENT VIEW

The minimum available view outside at the pilot seat is prescribed by aviation authorities, and is required to provide a good enough impression of the environment to the pilots. The available view field is described by a set of angles relative to the x-axis in the aircraft body reference frame and is composed of two parts. First is the pilot compartment view that needs to be present at all times. This requirement is set forth by Advisory Circular 25.773-1 section 4C [19], and it shows a range of angles of clear view, measured from the design eye point (DEP). This field of view is shown in fig. 3.18 and is shown in the backward directed hatches. The view-field is mirrored around the vertical axis for the first officer and it must be noted that this area can be expanded, but never shrunk. Additionally, it is not allowed to have any obstructions within the horizontal range between 20 degrees port and 20 degrees starboard. Outside this range the number of obstructions needs to be limited to a minimum.

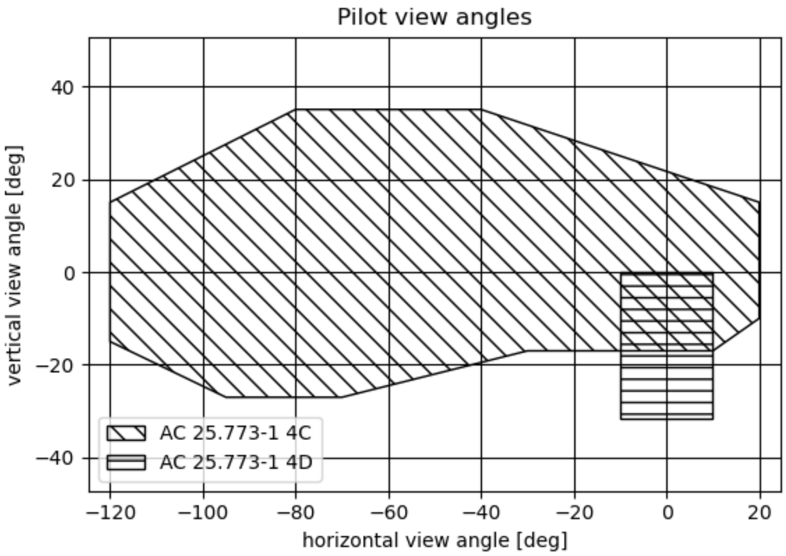

Figure 3.18: Minimum view angles from the design eye point. Backward slashed hatches represent the view angles from AC 25.773-1 section 4C, horizontal hatches represent the view angles required at landing as described in section 4D of the circular

Second is the view-field required at landing, which is described by section 4D of the circular[19]. The field of view required at landing is defined by the downward angle measured from the design eye point, within a horizontal range defined by landing with a crosswind of 10 knots. The required downward view angle, or overnose angle, is calculated by allowing the pilot to see for a distance on the runway that will be covered within three seconds during landing, as shown in fig. 3.19. This is assuming the weather conditions allow a 366 meter (1200 feet) runway visual range (RVR), while the lowest point of the aircraft is at a height of 100 feet (30.5 meter) above the runway. Furthermore, the aircraft is on a 2.5° glideslope and loaded at the most critical weight and center of gravity position.

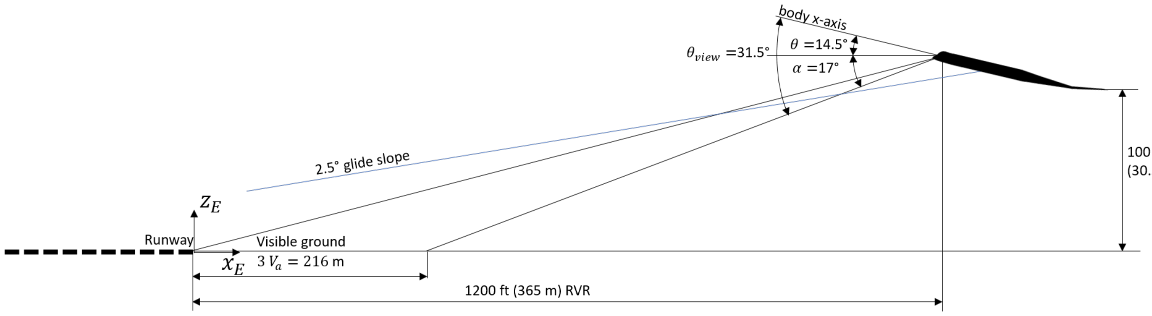

Figure 3.19: Required view angle at the pilot seat during landing

The Flying V requires an angle of attack of $\alpha = 17°$ [18] during landing. This means that a pitch angle of $\theta = 14.5°$ is required if a glide slope of 2.5° is attained. At this attitude, it is important to determine the height difference between the lowest point of the aircraft and the design eye point. The lowest point of the aircraft is set to be the extended main landing gear, from which all information is known from the design of the Flying V landing gear by Bourget[18]. As seen in fig. 3.20, the effective height difference between the pilot and the main landing gear is defined by four components, while the airplane body reference frame is rotated by the pitch angle with respect to the Earth reference frame. The first component to the height difference is that created by the landing gear wheel radius, which is 0.70m. Second is the vertical distance created by the vertical positioning of the landing gear. To compute this, the main landing gear leg length and the pivot position are taken into account. The leg length is 6m, where the placement of the pivot point is 0.658m down in the body reference frame. Therefor, the vertical distance in the tilted attitude is:

$$dh_{landing_z} = (z_{landing} + l_{landing})\cos\theta = (0.658 + 6)\cos 14.5° = 6.45m \tag{3.11}$$

The third contribution to the pilot height difference is the distance from the main landing gear pivot to the pilot design eye point along the aircraft body x-axis. The horizontal position of the main landing gear pivot point is given to be 31.5m from the body reference point. The position of the design eye point is defined relative to the center windshield point as seen in fig. 3.7 and is given by $l_{\text{window}} + l_{\text{DEP}}$ and $h_{\text{window}} + h_{\text{DEP}}$ for the horizontal and vertical position respectively. The contribution to the height difference is:

$$dh_{\text{landing}_x} = (x_{\text{landing}} - (l_{\text{window}} + l_{\text{DEP}}))\cos\theta \tag{3.12}$$

The final part of the height difference is given by the vertical positioning of the design eye point:

$$dh_{\text{pilot}} = (h_{\text{window}} + h_{\text{DEP}})\sin\theta \tag{3.13}$$

For example, if the design eye point is positioned 3.8m horizontally and 1.14m vertically, the distances above would equal $dh_{\text{landing}_x} = 6.9$m and $dh_{\text{pilot}} = 1.1$m. Summing all components, including the landing gear wheel radius, results in a design eye point height from the runway of $h_{eye} = 45$m.

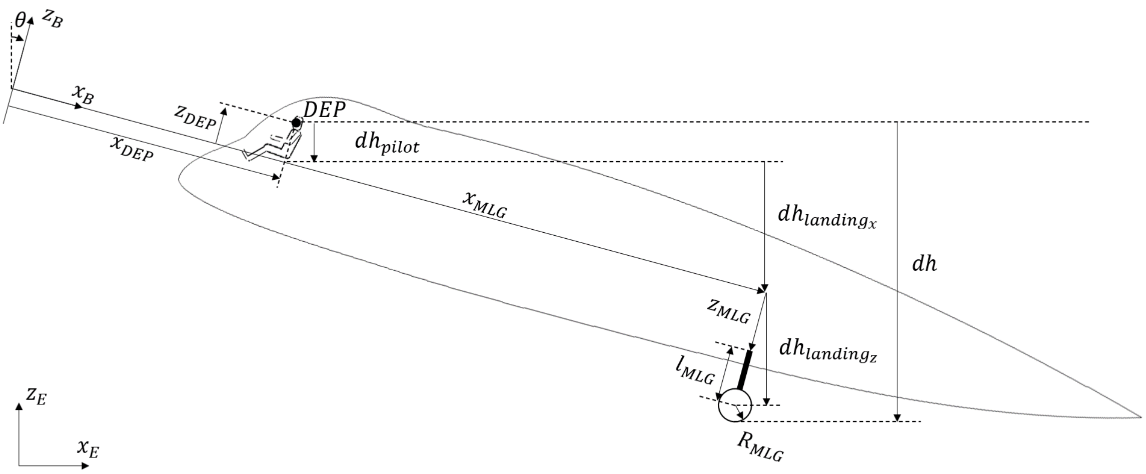

Figure 3.20: Pilot position with respect to the aircraft lowest point

After the vertical distance between the runway and the design eye point is known, the horizontal distance needs to be determined between the design eye point and the point to where the pilot requires vision. This distance is determined using the approach speed of the aircraft during approach. The approach velocity of the aircraft is $V_{\text{approach}} = 140\text{kts} = 72\text{m/s}$[18], which results in a visual runway distance of 216m. The downward view angle can now be calculated using:

$$\theta_{\text{view}} = \arctan\left(\frac{h_{\text{eye}}}{365.76 - 3V_{\text{approach}}}\right) + \theta = \arctan\left(\frac{h_{eye}}{365.76 - 216}\right) + 14.5^{\circ} \tag{3.14}$$

Using the example pilot position, a view angle of 31.5° is required measured from the design eye point. This view angle must be achieved during normal approach, but also when the aircraft yaws to the left when a cross-wind of 10kts is present. This results in an angle from the vertical plane of ±4.1°. However, Torenbeek recommends this angle to be ±10°[16]. The larger of the two is used in the determination of the required view-field, and is shown in Figure 3.18 in horizontal hatches.

The minimum required windshield that satisfies the above view-field requirements is made using the class `MinimumWindshield`. This class uses the pilot compartment view angles described above by retrieving these from the class `VisibilityPlot`, which also calculates the downward view angle needed during landing. These angles are passed to the class `VisibilityPane` to create the two window entities that satisfy the view from the design eye point at the captain's and the first officer's position. The creation of these window entities is performed by retrieving the common shell between a solid view-field emitted from the respective design eye point, made using the class `PilotViewfield`, with the cockpit shell. This method is shown in more detail in fig. 3.21.

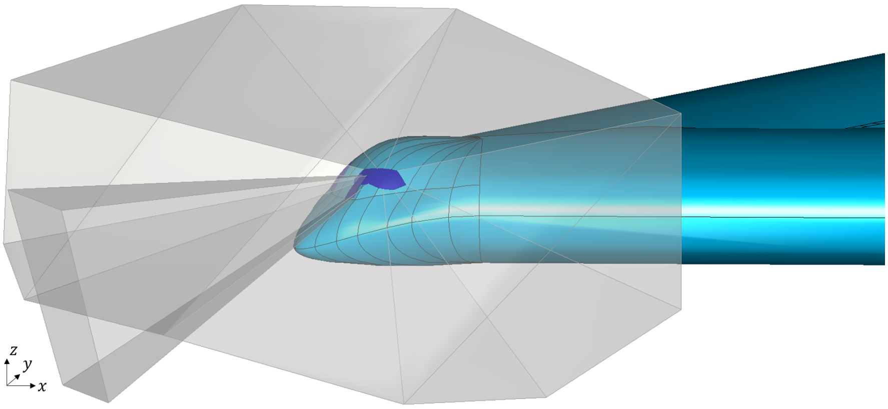

Figure 3.21: The minimum required windshield (dark blue) is made using the common surface between the solid pilot view-field (grey) emitted from the DEP and the cockpit shell (light blue).

The resulting windshield provides the absolute minimum view that is required to be provided to the pilots, but it may not be practical. For this reason, the minimum windshield is expanded using the class `RealisticWindshield`. The realistic windshield fuses the two windows using a center piece that connects these at the top and bottom. Flexibility herein is provided so that the user can change the height at which this center piece starts and ends, as seen in fig. 3.22.

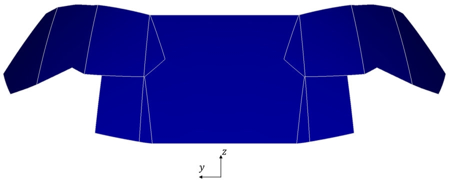

(a) windshield using a transition to connect both windows

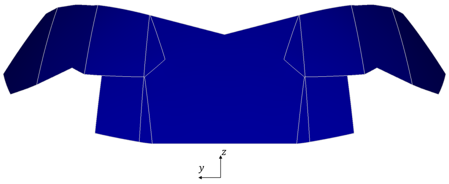

(b) windshield with changed top center point

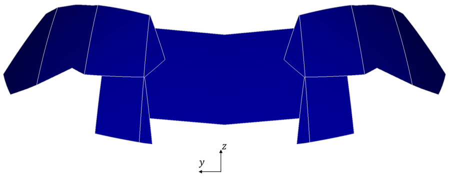

(c) windshield with changed attachment points to the minimum windshield, and changed center points

Figure 3.22: Realistic windshields using different start and end heights, as well as changing center points as seen from the front of the aircraft

Even though the functional requirements described above are always satisfied, since the windshield geometry results from these requirements, there is still one constraint that applies to the geometry. This constraint prescribes that the windshield is only to be cut from the shell formed by the aft top curve described in section 3.1.2. If it were to cut the front top curve, a sharp angle would result and the windshield could become excessively large or unrealistic. In order to assess this, the windshield is cut from only the shell formed by the top aft curves, and the area of the resulting windshield is compared to that of the complete windshield. If these are the same, then the windshield is deemed valid. The constraint can be described using the following:

$$h_{\text{windshield}}(\mathbf{x}) = \frac{S_{\text{windshield,top,aft}}}{S_{\text{windshield}}} - 1 \tag{3.15}$$

3.2.2. PILOT ANTHROPOMETRY

In order to design a cockpit, enough room should be allocated to provide a workspace for the pilot. However, since not all humans are the same, the topic of anthropometry plays an important role. Anthropometry is defined as "the science of obtaining systematic measurements of the human body"[2]. Results from anthropometric research include the sizes of different parts of the body for a given percentile of the population. For this research, data from the Human Factors Design Guide (HFDG)[24] is used, of which the applicable data is given in appendix C. However, some of the measurements required to make a human model are not included in the guide. To fill the gap in information, use is made of the Man-System Integration Standards to fill in the missing information[25]. Using anthropometric measurements from different sources may introduce errors in the human model, however, since the data concerns mostly information, such as the thickness of an arm or leg, the combined data is deemed accurate enough for it to fulfill the indicative purpose of the model.

Since the Flying V requires the CS 25 certification specifications, it is stipulated that pilots ranging from 1.58m to 1.91m should be able to pilot the airplane [15]. Additionally, it is decided that the 5th and 95th percentile of the human population should also be accounted for to provide a wide enough range of pilot sizes, in case the requirements of CS 25 do not overrule these. Since the data shown in table C.1 is split by gender, it is not possible to take the data for the human population as a whole. Therefor, the data for the female populace is chosen to represent the smaller of the pilot models, where the male sizes will be used for the larger model. It can be seen that the standing height of the 99th percentile male comes closest to the 1.91m requirement from CS 25 for the Human Factors Design Guide. However, the same applies for the 95^{th} percentile model from the NASA source. Therefor, the 99^{th} percentile model from the Human Factors Design Guide is chosen for the larger human model, where the 95^{th} model from the Man-System Integration Standards supplements the data where needed. The standing height of the 5th percentile women is smaller than the required 1.58m in the Human Factors Design Guide. This means that the female 5th percentile data will represent the smaller of the human models.

Now the pilot sizes are known, the pilot geometry can be made. The pilot geometry is approximated using rounded boxes, represented by the class `PilotBodyPart`, to estimate if there is enough room for the pilot to sit, as shown in fig. 3.23. In addition, a recommendation is given by Torenbeek that an additional 20cm is required around the design eye point to provide enough headroom. This is modelled as a sphere around the design eye point and must be completely included in the geometry. However, since the current model produces the outer mold line, the isolation thickness still needs to be included. The numbers for isolation thickness are found to be in the range of 8.8-11.6cm [17]. This is added to the previously mentioned 20cm in the determination of the available headroom.

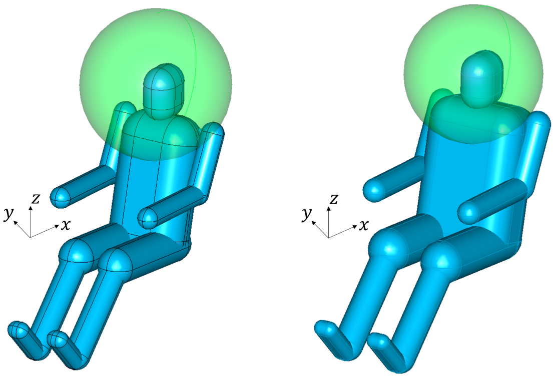

(a) Female 5^{th} percentile (b) Male 95^{th} percentile

Figure 3.23: An example of a pilot model (blue) including a 30cm headroom margin (green)

Finally, Torenbeek recommends that the distance from the design eye point to the windshield is between 0.5m and 0.6m. At this point, the angle of the windshield with respect to the horizon should be at least 35°.

---

[2] https://biologydictionary.net/anthropometry/ Retrieved: 10 January 2021

This is to prevent a loss of the effective transparent qualities of the windshield when looked through at small angles. This constraint is visualised in fig. 3.24. It must be noted that this is not a strong requirement, however, since it contributes to a good design it is included in the constraints.

The first two constraints follow from the total inclusion of the pilot geometry. In Parapy, this means that the volume of the common solid, $V_{\text{common}_{\text{pilot,cockpit}}}$, needs to be that of the pilot geometry V_{pilot}. If it is less, it means that part of the geometry is located outside the cockpit geometry and the constraint is violated. Therefor, the pilot inclusion can be written as:

$$h_{\text{pilot}}(\mathbf{x}) = \frac{(V_{\text{common}})_{\text{pilot,cockpit}}}{V_{\text{pilot}}} - 1 \tag{3.16}$$

The available headroom is determined in a similar manner, and can be written as:

$$h_{\text{headroom}}(\mathbf{x}) = \frac{(V_{\text{common}})_{\text{headroom,cockpit}}}{V_{\text{headroom}}} - 1 \tag{3.17}$$

The final constraints apply to the horizontal distance between the design eye point and the windshield $l_{viewpoint}$, and the angle $\phi_{\text{viewpoint}}$ at this point:

$$g_{\text{l}_{\text{DEP,viewpoint,l}}}(\mathbf{x}) \leq 1 - \frac{l_{\text{viewpoint}}}{0.5} \tag{3.18}$$

$$g_{\text{l}_{\text{DEP,viewpoint,u}}}(\mathbf{x}) \leq \frac{l_{\text{viewpoint}}}{0.6} - 1 \tag{3.19}$$

$$g_{\phi_{\text{viewpoint}}}(\mathbf{x}) \leq 1 - \frac{\phi_{\text{viewpoint}}}{35^\circ} \tag{3.20}$$

3.2.3. NOSE LANDING GEAR

To determine whether the nose landing gear fits in the cockpit section, it must fit under the cockpit floor. In this way the landing gear well is not pressurized and there is a reduction in structural weight relative to the situation where it must be pressurized. Therefor, the floor must first be positioned. This is done using the vertical distance between the design eye point and the floor, which is composed of two parts. First is the sitting height. This is the vertical distance between the seat reference point and the eyes, and is taken for the female 5th and male 99th percentile model for a human. As shown in table C.1, the sitting height for the 5th percentile female human body is 68.5cm, where it equals to 86.9cm for the 99th percentile male, shown as z_{pilot} in fig. 3.24. The second component is the seat height, z_{seat}, which is the vertical distance from the seat reference point and the floor. This was found to be between 34 and 51cm [26]. Combining the results show that after adjusting the seat, both the larger and smaller percentile model provide a vertical distance from the design eye point to the ground of maximum 120.5cm. For this reason, the cockpit floor is positioned using this distance relative to the design eye point. Additionally, the floor thickness is taken to be 20cm[17].

After the floor is positioned, the landing gear is placed. The landing gear position depends on three variables. The first two variables are the horizontal and vertical placement of the pivot point with respect to the aircraft origin, as seen in fig. 3.24. The third variable is the angle at which the nose landing gear rests in the aircraft. Then the nose landing gear geometry can be modelled. The gear wheel is modelled using the dimensions of the well where it lies in. The well diameter is 1.16m and is 1.21m in width[18]. The gear length is 6m from the pivot to the wheel center.

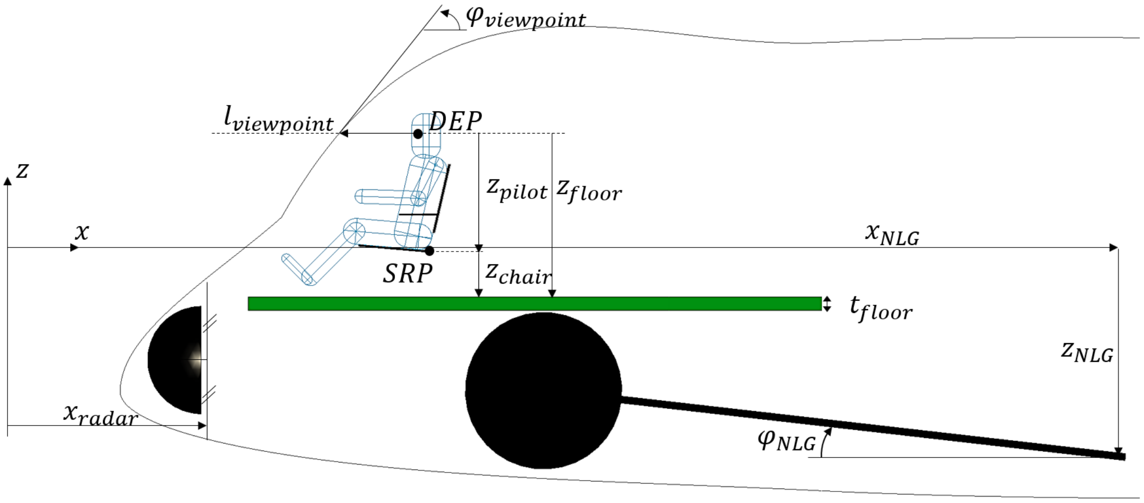

Figure 3.24: Positioning of the design eye point, cockpit floor, nose landing gear and radar antenna. Additionally, the windshield constraints are shown that apply the the height of the DEP

Finally the nose landing gear constraints can be made. The first determines whether the landing gear is fully enclosed in the cockpit geometry:

$$h_{\text{NLG,enclosed}}(\mathbf{x}) = \frac{(V_{\text{common}})_{\text{NLG,cockpit}}}{V_{\text{NLG}}} - 1 \tag{3.21}$$

Where $(V_{common})_{NLG,cockpit}$ is the common volume between the nose landing gear and the cockpit geometry, and V_{NLG} is the volume of the nose landing gear geometry itself. The second constraint checks if the nose landing gear is below the floor. This constraint uses the volume off the nose landing gear and the common volume $(V_{common})_{NLG,hss}$ between the nose landing gear and a `HalfSpaceSolid` enclosing the space from the bottom of the floor down:

$$h_{\text{NLG,floor}}(\mathbf{x}) = \frac{(V_{\text{common}})_{\text{NLG,hss}}}{V_{\text{NLG}}} - 1 \tag{3.22}$$

3.2.4. RADAR

The weather radar is positioned in front of the pilots, and is modelled after the Honeywell flat plate antenna[20]. The antenna has a diameter of 30 inch (76.2cm), and is represented by the front half of a sphere. The position is determined by the x-position, x_{radar}, of the back of this half-sphere, as can be seen in fig. 3.24. The half-sphere is then placed in the center of the local cross-section. The first constraint applies to the radar being inside the cockpit geometry:

$$h_{\text{radar}}(\mathbf{x}) = \frac{(V_{\text{common}})_{\text{radar,cockpit}}}{V_{\text{radar}}} - 1 \tag{3.23}$$

In this equation, $(V_{\text{common}})_{\text{radar,cockpit}}$ is the common volume between the radar half-sphere and the cockpit shell, and V_{radar} is the volume of the radar half-sphere itself.

To determine the bounds in which the radar can be positioned, it must be noted that the radar must always be in front of the pilots. The x-position at which the radar can be regarded to be in front of the pilot is assumed to be located 111.1cm in front of the seat reference point[16]. To this, an additional margin of 10cm is given. Therefore, the total minimum distance between the radar and the seat reference point is 121.1cm. This x-position represents the upper bound of the optimisation, where the lower bound is given by the nose of the aircraft.

The final constraint is to check if the radar is indeed located in front of the pilot's feet minus the $x_{margin,radar}$ margin. This constraint is defined by:

$$g_{\text{radar,position}}(\mathbf{x}) \leq \frac{x_{\text{radar}}}{x_{\text{pilot}} - x_{\text{margin,radar}}} - 1 \tag{3.24}$$

4

AERODYNAMIC ANALYSIS

One of the main results from the integration of the cockpit and center fairing design is the lift over drag ratio of the aircraft. This result can be used in an optimization of the model to determine a favorable shape for the cockpit and center fairing. An example of an objective function for such an optimization is seen in eq. (4.1):

$$f(\mathbf{x}) = \frac{C_L}{C_D} \tag{4.1}$$

Since the model is to be used in an optimization effort, the objective function will be called numerous times. This means that the computation time for one function evaluation should be limited as it will impact the total time required to optimize the shape.

As this research continues on that performed by Hillen [8], the method to assess the aerodynamic performance of the aircraft remains largely the same. In this research, use is made of Euler equations to compute the flow field in inviscid conditions. For this purpose use is made of the Stanford University Unstructured (SU2) solver [27]. The use of this software is explained in section 4.1. The inviscid results still need to be completed with their viscous counterpart. This is done using semi-empirical viscous methods. This method is further elaborated in section 4.2. Both the viscous and inviscid drag coefficients are added to form the total drag coefficient, as shown in eq. (4.2):

$$C_D = C_{D_{\text{inv}}} + C_{D_{\text{visc}}} \tag{4.2}$$

This will provide an estimation of the total drag coefficient by using the aforementioned methods, while still being fast enough to use the evaluation in an optimization.

4.1. INVISCID METHOD

The inviscid lift and drag coefficients are calculated by the Standford University Unstructured (SU2) tool. This is an open source software suite that is used to perform Partial Differential Equation analyses [27]. It features the possibility to perform Euler, but also RANS calculations. For this research, it is chosen to use the Euler computations, since these are generally faster than other types of calculations for the same domain size, which is a large advantage since the model is to be used in an optimization. The Euler equations result from a simplification of the Navier-Stokes equations. In the Euler equations, it is assumed that the flow is steady, and viscous effects are ignored [28]. This is an assumption that can be made, since the transonic flow means that a large Reynolds number is attained. This in turn causes viscous effects to be only important in a small region near the walls, and thus their effect is small as well as long as the flow remains attached [29]. In order to perform a Computational Fluid Dynamics (CFD) calculation, a mesh should be generated first. The mesh and the parameters with which it is generated will be provided in section 4.1.1. This is followed in section 4.1.2, where the configuration is shown with which the CFD is run.

4.1.1. MESH GENERATION

The mesh contains the geometry of which the evaluation is to be made. This is generated by using the integrated Parapy mesh library, which is in turn powered by the Salome package. The package provides a way to make an unstructured mesh automatically by providing it with the geometry to be meshed. Even though an unstructured mesh is less efficient in terms of resource usage and is known to be less accurate in comparison to a well made structured mesh, it is easier to make for complex geometries. Furthermore, for complex geometries it is recommended to use an unstructured mesh, since a structured mesh can have problems in the grid nonorthogonality or skewness, which can cause unphysical solutions [30]. An example of a mesh generated for the Flying V with cockpit and fairing geometry is shown in fig. 4.1. This mesh uses a very low count of elements to be able to show the mesh.

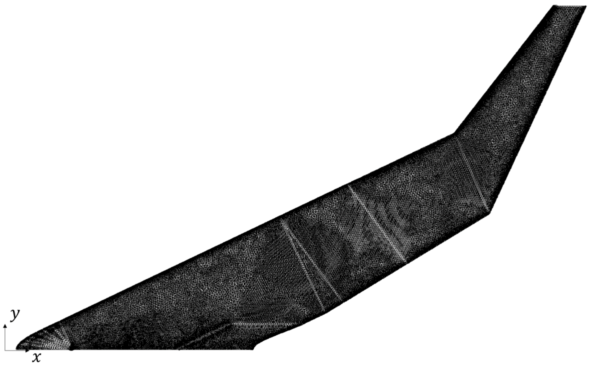

Figure 4.1: A mesh generated for the Flying V with integrated cockpit and center fairing using a low element count

In addition to the geometry, parameters ought to be supplied that, amongst others, describe the fineness of the mesh and the growth rate along different dimensions. These parameters are listed in table 4.1 and are the same as for the Flying V parameterisations performed by Hillen [8] and Faggiano is [3]. The default value is that as chosen from the grid convergence study discussed in section 4.1.3.

Table 4.1: Parameters used to create a mesh with their default value and element to which these apply

Parameter	Controls segments on	Default value
Nodes per length	Wing edges	15
Max size wing	Wing faces	0.1
Outer domain maxim	Outer domain faces	15.0
Triangular element growth rate	Faces	0.1
Tetrahedral maximum size	Volume	15.0
Tetrahedral growth rate	Volume	0.3

4.1.2. CONFIGURATION

The conditions at which the CFD must be run, such as the flight speed and height, but also the convergence criteria, are supplied to the solver by means of a configuration file. Additionally, this file contains the definition of the boundary conditions, which are split by three categories:

- Outer domain: here free stream conditions apply

- Symmetry wall: symmetry conditions apply at the symmetry wall

- Object: the object is defined too have Euler wall conditions

The three boundaries can also be seen in the computational domain in fig. 4.2.

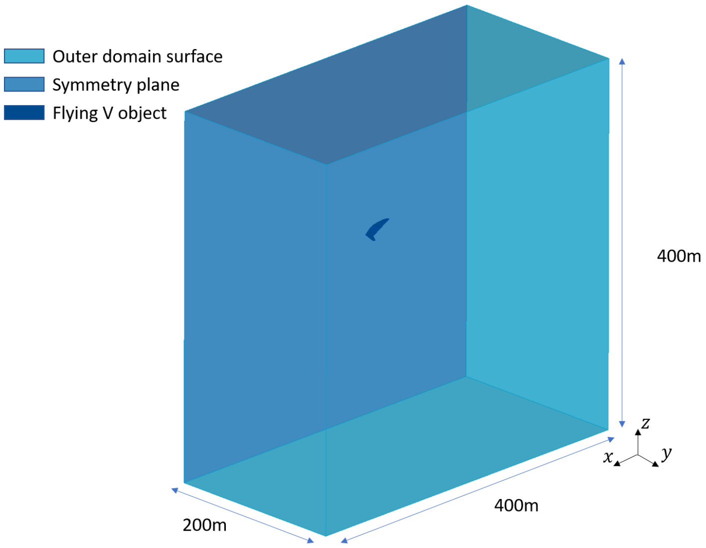

Figure 4.2: Computational domain used in the CFD calculations showing the three categories of boundaries: the outer domain, symmetry wall and the object (Flying V)

4.1.3. VERIFICATION

Verification of the SU2 analysis for the Flying has already been performed by Faggiano [3], who performed the analysis on an older version of SU2. In turn, Hillen [8] has performed a verification of a more current version of SU2 on the Flying V. The verification performed for this research is twofold: first, a grid convergence study is performed. This is carried out for cruise conditions, where the free stream Mach number $M = 0.85$ at an altitude of $h = 13,000$m while requiring a lift coefficient of $C_L = 0.266$. The grid convergence study was ran for the control settings shown in appendix D, of which the resulting inviscid drag coefficient is shown in fig. 4.3.

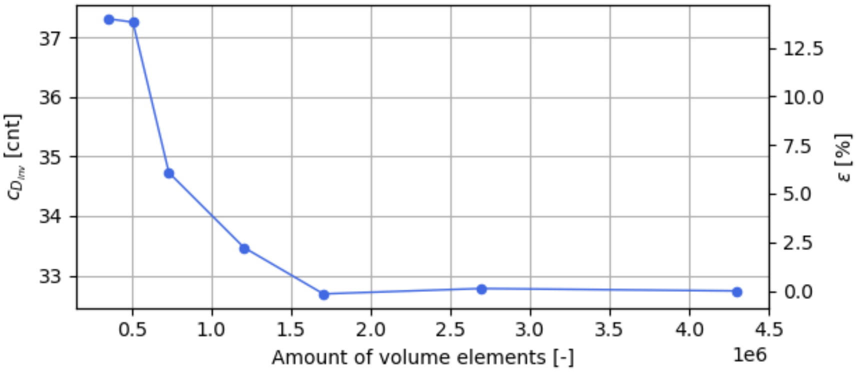

Figure 4.3: Grid convergence carried out for the original Flying V, showing the convergence of the inviscid drag coefficient computed by SU2 against the amount of volume elements in the grid. The error is relative to the result of the finest mesh

It can be seen that the inviscid drag coefficient $C_{D_{inv}}$ drops quickly when refining the mesh. The error ϵ, as seen on the right side of the figure, is relative to the value of the finest mesh:

$$\epsilon = \frac{C_{D_{\text{inv}}} - C_{D_{\text{inv}}}^{\text{fine}}}{C_{D_{\text{inv}}}^{\text{fine}}} \tag{4.3}$$

Where $C_{D_{\text{inv}}}$ is the inviscid drag coefficient calculated for a mesh and $C_{D_{\text{inv}}}^{\text{fine}}$ represents the inviscid drag

Table 4.2: Parameters used for aerodynamic validation where the cockpit and fairing domains are cut and reinserted into the cut geometry.

parameters	symbol	value	unit
cockpit end location	x_{cockpit}	6.7	[m]
aft tolerance	δ_{cockpit}	0.5	[m]
start location top	$x_{\text{fairing,top}}$	0.7	[-]
start location bottom	$x_{\text{fairing,bottom}}$	0.7	[-]
spanwise start location	b_{fairing}	5.7	[-]

coefficient for the finest mesh. The error is seen to stay in the range of 0.2 percent for the last three evaluations. For the remainder of this research, the settings used to generate the mesh with 1.7 million volumes is used to evaluate the aerodynamics, since the relative error is low and the computation time increases rapidly for the finer meshes.

The second verification is an analysis of the base geometry used for the analyses in chapter 5, where a section of the nose and center fairing have been cut and reattached to the geometry. This was to investigate the effect it has on the generation of the mesh and subsequent results. The results of this analysis are shown in table 5.2, and it is demonstrated that cutting the geometry does not influence the results to such extend that these would exceed the error caused by this or the other methods used. An example of the reattached geometry is shown in fig. 4.4, which was made using the parameters shown in table 4.2.

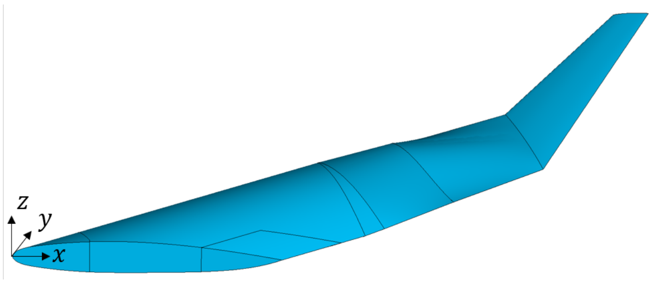

Figure 4.4: A reattached nose and center fairing to the base geometry used in this research

4.2. VISCOUS METHOD

The viscous drag estimation is meant to supply the viscous component of the drag coefficient to the inviscid part calculated by the SU2 analysis. This estimation method consists of four steps, and is based on the flat plate analogy, which is further explained in the works by Raymer and Torenbeek [16, 28]. Besides computing the wetted area of the shape, the skin friction coefficient is determined. This is done using the method explained in section 4.2.1. After the skin friction coefficient is known, the form factor is determined using the method shown in section 4.2.2. Using the form factor, the profile drag can be estimated in section 4.2.3. Lastly, the limitations of this method are discussed in section 4.2.4.

4.2.1. FRICTION COEFFICIENT

The first step of determining the viscous component of the drag coefficient of the aircraft and the aircraft components is to calculate the skin friction coefficient. This is done by analysing the local airfoil along multiple slices of the aircraft outer mold line in the direction of flight. This was already present for the base geometry, but the slices impacted by the cockpit and center fairing design are updated and used to determine the local drag coefficient components.

The skin friction coefficient for each of these slices is calculated using the equation given by Raymer for a turbulent flow[28], as shown in:

$$C_f = \frac{0.455}{(log_{10}R)^{2.58}(1+0.144M^2)^{0.65}} \tag{4.4}$$

In this equation, C_f is the skin friction coefficient, R is the applicable Reynolds number and M is the free stream Mach number. For a rough surface, the friction coefficient is higher than indicated by eq. (4.4). To accommodate for surface roughness, a cut-off Reynolds number for transonic or supersonic conditions is presented by Raymer[28], which is shown in:

$$R_{\text{cutoff}} = 44.62(l/k)^{1.053} M^{1.16} \tag{4.5}$$

In which R_{cutoff} is the cutoff Reynolds number, l is the characteristic length, k is the surface roughness value and M is the Mach number. The Reynolds number to be used in eq. (4.4) is the lower of the actual Reynolds number and the cutoff Reynolds number.

4.2.2. FORM FACTOR

Following the calculation of the skin friction coefficient in section 4.2.1 is the computation of the form factor. For a streamlined shape, this is defined by the following equation[16]:

$$FF = 1 + \phi \cos \Lambda_{1/2} \tag{4.6}$$

In this equation $\Lambda_{1/2}$ is the sweep angle at half chord, and the shape correction factor ϕ is defined in:

$$\phi = 2.7\frac{t}{c} + 100\left(\frac{t}{c}\right)^4 \tag{4.7}$$

Which uses $\frac{t}{c}$, the thickness to chord ratio of the local profile. However, the assumption is made that the shape is streamlined. For a cockpit shape this assumption is not valid as it mostly features a kink, and will therefor result in a penalty in the accuracy of the method.

4.2.3. PROFILE DRAG COEFFICIENT

After knowing the form factor of a strip, the profile drag coefficient can be calculated. This is done using the integral shown in eq. (4.8), which is based on strip theory. The strip theory assumes that the cross sections do not have any interaction with each other. This makes it possible to analyse the strips separately and sum up the results.

$$C_{D_p} = \frac{2}{S}\int_0^{b/2} c_{d_{\text{p}}} c\, dy \tag{4.8}$$

Where S is the reference surface area of the wing, $b/2$ is the half span, c_{d_p} is the strip profile drag of the local profile and c is the local chord length. The local profile drag coefficient is calculated using:

$$c_{d_p} = (c_{d_{\text{p}}})_{\text{min}} + \Delta_l c_{d_{\text{p}}} \tag{4.9}$$

In which $\Delta_l c_{d_{\text{p}}}$ is the drag increment for lift coefficients different from $c_{l_{\text{i}}}$. However, it is assumed that this factor is negligible because the calculations are performed at cruise conditions at which the aircraft is expected to fly at low lift coefficients.

Finally, $(c_{d_p})_{min}$ is calculated by using:

$$(c_{d_p})_{min} = 2C_f FF \tag{4.10}$$

4.2.4. LIMITATIONS

The flat plate analogy provides a means to estimate the influence of viscosity on the drag coefficient of a shape. However, this comes with a number of limitations and assumptions [16]. First is the limitation that the thickness to chord ratio of the airfoil sections should be below 25%. For body diameter to length ratios the method is limited to 25% to 35%. This limitation is satisfied for the default Flying V geometries, as well as for the geometry where the default cockpit and center fairing are fitted in.

The second limitation is found in the parts having a smooth surface contour, free from kinks or steps. It was already established that in the parameterisation used for this research [8] that this is not the case, and that this assumption is not satisfied, having an inaccuracy as a result. The same applies for the cockpit geometry, since it is designed to feature a possible kink at the bottom of the windshield. This limitation is not satisfied, however, for the purpose of optimisation it is more important to know the direction of the objective function, rather than the accurate value. In other words, the inaccuracy of the method is acceptable, as long as it provides an estimate of the viscous drag coefficient that is accurate enough for optimisation.

The third and last limitation of the flat plate analogy is that the angle of incidence, or the lift, is zero or small. Having the Flying V aerodynamic drag and lift analysed at cruise conditions satisfies the small angle assumption.

Concluding is an assumption regarding the strip theory. For this it is assumed that the strips do not influence eachother, which is plausible for straight wings for which it yields good results. However, for swept wings the method is open for criticism because of the cross-flow in the boundary layer [16]. Here the same arguments can be made which are described above. For this reason, the methods used are deemed satisfactory for this model.

4.3. ROOT EFFECT

The root effect consists of two parts: the root effect due to thickness, and due to lift. The component due to thickness is reduced by moving the thickest point of the root airfoil towards the leading edge, and increasing the thickness to chord ratio. The first is estimated by:

$$\Delta x = \frac{1}{2\sqrt{2}}\sqrt{1-\frac{1}{\sqrt{1+f(\phi)^2}}} \tag{4.11}$$

Where Δx is the change in location of the thickest point and $f(\phi)$ is a function of the sweep angle and is defined by:

$$f(\phi) = \frac{1}{\pi}\ln\frac{1+\sin\phi}{1-\sin\phi} \tag{4.12}$$

The change in thickness to chord ratio is estimated by:

$$\frac{t}{c} = \frac{(t/c)_{\mathrm{s}}}{\tau}\frac{\cos\phi_s}{\cos\phi}\frac{1+\sqrt{1+f(\phi)^2}}{2+\frac{1}{2}\pi f(\phi)^2} \tag{4.13}$$

Where t/c is the thickness to chord ratio of the adapted root airfoil, $(t/c)_{\mathrm{s}}$ is the thickness to chord ratio of the original root airfoil and τ is a reduction factor in case taper is present. Lastly, ϕ and ϕ_s are respectively the sweep angles at the root and the outer wing.

It can be assumed that the adapted root airfoil blends in the rest of the aircraft shape at around $y = c/2$. Then the eq. (4.11) and eq. (4.13) can be simplified to the following equations:

$$\Delta x = \frac{\phi}{2\pi} \tag{4.14}$$

$$\frac{t}{c} = \frac{(t/c)_{\mathrm{s}}}{\tau}(1+0.1\phi_{\mathrm{s}}^2) \tag{4.15}$$

Using these equations with $\phi = 64.5°$ and $\tau = 1$ results in a movement of the thickest location of $0.18x/c$ and an increase of the root thickness to chord ratio of 13%.

The root effect due to lift is reduced by increasing the angle of twist and by reducing camber. The change in camber line is described with:

$$z_{\lambda_1} = \frac{1}{2\tan(\pi n)}\frac{\cos\phi}{\cos\phi_{v_{\lambda_1}}}\alpha_{e_s}\left[\frac{\pi}{2}(1-2x)-\sin^{-1}(1-2x)+\sqrt{1-(1-2x)^2}\right] \tag{4.16}$$

Where z_{λ_1} is the downward z-coordinate of the camber line at position x. Furthermore, ϕ and $\phi_{v_{\lambda_1}}$ are the sweep angle and the sweep angle along a vortex filament along the chord, and $\alpha_{\mathrm{e_s}}$ is the effective angle of attack at which the airfoil is evaluated. Lastly, the factor n can be determined using:

$$n = \frac{1}{2}\left\{1-\frac{\phi}{\pi/2}\right\} \tag{4.17}$$

Finally, to calculate the required twist angle at the root, the required effective angle of attack at the root needs to be determined. This is done using the following equation:

$$\alpha_{\mathrm{e}_{\lambda_1}} = \frac{\cos\phi}{\cos\phi_{\mathrm{v}_{\lambda_1}}}\left(1+\frac{\pi}{2}\tan\phi\right)\alpha_{\mathrm{e_s}} \tag{4.18}$$

5
RESULTS

The discussed models for the cockpit and center fairing are used on the Flying V geometry developed by Faggiano using the parameterisation of Hillen [8]. First, the robustness of the models is discussed in section 5.1. This will be done for the cockpit and center fairing separately. Following is the application of the model in section 5.2. Here, three cases will be shown which cover the application of the root effect airfoil changes, as well as the integration of the cockpit and center fairing.

5.1. ROBUSTNESS

The robustness of the defined geometrical models is determined by means of sampling the design space and examine whether the result is a valid geometrical shape, as explained in section 3.1.4. The process of sampling and calculating the robustness is repeated for a set of sample sizes. The results for the cockpit can be seen in fig. 5.1. The first results are those obtained for the cockpit geometry with the `try_fix` option, as discussed in section 3.1.2, turned off. The second result shows a robustness as calculated for the the cockpit geometry with the `try_fix` option enabled.

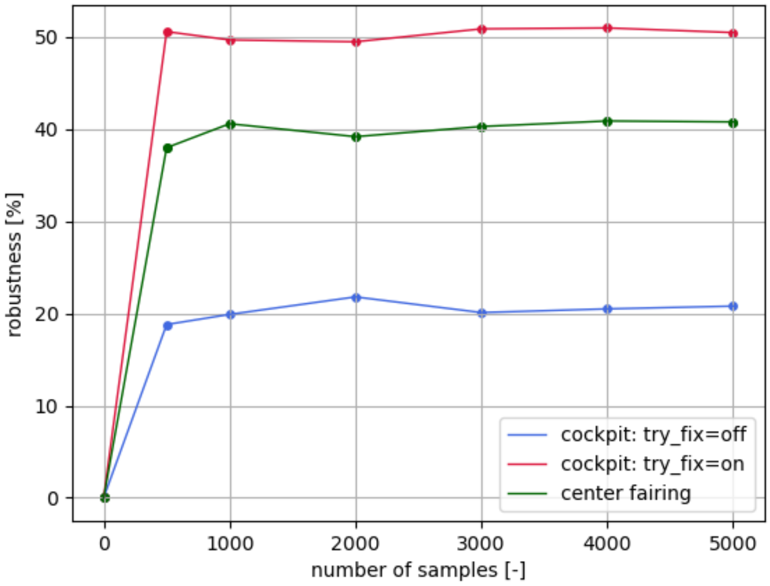

Figure 5.1: Robustness sample study for the cockpit and center fairing geometry using LHS sampling. The cockpit robustness is shown with the try_fix option set on or off

As can be seen, the robustness cockpit model with the `try_fix` option turned off was lower than when it was on. The robustness of the more precise model has shown to be 20.3% on average, where the less accurate model has an average robustness figure of 50.4%. This is much higher and therefor it can be used in an optimization routine to first find a region where a more precise geometric model is desired. At this point, the `try_fix` option can be turned off.

Besides the robustness for the cockpit model, there is also that for the center fairing, for which the results can be seen in section 5.1. The results show that the robustness of the fairing model is 39.9% on average, and oscillates between the bounds of 38.00% and 40.88%. Furthermore, it must be noted that executing a robustness analysis helps in detecting errors in the coding of the application. The robustness started at 10%, but climbed up to 20% for both the cockpit and fairing models after finding solutions to increase robustness as well as bugfixes.

A collection of images can be found in appendix E in which an impression is given of the design space. It features a total of 200 images of the successful samples of the robustness analysis.

5.2. APPLICATION OF THE MODEL

In this section, the application of the discussed model will be shown. This will be done through the use of three cases. The first case serves a pure aerodynamic objective, and will cover a potential reduction of the root effect by use of the cockpit and center fairing models. The second case includes a functional cockpit design, in which the constraints, as covered in section 3.2, are satisfied. The third case features a central fairing design which focuses on a realistic integration of such design. All cases serve as an application of the models, for which the input parameters are provided in appendix F, instead of providing the best possible aerodynamic or functional shape. Furthermore, the flight condition used for all cases is that of cruise. This means a free stream Mach number of 0.85 at an altitude of $h = 13,000$m was used and a lift coefficient of $C_{L_{\text{ref}}} = 0.266$ had to be attained. The latter may change slightly because of rounding in combination with CFD results, as the lift coefficient from these results will be given later in the section.

5.2.1. CASE I: ROOT EFFECT

The first case focuses on countering the root effect. To reduce this effect, a number of changes are required to be made on the root airfoil and are grouped in two categories. First is due to the root effect due to thickness, and include a change in thickness to chord ratio and the position of the thickest point as described by Küchemann [13]. The second component is discussed by Brebner [14], and includes the airfoil change caused by the root effect due to lift, and requires a decrease in airfoil camber and an increase in twist angle. The methods to estimate the airfoil changes are given in section 4.3.

The first component, the airfoil change caused by the root effect due to thickness, is estimated using the aircraft sweep angle and a reduction factor for taper. Using the inner sweep of the Flying V of $\phi = 64.5°$ and a reduction factor of $\tau = 1$ results in a movement of the thickest location of $\Delta x = 0.18$x/c and an increase of the root thickness to chord ratio of 13%.

The second component is caused by the root effect due to lift. The airfoil required change is estimated using the effective angle of attack, which is that of the aircraft plus the twist angle of the root airfoil. The angle of attack of the aircraft is 4.5° for cruise, as determined using the Flying V model of Faggiano in the parameterisation of Hillen. The twist angle of the root airfoil was found to be 0.8°, resulting is an effective angle of attack of 5.3°. This results in a required effective angle of attack of 9.84°, and thus a twist angle of 5.34°. Furthermore, the required airfoil camber can be seen in fig. 5.2, where a maximum reduction in camber is found to be 0.047z/c.

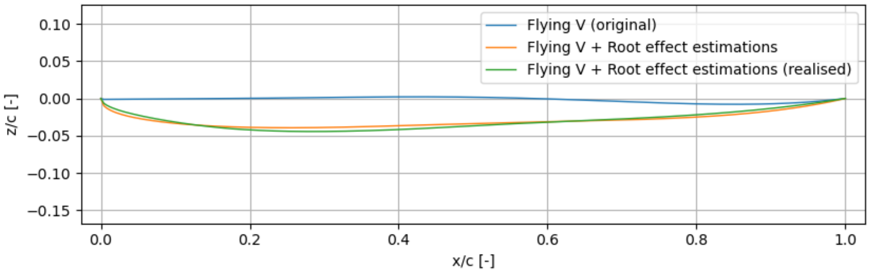

Figure 5.2: Change in camber line required as per [14], together with the original and achieved camber

The thickness ratio and location of the thickest point of the achieved airfoil and the desired figures are summarized in table 5.1 together with the effective angle of attack and twist angle. It is shown that the provided case does not fit the desired shape perfectly. Especially the location of the thickest point is difficult to move in the proposed parameterisation, as the camber is easy to change with it. An impression of the design for this case can be seen in fig. 5.3, which uses the parameters shown in table F.1 and table F.2.

	original root airfoil	original root airfoil + root effect estimations	adapted root airfoil (realised)
$x_{t/c}$ [-]	0.378	0.199	0.265
t/c [-]	0.145	0.164	0.167
α_e [°]	5.33	9.84	9.70
θ [°]	0.83	5.34	5.20

Table 5.1: Various airfoil parameters for the root airfoil of the original and adapted geometry and the goal set by the root effect equations described above

Figure 5.3: Design of the cockpit and center fairing when resolving the airfoil changes required to reduce the root effect

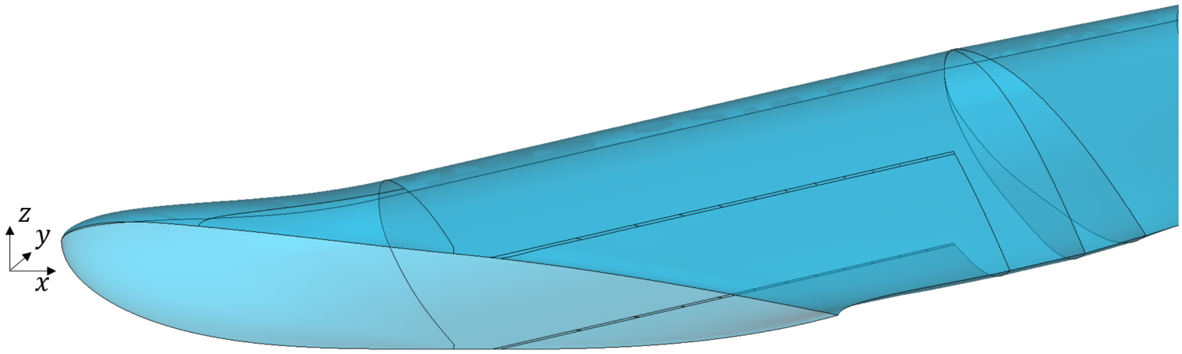

AERODYNAMIC RESULTS

The results from the aerodynamics module provide the values for the drag coefficient and its breakdown as shown in table 5.2. The results show an increase of 0.39% in the lift to drag ratio. The increase is mainly due to the reduced inviscid drag component, but is almost entirely countered by the increased viscous component. The total difference in drag coefficient between case I and the original geometry is 0.2 drag count.

On the root airfoil, a low pressure area situates at the top surface of the nose, and the high pressure area at the bottom is slightly larger than for the original, as can be seen in fig. 5.4. Furthermore, behind the low pressure area on the top surface a higher pressure area is identified. This area is located at a relatively flat section of the airfoil, introduced by the high negative camber applied to the root airfoil. Applying less negative camber may reduce this effect and increase local curvature, prolonging the low pressure area further aft on the airfoil. However, while isobars may be better aligned by lowering the pressure at this area, it may result in additional drag since it is located behind the top of the airfoil, providing a suction force. At the same chordwise position on the bottom surface, a low pressure area is seen. This is due to the increased curvature relative to the original root airfoil at this point. To increase local lift, it may be considered that the 'belly' of the airfoil can be reduced. However, this also plays with the thickness to chord ratio and the position of the thickest point, deviating from the geometric results obtained by the method described in section 4.3

It can be seen that behind the relatively flat area, at around 50% of the chord, the pressure distribution continues at a comparable level as the original. The pressure distribution can be seen to oscillate slightly, however it must be noted that the CFD solution was converged. This behaviour is likely caused by the proximity of the transitions from the cockpit shell to the base wing geometry and that from the base wing geometry to the center fairing, which are located close together. Providing more room between these transitions may result in a smoother pressure distribution. The solution from 60% of the chord onward shows the results of the center fairing. Here it can be seen that the inverted pressure difference between the top and bottom surface is smaller, reducing a loss of lift relative to the original pressure distribution in this area.

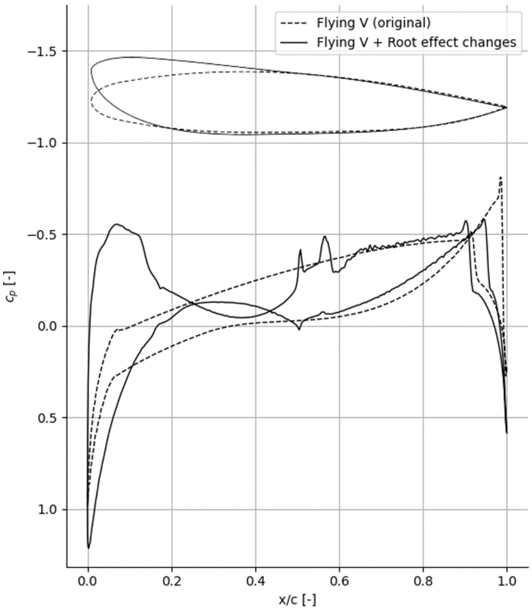

Figure 5.4: Pressure coefficient plot for the Flying V using an adapted root airfoil to reduce the root effect (M=0.85, h=13,000m, $C_{L_{\text{ref}}}$=0.266)

Additionally, the influence of the change in root geometry can be seen on the isobars on the aircraft planform, shown in fig. 5.5. These figures are shown in appendix G in a larger format. It can be seen that the low pressure area near the nose at the root causes the isobars in this region to align more to the local sweep angle. This, combined with the high pressure area at the bottom, help at providing additional lift at the root, while giving a small total increase in inviscid drag. The high pressure area that follows produces the adverse effect, reducing lift at this section of the root airfoil. Furthermore, it can be seen that the fairing does not influence the isobaric pattern noticeably. This may be due to the value of $R_{fairing}$ being small. Lowering the trailing edge would result in a change in the isobars, however, it would also increase the twist angle. Keeping twist constant, the leading edge would have to be lowered, causing an increase in camber, which was the opposite of the airfoil change required to reduce the root effect. Another option would be to change the free parameters of the fairing cross-sections. These have shown to mainly alter the curve at the trailing edge instead of at the attachment line. This is due to the constrained nature of the curves and would not help in shifting the isobars forward.

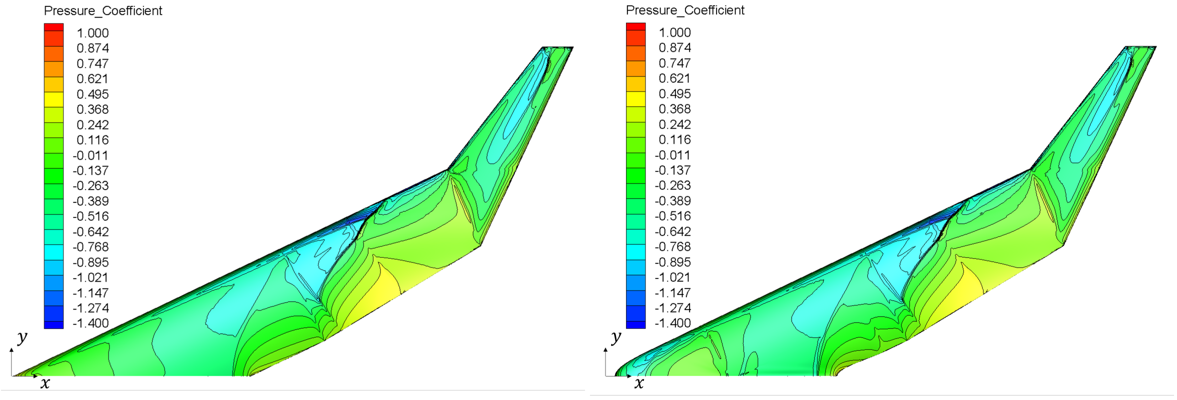

(a) Flying V (original)

(b) Flying V with root airfoil adaptations

Figure 5.5: Isobars for the original geometry and the geometry using an adapted airfoil to satisfy the airfoil changes required to reduce the root effect (M=0.85, h=13,000m, $C_{L_{\text{ref}}}$=0.266)

Finally, the result of the root airfoil adaptation is that the lift at the root is increased, as indicated by the orange line in fig. 5.6a. It can be seen that the result is localised and increases lift until 15% of the wing span, where the cockpit geometry ends. The increase in lift at the root is determined to be up to 11% relative to the original Flying V. The drag coefficient follows the increased lift at the root slightly, as seen in fig. 5.6b. However, it drops below the value for the original Flying V between 10% and 17% of the half span.

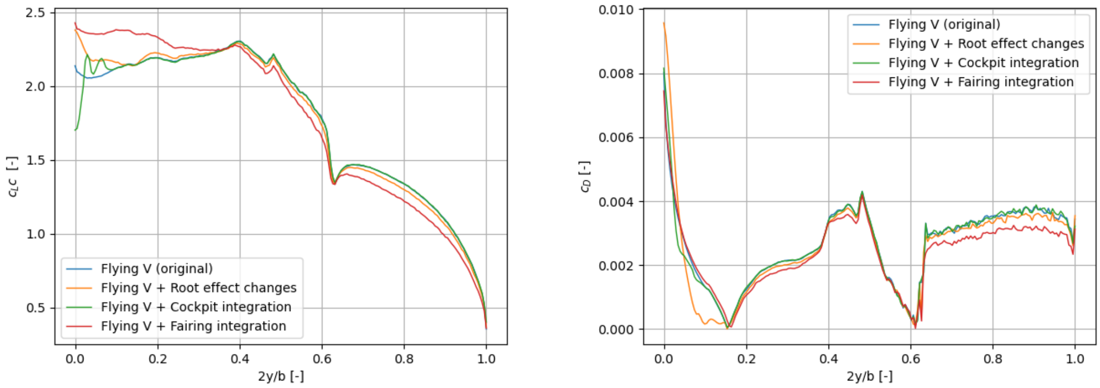

(a) Lift distribution along the semi span

(b) Drag distribution along the semi span

Figure 5.6: Drag coefficient and lift distribution over the halfspan of the original Flying V geometry (blue), and the Flying V where the root airfoil is adapted to reduce the root effect (orange), a cockpit is integrated (green) and with an integrated center fairing (red) (M=0.85, h=13,000m, $C_{L_{\text{ref}}}$=0.266)

5.2.2. CASE II: COCKPIT INTEGRATION

The second case provides a design for the cockpit. The main aim of this design is to provide a potential shape to satisfy the constraints defined in section 3.2, such as being able to accommodate the pilots, nose landing gear and radar, and to provide a wide enough vision for the pilots through the windshield. The design, shown in fig. 5.7, features seven sections and a near straight windshield line as seen from the top. This line curves aft at the outboard position of the pilots and curves back to fit the original airfoil at the end of the cockpit shape. This was done to provide smaller windows and to have the possibility for large overnose angles. The design also features a relatively high cockpit. This is required to provide enough headroom for the pilots, as a minimum of 20cm is required to which the isolation thickness of the cabin is added. The parameters used for this case are shown in table F.3:

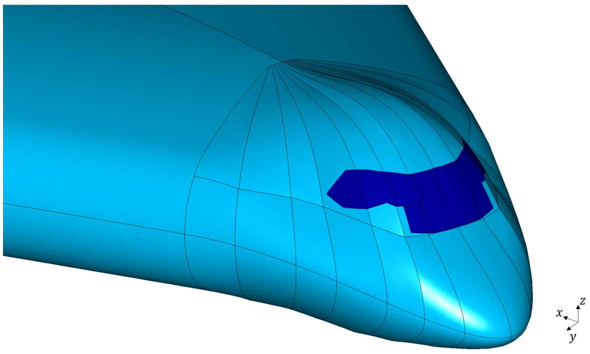

Figure 5.7: The cockpit design integrated in the original geometry used for the second case

GEOMETRICAL RESULTS

The geometrical results of the cockpit analysis include a verification of the various constraints laid out in section 3.2, such as the pilot visibility angles from the design eye point, the available room for the pilots, radar installation and nose landing gear.

The visibility angles from the design eye point are first computed using the windshield. This provided the view from the captain's seat as shown in fig. 5.8. It is shown that the windshield is made larger in this example to have a single window in front of the pilots. The windows could also have been separated at the 20 degree mark port of the captain, but this would result in two separate window entities. Furthermore, it can be noticed that the windshield has a small cut at the bottom. This is to allow the pilots to look over the nose of the aircraft at approaching the runway during landing. The total realistic windshield area is equal to 2.27 m^2, where the area of the minimum windshield is equal to 2.07m^2. Both are is smaller than that of an A320 [31] which compares to 2.36 m^2 of total windshield area. The windshield area of an A350 is, upon pixel measurement, determined to be approximately 2.3m^2. For this pictures of the cockpit were used in combination with known measurements, such as the fuselage diameter. This indicates that the windshield size is in the correct order of magnitude respective to the windshields of existing aircraft.

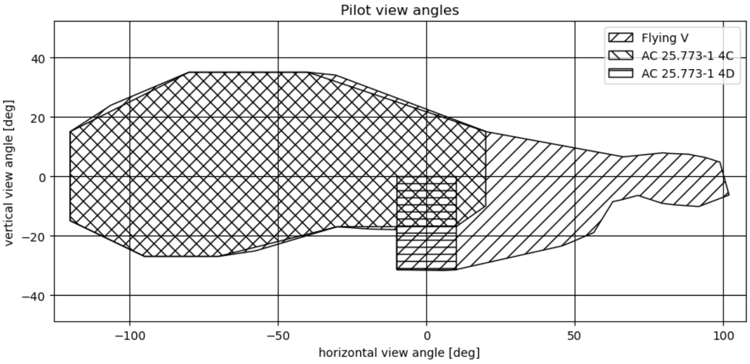

Figure 5.8:]

View angles attained from the design eye point at the captain's seat (right facing hatches show the angles resulting from the realistic windshield, left facing hatches show the required view angles as stipulated by AC 25.773-1 4C, where horizontal hatches represent the required landing view described in AC 25.733-1 4D)

Furthermore, the floor position is determined to be 1.195m down from the design eye point[24], resulting in the configuration shown in fig. 5.9. As can be seen, the nose landing gear can still fit underneath the pilot station and there is ample room for the weather radar in the nose. The windshield is at a distance of 50.5cm from the pilot under an angle of 46.5°. These figures satisfy the constraints discussed in section 3.2. Furthermore, there is enough room above the pilot to account for 12cm of insulation and 20cm of headroom.

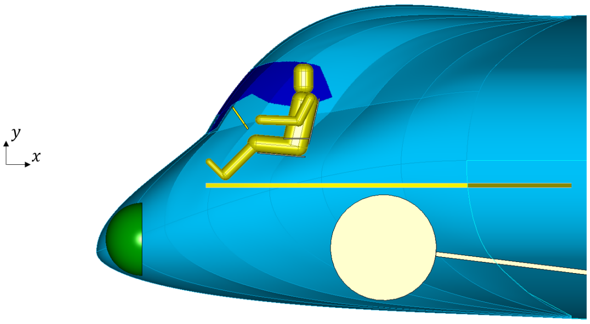

Figure 5.9: Cross section of the cockpit showing the pilots, floor, nose landing gear and radar installation

AERODYNAMIC RESULTS

The aerodynamic results for the integrated cockpit design are shown by the pressure distribution of the root airfoil in fig. 5.10, as well as the 3D pressure and Mach contours in fig. 5.11. In these results, three features can be noted. Firstly, a high pressure area situates at the nose of the aircraft, as can be seen in fig. 5.11a. This is expected because of stagnation at the leading edge of the root airfoil, which is confirmed by a low local Mach number. This causes a high pressure coefficient and with it additional drag. The velocity may be increased by using a longer, more slender nose section (decreasing the x_{nose} parameter). However, this will interfere with the constraint of having a sufficient overnose angle. Secondly, a high pressure area is seen at the windshield kink at the root, characterised by the sharp peak in the pressure distribution. This sudden change in pressure can trigger turbulence, causing noise in the flightdeck.

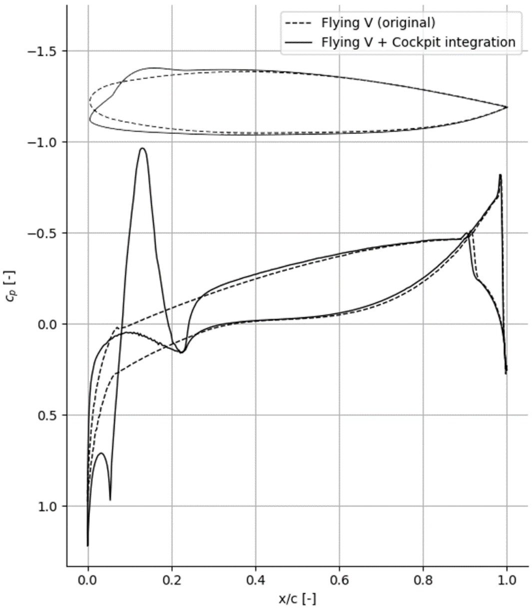

Figure 5.10: Pressure coefficient plot for the Flying V with integrated cockpit design (M=0.85, h=13,000m, $C_{L_{\text{ref}}}$=0.266)

Thirdly, a low pressure area can be seen on top of the cockpit, shown as a large peak in the pressure distribution. This is due to the high local Mach number, as shown in fig. 5.11b, and shown larger in appendix G. This could cause separation at high angles of attack and high velocities, however, using the current methods this is hard to predict accurately. The super-velocity at the top of the cockpit can be reduced by lowering the bulge. However, this would cause the headroom reserved for the pilot to shrink below the constraint value. A possible solution for this may be to adapt the parameterisation such that two curves are used for the current aft curve on the top (between the p_{top} and p_{window}), instead of one. This brings in more design flexibility and may provide better aerodynamic results, but it also brings additional parameters which will make a future optimisation take longer.

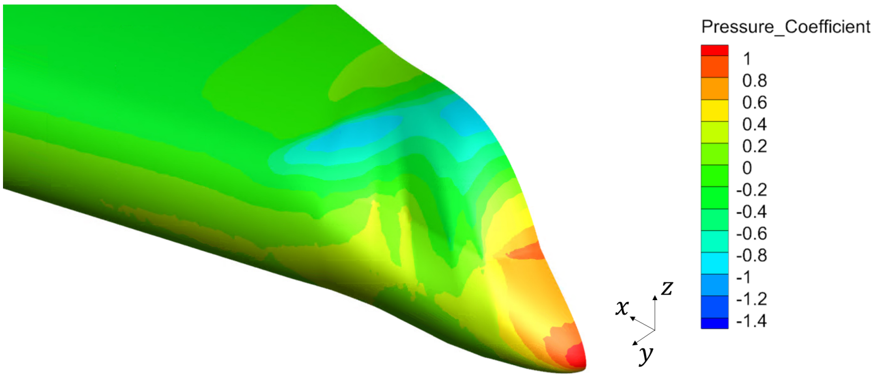

(a) Pressure coefficient contours

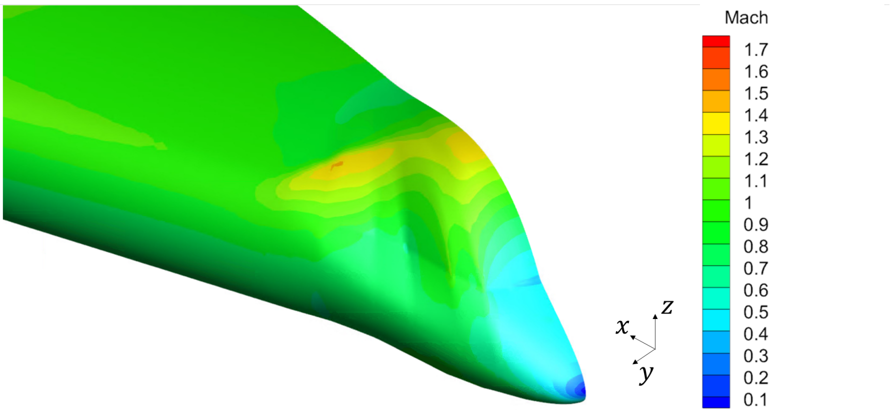

(b) Mach contours

Figure 5.11: Close up of the 3D aerodynamic results for the integrated cockpit design (M=0.85, h=13,000m, $C_{L_{\text{ref}}} = 0.266$)

Furthermore, the aerodynamic results shown in table 5.2 show that the integration of the cockpit increases the total drag coefficient of the aircraft slightly, and as a result decreases the lift over drag ratio by 0.80% as compared to the original geometry. The decrease in total lift to drag ratio is to be expected as the design features of the cockpit, such as the requirement for pilots to have a minimum view outside, are contrary to a pure aerodynamic design. For example, to make it possible for the pilots to see the runway at landing, the nose is swept down and a kink is introduced below the windshield. However, for providing a solution to the root effect it is necessary to sweep the nose up. Additionally, the lift distribution displayed in fig. 5.6a shows that the lift generated at the cockpit position is increased further from the symmetry plane, but is reduced at the root by 20%. This may deviate further from the elliptical lift distribution and as such increase the induced drag.

Finally, it must be noted that the viscous component of the drag coefficient is estimated using relatively simple methods, which do not account for the kink in the geometry. This may cause an error between the actual viscous drag and the predicted one. However, the proposed model is focused on providing a method to optimize the Flying V cockpit outer mold line. As such, it is sufficient to indicate a trend in the drag as opposed to providing a highly accurate solution. If the aerodynamic module can make a trend to occur an optimization method can find a better shape in a reliable way.

5.2.3. CASE III: CENTER FAIRING INTEGRATION

The final case includes a design for the center fairing. The design features a trailing edge movement downward and an extension in x-direction relative to the base geometry. The fairing attaches at 70% of the chord and runs for 5.7m where it runs aft parallel to the flight direction. The design, using the parameters as described in table F.4, can be seen in fig. 5.12.

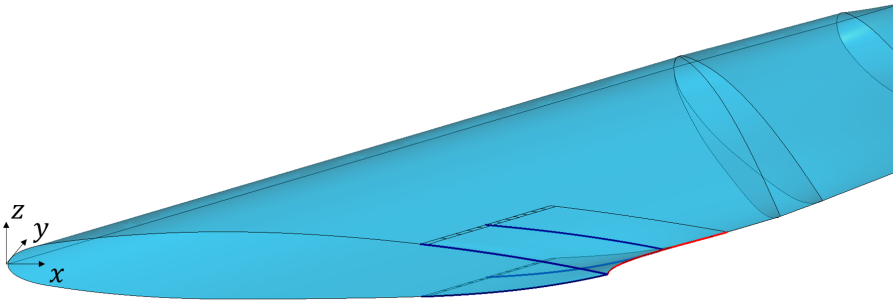

Figure 5.12: The center fairing design integrated in the original geometry used for the third case

AERODYNAMIC RESULTS

The pressure distribution along the root airfoil is shown in fig. 5.13, where it can be seen that the pressure coefficient starts oscillating after the start of the inserted fairing. This may be due to the presence of the transition surface, where the length of a mesh control edge is small and multiple are in close proximity to each other. Close inspection of the mesh does not reveal any anomalies. Again, it must be noted that the CFD solution has been converged. Also, doubling the width of the transition surface decreases the oscillations slightly. Furthermore, the pressure distribution shows that the pressure on the upper surface is lower till about 95% of the root chord. The pressure distribution on the bottom surface shows the same change. Furthermore, the pressure coefficient contours and Mach contours are shown in fig. 5.14. Here, not much seems to be changed relative to the figures of the original shown before. A large version of these figures can be seen in appendix G.

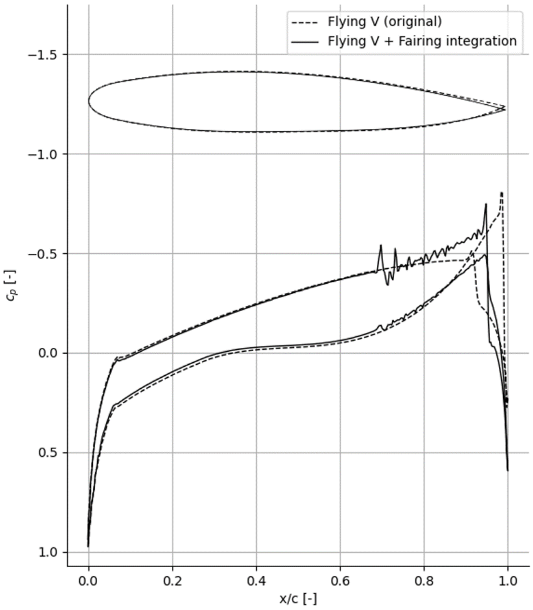

Figure 5.13: Pressure coefficient plot for the Flying V with integrated center fairing design (M=0.85, h=13,000m, $C_{L_{ref}}$ = 0.266)

Finally, the total lift over drag ratio of the aircraft shows an increase of 0.9% relative to the base geometry, as can be seen in table 5.2. This change is mainly due to the inviscid component of the drag coefficient, which is reduced by 1.17%. This is due to the increased lift from the center section, which can be seen in fig. 5.6a. The lift at the center is increased along the entire length of the added fairing, and brings the lift distribution closer to an elliptical one. Furthermore, the increased lift at the root causes the aircraft angle of attack to be decreased by 0.6 degrees, which in turn causes less lift to be generated by the outer wing, reducing the total inviscid drag. The effect of the decreased angle of attack can also be seen in fig. 5.6b in the lower drag coefficient that is present along the entire span.

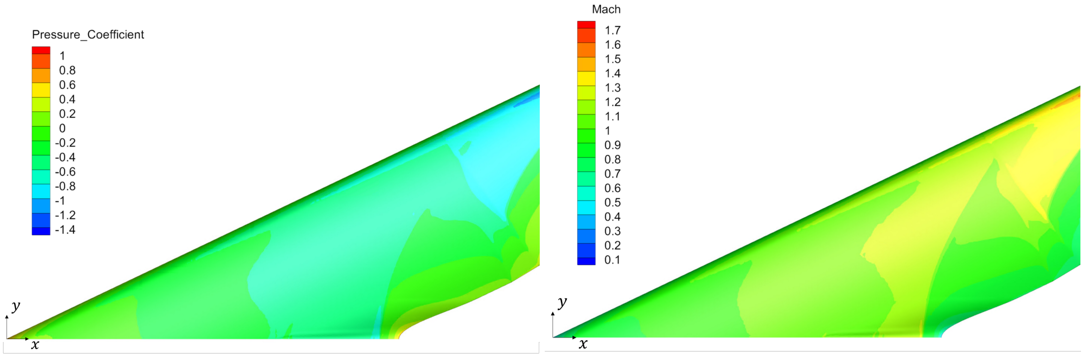

(a) Pressure coefficient contours

(b) Mach contours

Figure 5.14: Aerodynamic results for the Flying V with integrated center fairing

Table 5.2: Results of the aerodynamic analyses for multiple cases. Percentages are relative to the original case (*The original geometry is the representation of that made by Faggiano in the parameterisation by Hillen [8])

	C_L [-]		$C_{D_{visc}}$ [counts]		$C_{D_{invisc}}$ [counts]		C_D [counts]		$\frac{C_L}{C_D}$ [-]	
Flying V (original)	0.264	-	47.7	-	65.2	-	112.9	-	23.37	-
Flying V (original) with reattached nose and center fairing	0.264	0.00%	47.7	0.00%	65.2	0.00%	113.0	0.06%	23.37	0.00%
Case I: Root effect	0.265	3.85%	48.3	1.26%	64.8	-0.61%	113.1	0.18%	23.46	0.39%
Case II: Cockpit integration	0.264	0.00%	47.9	0.42%	66.1	1.38%	114.0	0.97%	23.19	-0.77%
Case III: Fairing integration	0.265	3.85%	47.8	0.21%	64.5	-1.07%	112.3	-0.53%	23.59	0.94%

6

CONCLUSION AND RECOMMENDATIONS

The research objective of the work presented in this thesis is to develop a parameterisation for the Flying V to integrate a cockpit and aft center fairing design, that satisfies the constraints imposed by pilot anthropometry, visibility certification constraints, allocation of nose landing gear and radar, while ensuring a high probability for good aerodynamic performance and being able to be used in an aerodynamic design optimization. This was done by developing an application in the Parapy suite using the Python programming language. The generated geometry was meshed and analysed using an Euler method in the Stanford University Unstructured software, providing the inviscid drag of the aircraft. This was added to the result of a semi-empirical method, which was used to estimate the viscous drag.

The results of the research consisted of an analysis of the parameterisation and the constraints imposed on the model. This was done through determining the robustness and a qualitative evaluation of the design space, as well as an aerodynamic analysis for a selected number of cases.

6.1. CONCLUSION

The cockpit and aft center fairing parameterisation provide an outer mold line that fits the rest of the Flying V shape. This was done by aligning multiple cross-sections along a predefined rail curve, after which a loft was made using these cross-sections. The loft replaced the original geometry and assured that a smooth symmetric geometry took its place.

The flight deck was integrated in the geometric model by using multiple constraints. The first constraint was the visibility certification constraint, which put a requirement on the minimum field of view of the pilots from the design eye point. The minimum field of view is complemented by a required overnose angle during landing, which was determined to be 31.5° between ±10° port and starboard. Following was the constraint formed by pilot anthropometry. This was used to determine whether the pilot could fit in the cockpit and how much room had to be reserved. This was assessed using the 5th and 99th percentile human models and the typical sizes of pilot seats. The pilot size also defined the position of the cockpit floor and subsequently the positioning of the radar and nose landing gear. The final constraints were defined by providing enough space between the pilots and the windshield, and by ensuring that the windshield is angled above an angle of 35 ° relative to the pilot's vision. This was done in order to prevent a loss of the transparent qualities of the windshield from the pilot's perspective.

After the parameterisation and the constraints that apply to it were known, an analysis was performed for three cases. The first case served a pure aerodynamic purpose, of which the geometry was defined using measures to reduce the root effect. It was seen that the measures increased the lift at the root of the wing. However, the pressure distribution on the root airfoil showed that a relatively high pressure area was located on the top surface. This was due to the low amount of curvature in that area, so more careful adaptation of the geometry could yield better results. Furthermore, the aircraft lift to drag ratio relative to the base geometry was found to be increased by 0.39%, due to the increased lift at the root.

The second case provided a potential cockpit design. In the aerodynamic results of this case it could be seen that a high pressure area was present at the windshield kink. This pressure peak was also seen in the pressure distribution, after which a large negative spike was observed. This was due to the high velocity on top of the cockpit, resulting in a low pressure coefficient. These results caused a decrease in lift at the root.

Because of these factors, the lift to drag ratio of the aircraft was found to be decreased by 0.8%. Furthermore, all defined constraints were satisfied for the cockpit design and a larger-than-necessary windshield was defined. The windshield surface area resulted to be 2.36 m^2, which was found to be comparable to that used on the A320 and A350-900.

The third and final case included only the aft center fairing design of the first case. This design resulted in a lift to drag ratio of 23.59. This is an increase of 0.94%, which was the highest of all cases. It was a result of a large increase in lift at the root, causing the angle of attack of the aircraft to decrease by 0.6 degrees. The lift distribution was seen to be more elliptical, and the inviscid drag distribution showed an overall decrease at the outer wing because of the reduced angle of attack.

Finally the robustness of the geometrical model was assessed. This was calculated by dividing the number of valid and generated geometries by the amount of samples taken. The analysis was performed separately for the cockpit and for the aft center fairing, and resulted in an average robustness of 20.3% for the cockpit model where a more precise geometry is used. When a setting was used to generate a less accurate geometrical model, the robustness was found to be 50.4% on average. Lastly, the robustness for the aft center fairing was determined to be 39.9% on average. Overall, the robustness of these models is rather low. However, the less accurate cockpit geometry is much more robust than the more accurate geometry, making it more useful for an initial search in an optimization routine, while the more accurate model can take over when a region is found where the optimum can reside.

6.2. RECOMMENDATIONS

This research has provided a first stride in the design of a cockpit design for the Flying V in combination with the center fairing. However, in order to advance the model, some steps must be taken and improvements can be made. The first step is to optimize the model provided in this research. This can be done with and without the applicable constraints to determine how much influence these really have on the optimum lift over drag ratio and the resulting geometry. Besides carrying out an optimization, improvements that can be made on the model are:

- The cockpit cross-section can be altered. Especially the top aft curve can be split in two in order to provide more design freedom, and make it easier to provide enough room for the pilot and also being able to reduce the maximum Mach number over the bulge of the cockpit. Also, the curves are now continuous to the first order. It is probably beneficial to have the cross-section attach to the main wing geometry to at least the second order continuous for improved aerodynamic results.

- Some parts of the cockpit interior can already be placed. For example, the pilot chair, the floor, nose landing gear and the radar are shown to be placed using the method discussed in this research. However, the rest of the interior of the cockpit can be designed as well. For example, the instrument panel and controls can be designed, and the topic of human-machine interaction can be investigated.

- The kink at the bottom of the windshield was seen to generate a large positive pressure coefficient. This sudden change can trigger turbulence which in its turn creates noise. Noise analysis and optimization of the cockpit would be needed after a cockpit has been optimized. This sort of analysis might give great insight in how to best design a windshield and cockpit exterior.

- Currently, it was impossible to have all the cockpit cross-sections align in a single point, mainly due to the meshing software being unable to generate a grid for such a geometry. A different meshing software could help in generating a grid for this type of geometry or improve the grid of the current geometrical model.

- A more advanced CFD analysis can be performed to investigate what the exact influence is of the cockpit and center fairing integration. Currently the drag is partially estimated using semi-empirical methods, which introduce inaccuracies. It would be interesting to determine how large the error between the two is.

A

APPENDIX A: UML CLASS DIAGRAM

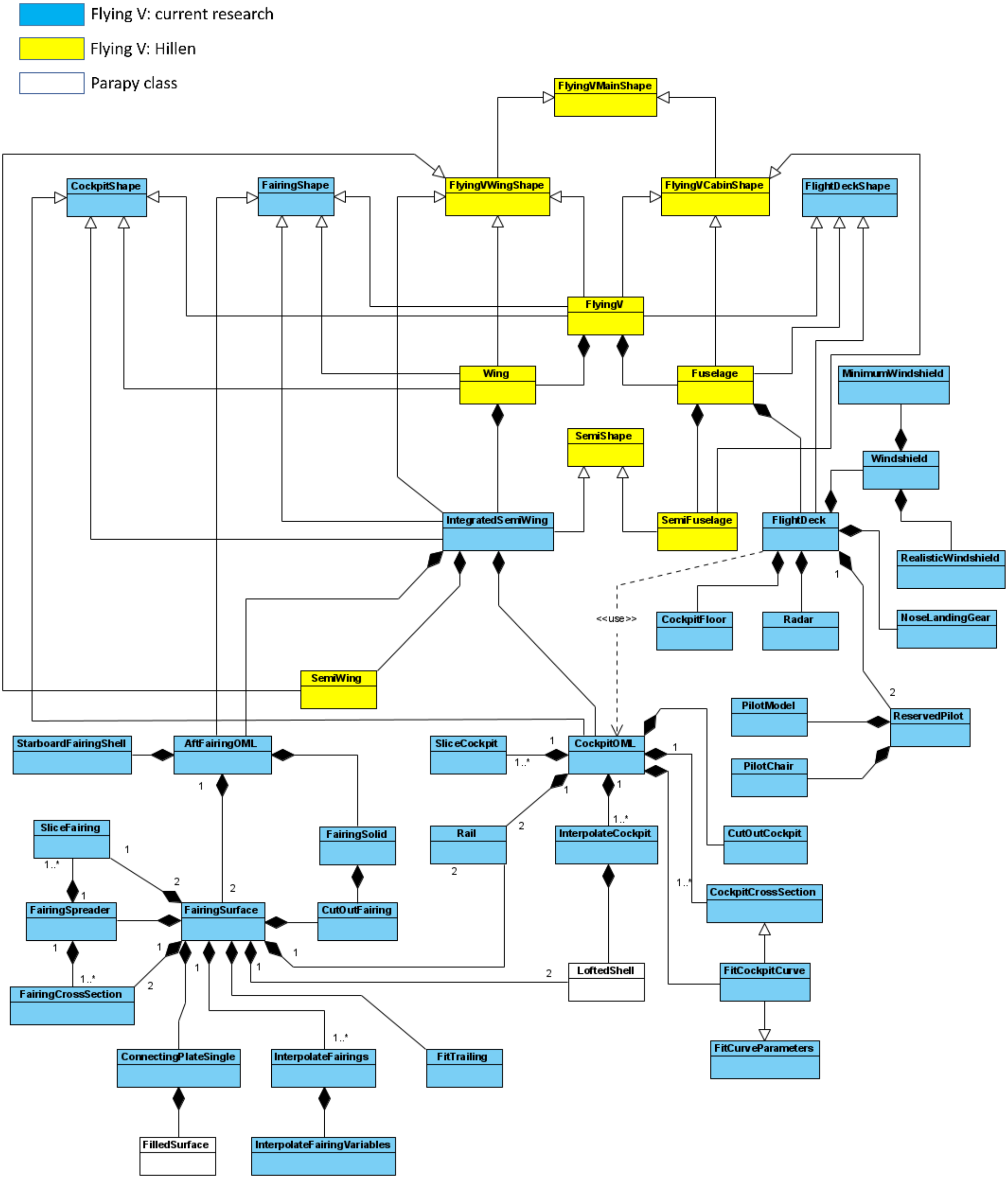
Flying V: current research
Flying V: Hillen
Parapy class
FlyingVMainShape
CockpitShape
FairingShape
FlyingVWingShape
FlyingVCabinShape
FlightDeckShape
FlyingV
Wing
Fuselage
MinimumWindshield
SemiShape
Windshield
IntegratedSemiWing
SemiFuselage
FlightDeck
RealisticWindshield
<<use>>
CockpitFloor
Radar
NoseLandingGear
SemiWing
PilotModel
ReservedPilot
PilotChair
StarboardFairingShell
AftFairingOML
SliceCockpit
CockpitOML
SliceFairing
FairingSolid
Rail
InterpolateCockpit
CutOutCockpit
FairingSpreader
FairingSurface
CutOutFairing
CockpitCrossSection
FairingCrossSection
LoftedShell
FitCockpitCurve
ConnectingPlateSingle
InterpolateFairings
FitTrailing
FitCurveParameters
FilledSurface
InterpolateFairingVariables
1
2
1..*

B

APPENDIX B: ROBUSTNESS DESIGN SPACE BOUNDS

Table B.1: Design space bounds for parameters used to determine the robustness of the cockpit outer mold line

parameters	symbol	unit	lower bound	upper bound
nose x-location	x_{nose}	[m]	0	4
cockpit end location	x_{cockpit}	[m]	5	9
aft tolerance	δ_{cockpit}	[m]	0.25	0.75
rail z-displacement	R_{cockpit}	[-]	-1.5	1.5
rail free parameter	$a_{\text{rail,cockpit}}$	[-]	-0.5	0.2
horizontal window position	$\bar{l}_{\text{window}}$	[-]	0.1	0.5
vertical window position	$\bar{h}_{\text{window}}$	[-]	0.2	0.75
view angle	ϕ_{window}	[°]	20	80
free variable aft top curve	$p_{\text{top,aft}}$	[-]	0	0.5
free variable front top curve	$p_{\text{top,front}}$	[-]	0	2
free variable bottom curve	p_{bottom}	[-]	0	0.2

Table B.2: Design space bounds for parameters used to determine the robustness of the center fairing outer mold line

parameters	symbol	unit	lower bound	upper bound
start location top	$x_{\text{fairing,top}}$	[-]	0.5	0.95
start location bottom	$x_{\text{fairing,bottom}}$	[-]	0.5	0.95
aft displacement	$\Delta x_{\text{fairing}}$	[m]	0	7
spanwise start location	b_{fairing}	[m]	0.5	7
end angle	Φ_{end}	[°]	0	65
rail z-displacement	R_{fairing}	[m]	0	2
rail free parameter	$a_{\text{rail,fairing}}$	[-]	-0.5	0.5
free variable top curve	$a_{\text{fairing,top}}$	[-]	-0.01	0
free variable bottom curve	$a_{\text{fairing,bottom}}$	[-]	0	0.01
cross-section location	f_{fairing}	[-]	0.15	0.85

C

Appendix C: Anthropometric Data

Table C.1: Anthropometric data from the Human Factors Design Guide [24]

gender	M					F				
percentile	1	5	50	95	99	1	5	50	95	99
standing height	160.3	164.7	175.5	186.7	190.9	148.3	152.8	162.7	173.7	178
eye height, sitting	71.2	73.5	79.2	84.8	86.9	66.4	68.5	73.8	79.4	81.6
upper leg length	-	-	-	-	-	-	-	-	-	-
upper leg thickness	14.1	14.9	16.8	19	20.1	13.4	14	15.75	18	19
lower leg length	49.7	51.4	55.8	60.6	62.3	45.4	47.4	49.8	56	57.8
lower leg thickness	-	-	-	-	-	-	-	-	-	-
foot length	-	-	-	-	-	-	-	-	-	-
foot width	-	-	-	-	-	-	-	-	-	-
torso height	56.3	58.3	63	67.7	69.4	52.3	53.9	58.4	63.1	64.7
torso width	-	-	-	-	-	-	-	-	-	-
torso thickness	-	-	-	-	-	-	-	-	-	-
shoulder width	43.4	45	49.1	53.5	55.2	38	39.7	43.1	47.2	49.2
upper arm length		-	-	-	-	-	-	-	-	-
upper arm thickness	-	-	-	-	-	-	-	-	-	-
lower arm length	43.4	44.8	48.3	52.4	54.2	39.1	40.6	44.2	48.3	49.8
lower arm thickness	-	-	-	-	-	-	-	-	-	-
head height	21.2	21.8	23.2	24.7	25.5	19.8	20.4	21.8	23.2	23.8
head width	13.1	13.5	14.5	15.5	15.9	12.5	12.8	13.3	14.3	15
head length	18	18.5	19.7	20.9	20.9	17.2	17.6	18.7	19.8	20.2

Table C.2: Anthropometric data from Man-System Integration Standards [25]

gender	M			F		
percentage	5	50	95	5	50	95
standing height	169.7	179.9	190.1	148.9	157	165.1
eye height, sitting	76.8	81.9	86.9	68.1	73.8	79.5
upper leg length	56.8	61.3	65.8	48.9	53.3	57.8
upper leg thickness	14.5	16.8	19.1	11.2	12.9	14.5
lower leg length	52.6	56.7	60.9	41.6	45.6	49.5
lower leg thickness	10.8	12	13.2	9.8	10.9	12
foot length	25.4	27.3	29.3	21.3	22.9	24.4
foot width	9	9.9	10.7	8.6	9.3	10
torso height	60.8	65.4	70	-	-	-
torso width	32.9	39.2	45.4	32.4	35.7	39
torso thickness	21.8	25	28.2	17.4	20.5	23.6
shoulder width	48.8	55.1	61.5	-	-	-
upper arm length	33.7	36.6	39.4	27.2	29.8	32.4
upper arm thickness	9.4	10.6	11.7	6.9	8.1	9.3
lower arm length	-	-	-	37.3	41.7	44.6
lower arm thickness	8.7	9.6	10.4	6.3	7	7.7
head height	31.7	32.3	32.8	29.3	29.9	30.6
head width	14.8	15.7	16.5	14.4	15.6	16.8
head length	18.8	20	21.1	16.7	18.2	19.6

D

APPENDIX D: MESH CONVERGENCE SETTINGS AND RESULTS

Table D.1: Mesh control values used for the mesh convergence together with the results these have produced. The error is defined as the drag coefficient of a mesh divided by the drag coefficient of the finest mesh

Variable							
Factor (larger is finer)	0.50	0.60	0.67	0.88	1	1.05	1.20
nodes per length	7.5	9	10.05	13.13	15	15.75	18
max size wing	0.20	0.17	0.15	0.11	0.10	0.10	0.08
outer domain maxim	30	25	22.39	17.14	15	14.29	12.5
triangular growth rate	0.20	0.17	0.15	0.11	0.10	0.10	0.08
tetrahedral max size	30	25	22.39	17.14	15	14.29	12.5
tetrahedral growth rate	0.60	0.50	0.45	0.34	0.30	0.29	0.25
amount of volumes	349,144	508,002	733,638	1,205,188	1,704,123	2,694,471	4,303,046
$C_{D_{inv}}$ [counts]	37.32	37.26	34.73	33.47	32.69	32.78	32.74
error	-14.0%	-13.8%	-6.1%	-2.2%	0.2%	-0.1%	0.0%

E

APPENDIX E: DESIGN SPACE IMPRESSION

This appendix is dedicated to providing an impression of the design space. This is done by means of 100 randomized designs for each the cockpit and center fairing..

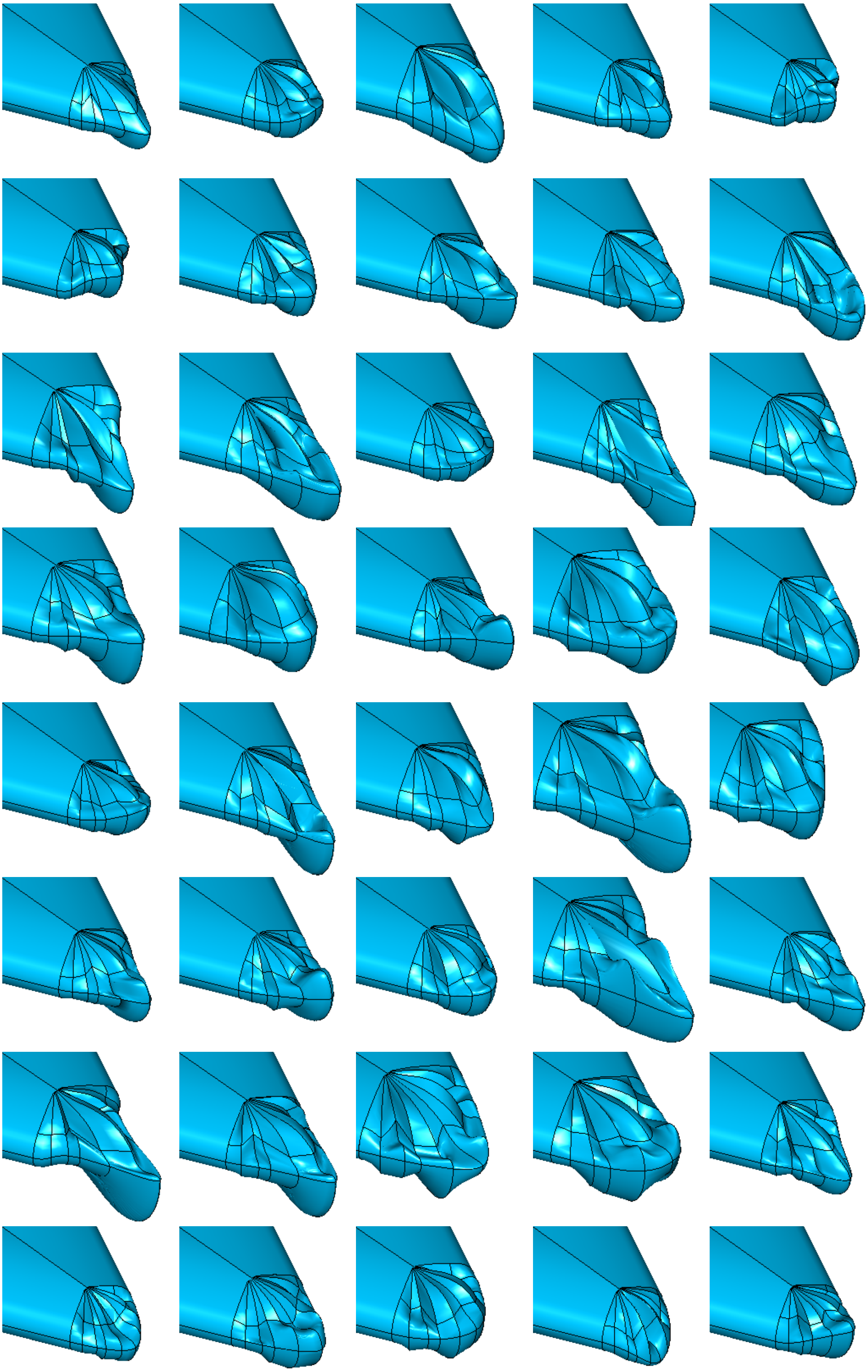

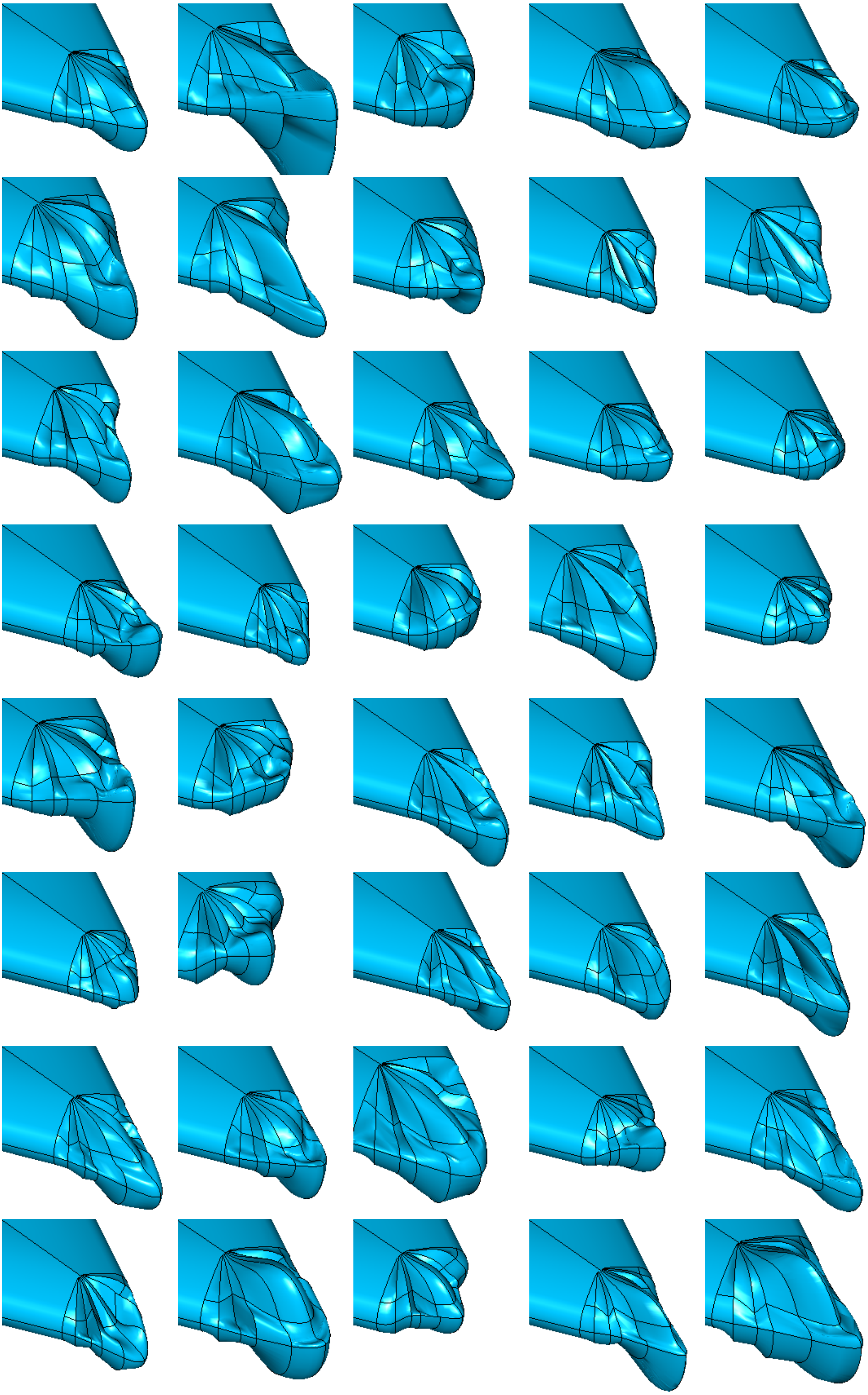

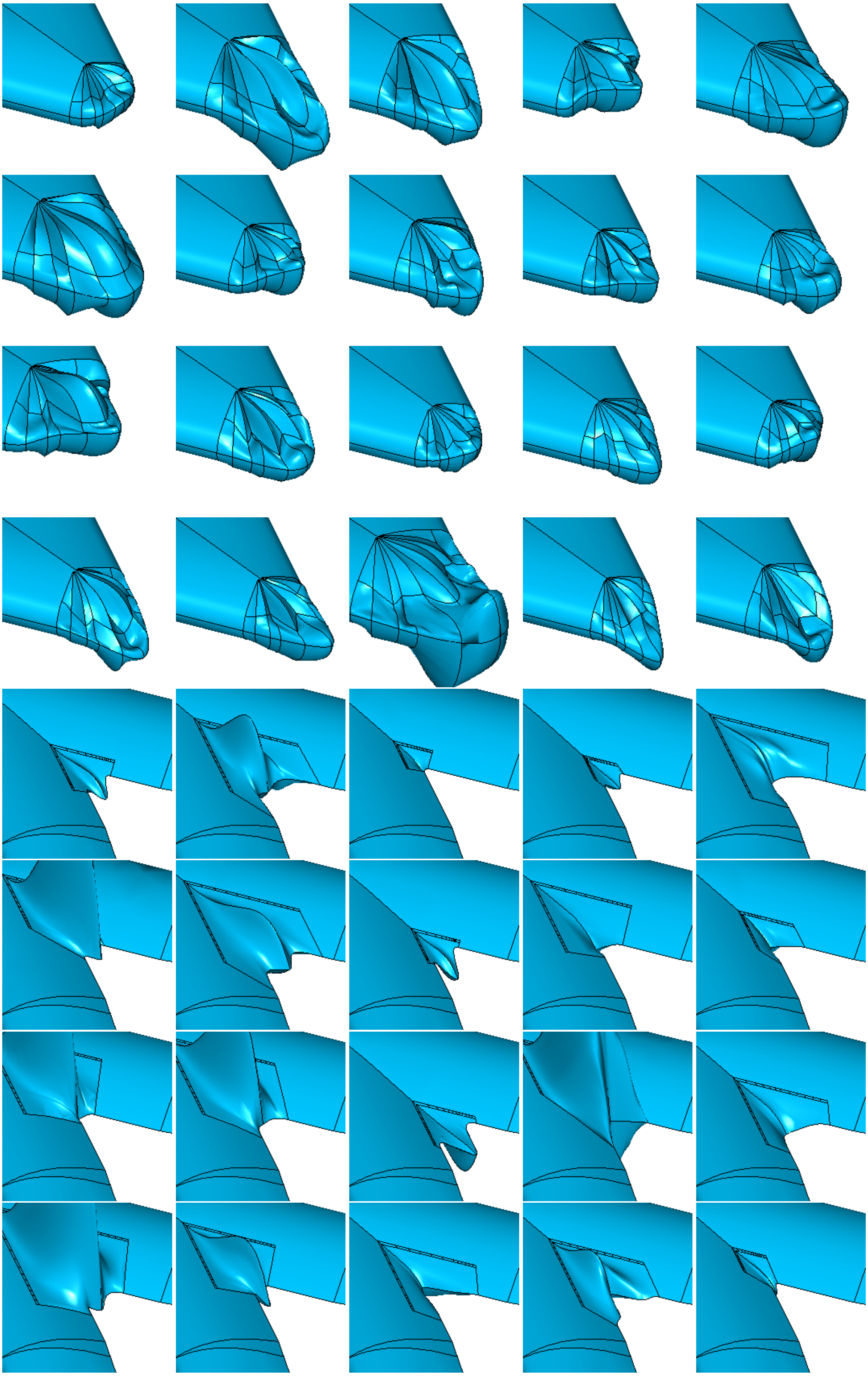

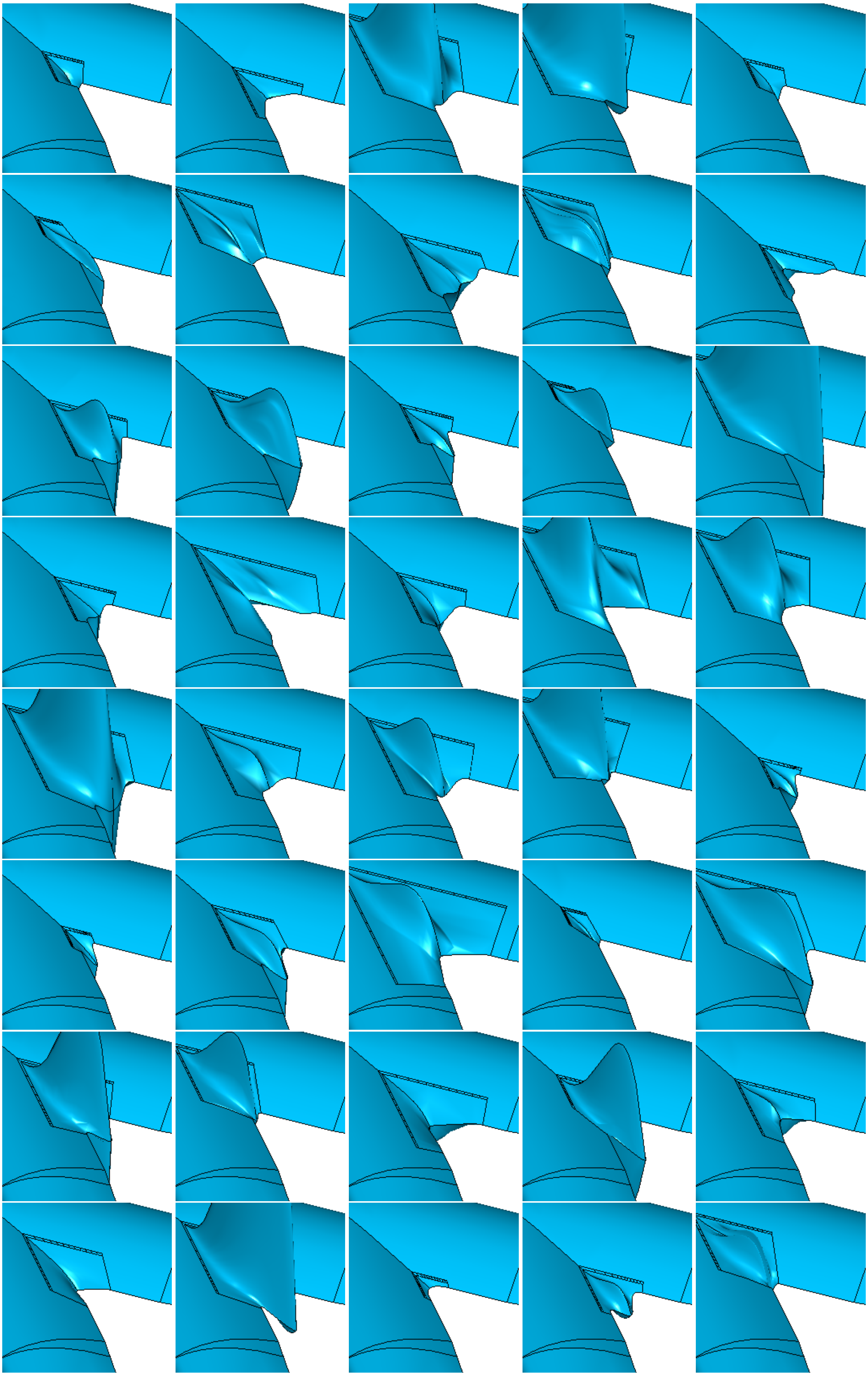

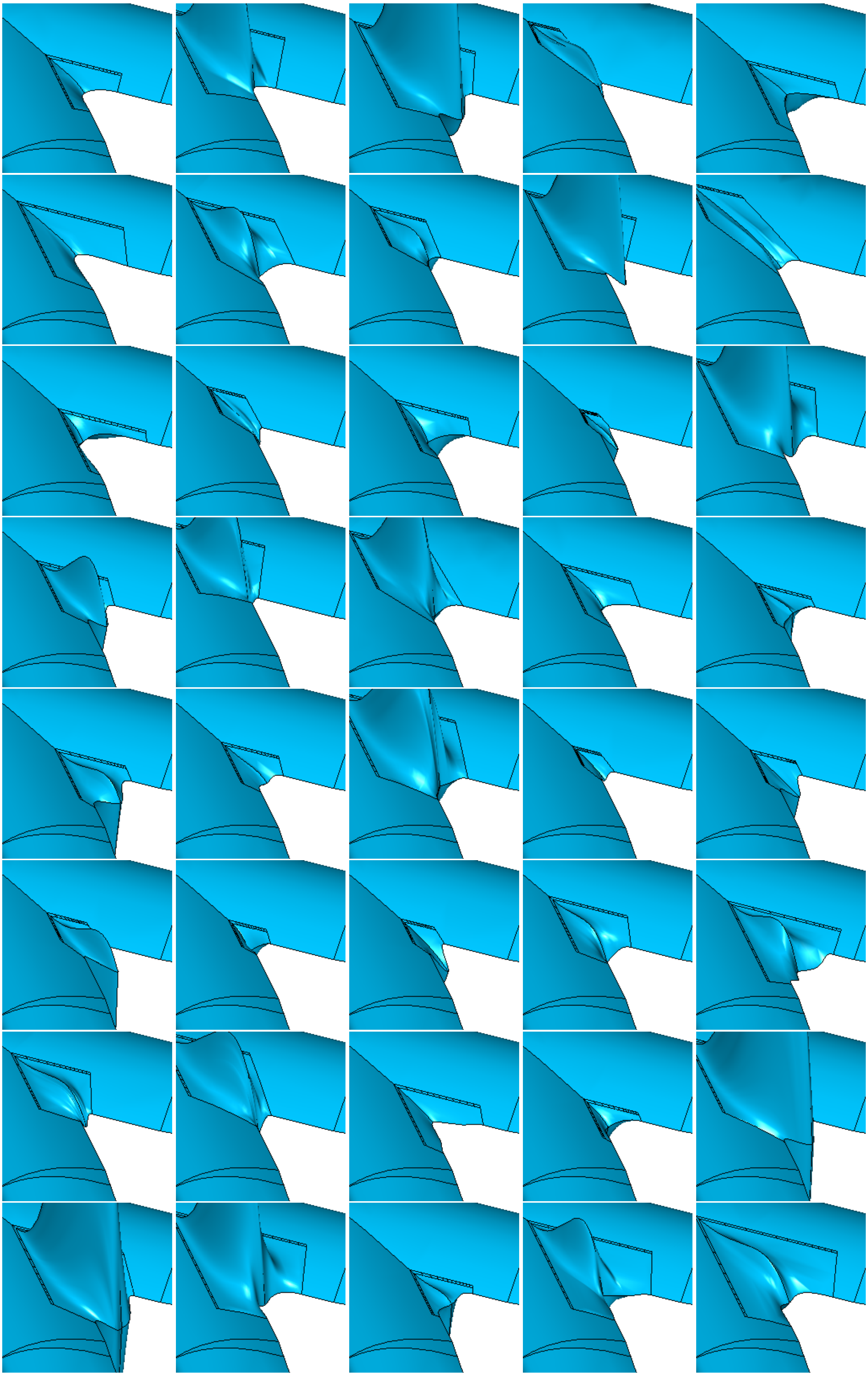

F

APPENDIX F: CASE INPUT DATA

F.1. CASE I: ROOT EFFECT

Table F.1: Cockpit parameters for the Flying V with adaptations made to reduce the root effect (first case of the results chapter)

parameter	symbol	value	unit
nose x-location	x_{nose}	1.95	[m]
cockpit end location	x_{cockpit}	13	[m]
aft tolerance	δ_{cockpit}	0.5	[m]
rail z-displacement	R_{cockpit}	-1.6	[m]
rail free parameter	$a_{\text{rail,cockpit}}$	-0.01	[-]
horizontal window position	l_{window}	0.35	[-]
vertical window position	h_{window}	-3	[-]
view angle	ϕ_{window}	-5.0	[°]
free variable aft top curve	$p_{\text{top,aft}}$	0.005	[-]
free variable front top curve	$p_{\text{top,front}}$	0.0	[-]
free variable bottom curve	p_{bottom}	0.0025	[-]
cross-section location	f_{cockpit}	0.0	[-]

Table F.2: Fairing parameters for Flying V with adaptations made to reduce the root effect (first case of the results chapter)

parameter	symbol	value	unit
start location top	$x_{\text{fairing,top}}$	0.6	[-]
start location bottom	$x_{\text{fairing,bottom}}$	0.6	[-]
aft displacement	$\Delta x_{\text{fairing}}$	0.4	[m]
spanwise start location	b_{fairing}	5.7	[m]
end angle	Φ_{end}	64.5	[°]
rail z-displacement	R_{fairing}	0.05	[m]
rail free parameter	$a_{\text{rail,fairing}}$	0.0	[-]
free variable top curve	$p_{\text{fairing,top}}$	[0,0]	[-]
free variable bottom curve	$p_{\text{fairing,bottom}}$	[0,0]	[-]
cross-section location	f_{fairing}	0.5	[-]

F.2. CASE II: COCKPIT INTEGRATION

Table F.3: Cockpit parameters for the Flying V using the integrated cockpit (second case of the results chapter)

parameter	symbol	value	unit
nose x-location	x_{nose}	1.5	[m]
cockpit end location	x_{cockpit}	6.7	[m]
aft tolerance	δ_{cockpit}	0.5	[m]
rail z-displacement	R_{cockpit}	1.0	[m]
rail free parameter	$a_{\text{rail,cockpit}}$	0.0	[-]
horizontal window position	$\bar{l}_{\text{window}}$	0.23, 0.19, 0.13, 0.135, 0.2, 0.19, 0.12	[-]
vertical window position	$\bar{h}_{\text{window}}$	0.5, 0.475, 0.45, 0.46, 0.45, 0.45, 0.45	[-]
view angle	ϕ_{window}	40.0, 40.0, 40.0, 45.0, 40.0, 40.0, 40.0	[°]
free variable aft top curve	$p_{\text{top,aft}}$	0.0, 0.0, 0.2, 0.1, 0.1, 0.1, 0.1	[-]
free variable front top curve	$p_{\text{top,front}}$	0.25, 0.2, 0.1, 0.1, 0.15, 0.1, 0.02	[-]
free variable bottom curve	p_{bottom}	0.001, 0.002, 0.005, 0.0085, 0.01, 0.01, 0.02	[-]
cross-section location	f_{cockpit}	0.0, 0.1, 0.175, 0.25, 0.375, 0.5, 0.75	[-]

F.3. CASE III: FAIRING INTEGRATION

Table F.4: Parameters used to describe the center fairing for the Flying V using the integrated center fairing (third case of the results chapter)

parameter	symbol	value	unit
start location top	$x_{\text{fairing,top}}$	0.7	[-]
start location bottom	$x_{\text{fairing,bottom}}$	0.7	[-]
aft displacement	$\Delta x_{\text{fairing}}$	0.4	[m]
spanwise start location	b_{fairing}	5.7	[m]
end angle	Φ_{end}	0.0	[°]
rail z-displacement	R_{fairing}	0.2	[m]
rail free parameter	$a_{\text{rail,fairing}}$	0.0	[-]
free variable top curve	$p_{\text{fairing,top}}$	[0,0]	[-]
free variable bottom curve	$p_{\text{fairing,bottom}}$	[0,0]	[-]
cross-section location	f_{fairing}	0.5	[-]

G

APPENDIX G: LARGE CONTOUR PLOTS

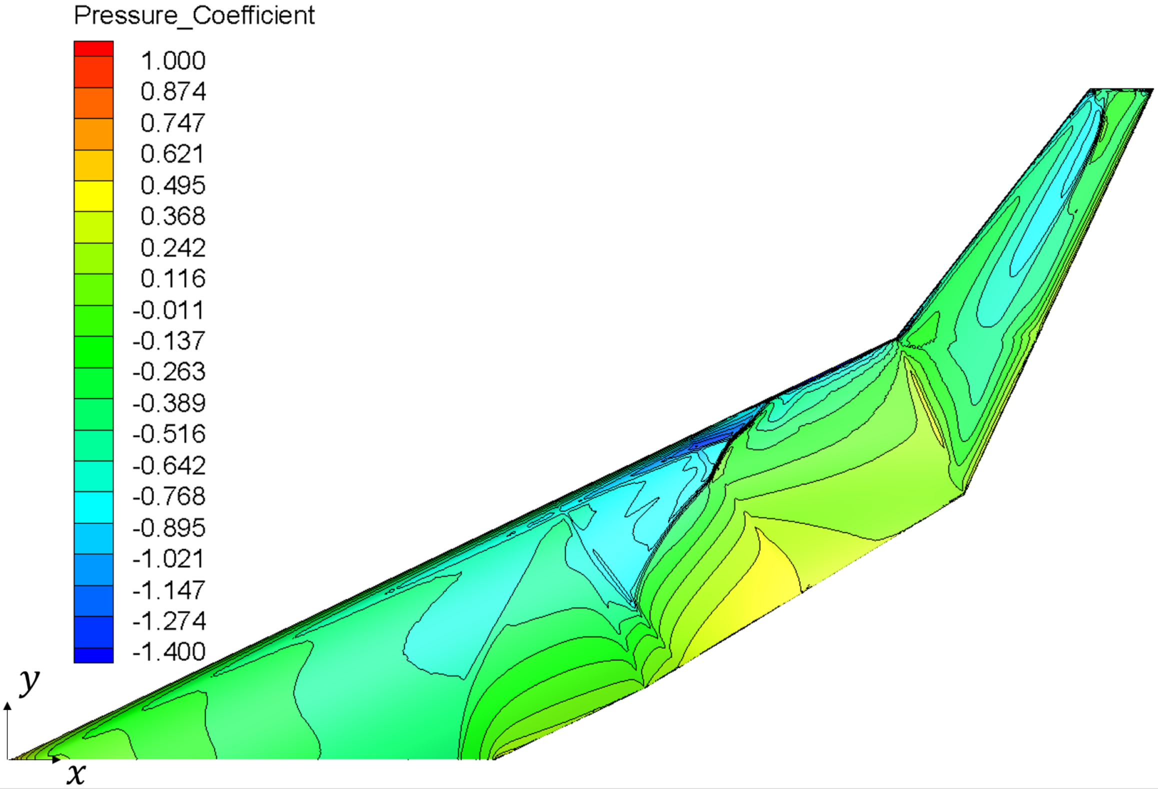

Figure G.1: Isobars for the original geometry (M=0.85, h=13,000m, $c_{L_{\mathrm{ref}}} = 0.266$)

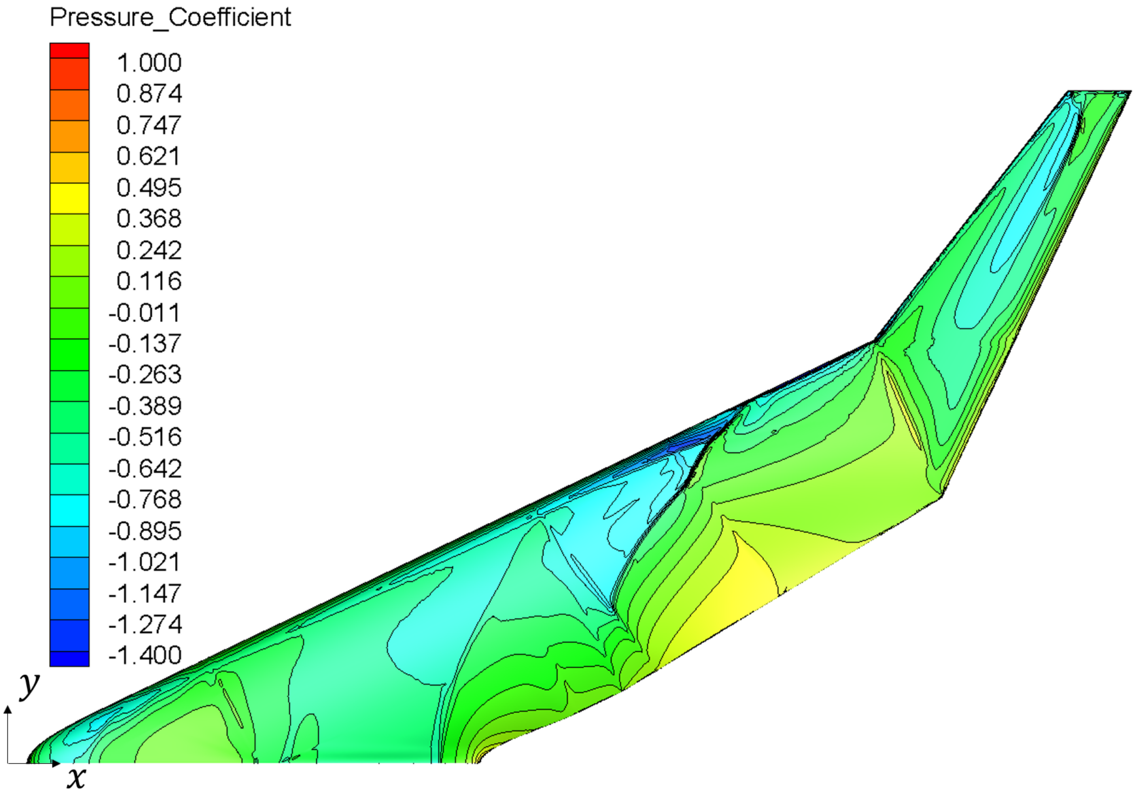

Figure G.2: Isobars for the first case geometry, using an adapted airfoil to satisfy the airfoil changes required to reduce the root effect (M=0.85, h=13,000m, $c_{L_{\text{ref}}} = 0.266$)

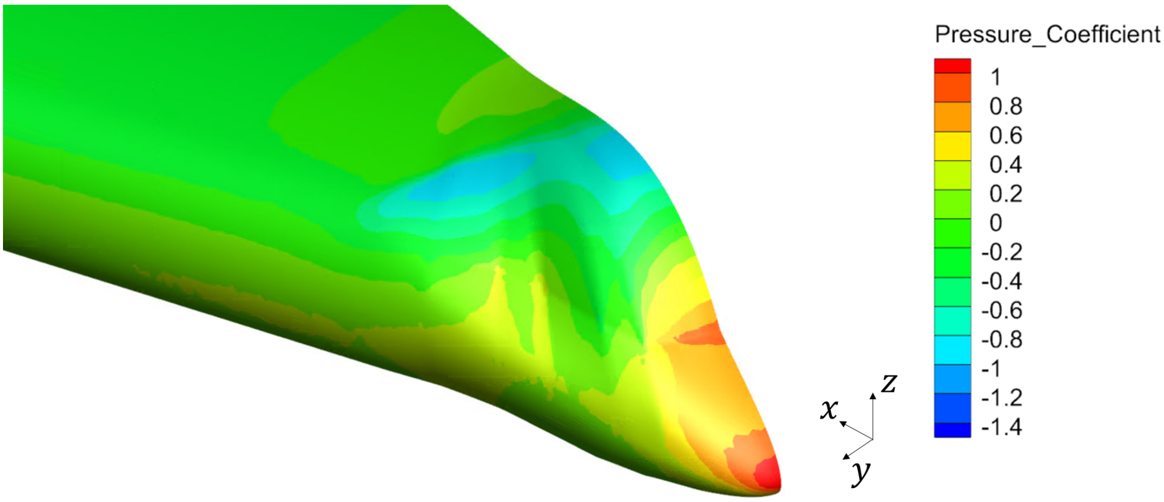

Figure G.3: Close up of the pressure contours for the integrated cockpit design (M=0.85, h=13,000m, $c_{L_{\text{ref}}} = 0.266$)

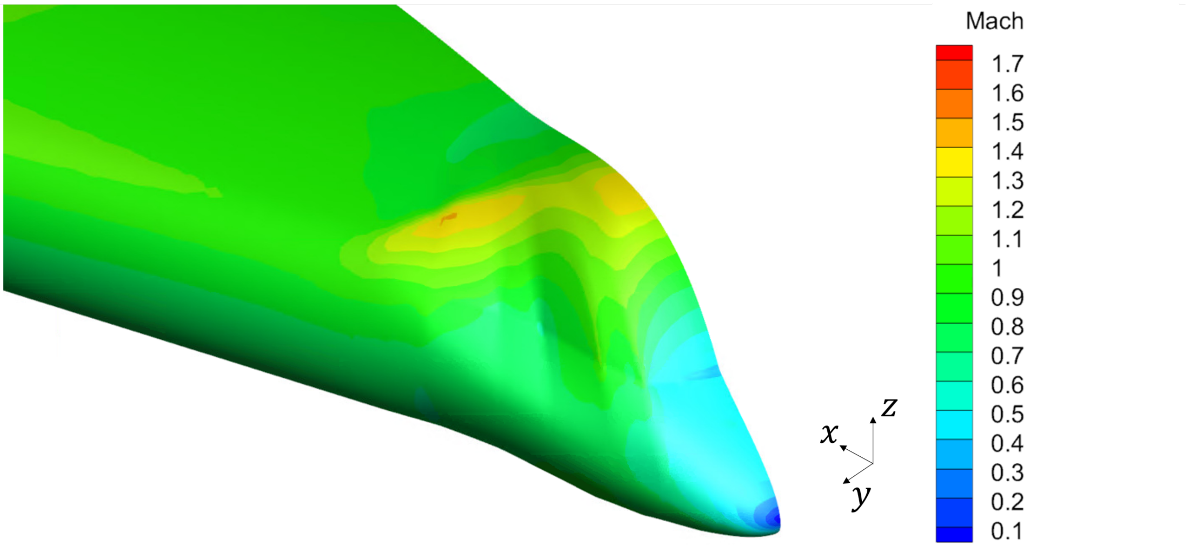

Figure G.4: Close up of the Mach contours for the integrated cockpit design (M=0.85, h=13,000m, $c_{L_{\text{ref}}} = 0.266$)

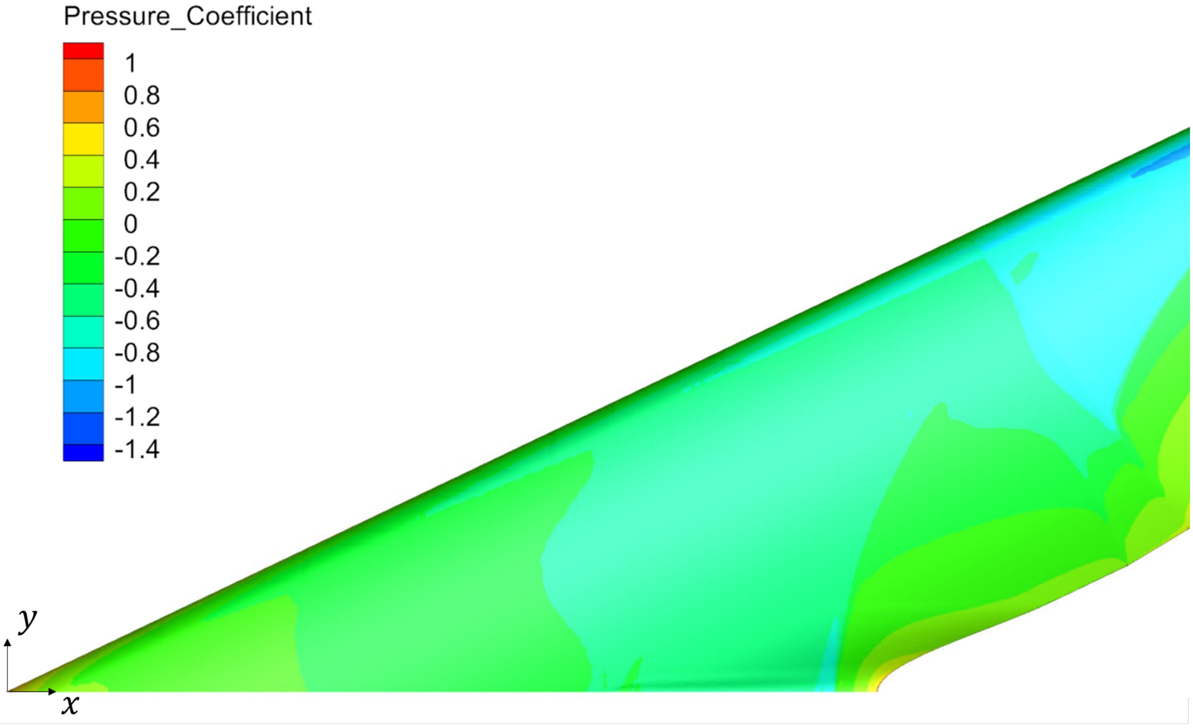

Figure G.5: Aerodynamic results for the Flying V with integrated center fairing (M=0.85, h=13,000m, $C_{L_{\text{ref}}} = 0.266$)

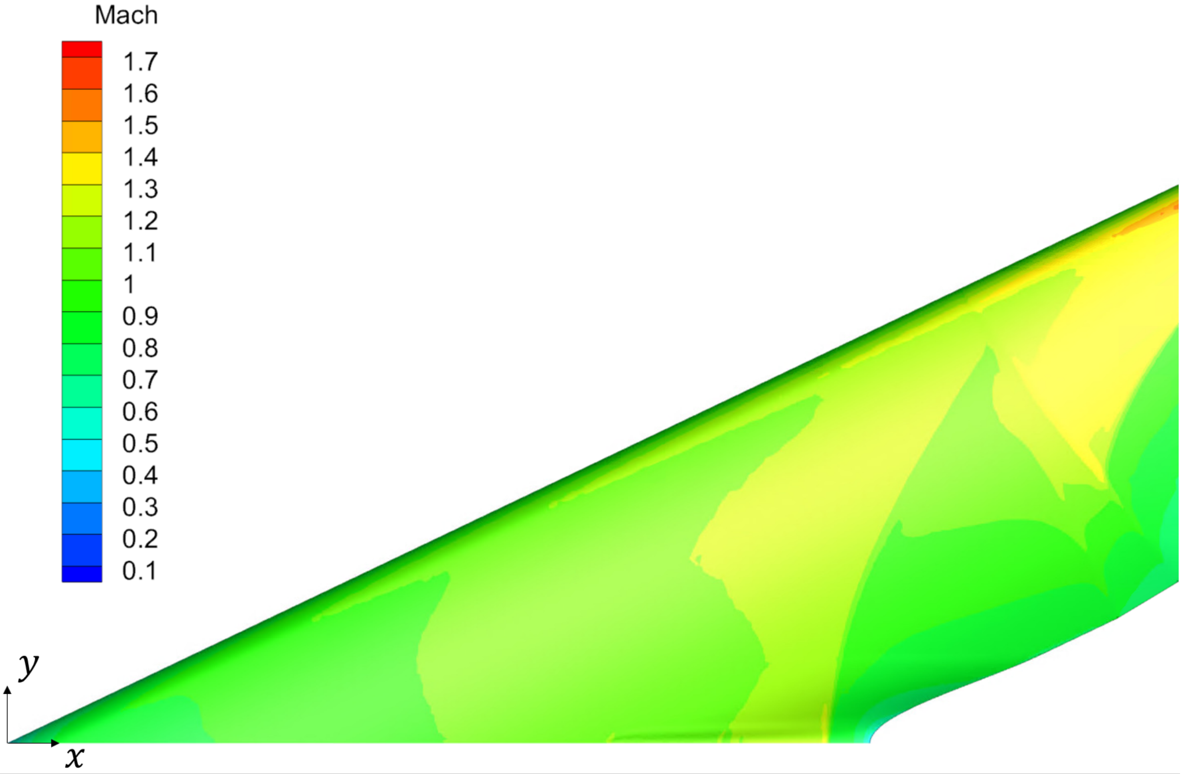

Figure G.6: Aerodynamic results for the Flying V with integrated center fairing (M=0.85, h=13,000m, $C_{L_{\text{ref}}} = 0.266$)

BIBLIOGRAPHY

[1] J. Benad, *Deutscher Luft- und Raumfahrtkongress* pp. 1-8 (2015), ISSN 01406736, URL http://www.dglr.de/publikationen/2015/370094.pdf.

[2] B. Rubio Pascual, *Engine-Airframe Integration for the Flying-V* (2018), URL https://repository.tudelft.nl/islandora/object/uuid%3A75be27a7-6fd4-4112-a600-45df2999758f

[3] F. Faggiano, *Aerodynamic Design Optimization of a Flying V Aircraft* (2016), URL http://resolver.tudelft.nl/uuid:43bbc423-3746-465d-b096-597f173be38d.

[4] L. van der Schaft, *Development, Model Generation and Analysis of a Flying V Structure Concept*, Delft University of Technology (2017), URL http://resolver.tudelft.nl/uuid:d9c9c02f-d67a-4e3c-93a7-eb20ed67cd03

[5] M. Claeys, *Flying V and Reference Aircraft Structural Analysis and Mass Comparison* (2018), URL https://repository.tudelft.nl/islandora/object/uuid%3Aee7f2ecb-cdb6-46de-8b57-d55b89f8c7e6

[6] R. Viet, Analysis of the flight characteristics of a highly swept cranked flying wing by means of an experimental test (2019), URL https://repository.tudelft.nl/islandora/object/uuid:90de4d9e-70ae-4efc-bd0a-7426a0a669c3?collection=education

[7] M. Palermo, *The Longitudinal Static Stability and Control Characteristics of a Flying V Scaled Model* (2019), URL https://repository.tudelft.nl/islandora/object/uuid%3A6286f9e2-c24a-430c-a4fa-9fb67b9558b4?collection=education.

[8] M. Hillen. *Parametrisation of the Flying-V Outer Mould Line.* (2020), URL http://resolver.tudelft.nl/uuid:f4863ae4-2792-4335-b929-ff9dfdb6fed5.

[9] B. M. Yutko, N. Titchener, C. Courtin, M. Lieu, L. Wirsing, J. Tylko, J. T. Chambers, T. W. Roberts and C. S. Church. *Conceptual Design of a D8 Commercial Aircraft.* 17th AIAA Aviation Technology, Integration, and Operations Conference. AIAA 2017-3590. June 2017. https://doi.org/10.2514/6.2017-3590

[10] L. Daumas, Q. Dinh, S. Kleinveld and G. Rogé. *Fuselage Shape Automatic Optimization with Geometric Constraints Using a CAD Based Process.* 11th AIAA/ISSMO Multidisciplinary Analysis and Optimization Conference. AIAA 2006-6936. September 2006. https://doi.org/10.2514/6.2006-6936

[11] M. Mestriner, R. F. de Souza and M. Ferrari.*Aerodynamic sensitivity to geometry parameters of an aircraft forward fuselage.* 2018 Applied Aerodynamics Conference. AIAA 2018-4201. June 2018. https://doi.org/10.2514/6.2018-4201

[12] F. Nicolosi, P. D. Vecchia, D. Ciliberti, V. Cusati and L. Attanasio *Fuselage Aerodynamic Prediction Methods.* 33rd AIAA Applied Aerodynamics Conference. AIAA 2015-2257. June 2015. https://doi.org/10.2514/6.2015-2257

[13] D. Kuchemann and J. Weber. *The subsonic flow past swept wings at zero lift without and with body.* 2908, 1953

[14] G.G. Brebner. *The application of camber and twist to swept wings in incompressible flow.* 171, 1952.

[15] Federal Aviation Authority. *Certification Specifications and Acceptable Means of Compliance for Large Aeroplanes CS-25.* Amendment 25. Federal Aviation Authority (2020)

[16] E. Torenbeek. *Synthesis of Subsonic Airplane Design.* Delft University Press, (1982), ISBN: 90-247-2724-3

[17] J. Roskam. *PART III: Layout Design Of Cockpit, Fuselage, Wing and Empennage: Cutaways and Inboard Profiles.* Roskam Aviation and Engineering Corporation, Ottowa (1986).

[18] G. Bourget, *The effect of landing-gear implementation on Flying V aerodynamics, stability and controllability* (2020), URL `http://resolver.tudelft.nl/uuid:599eca91-6200-4d29-8dd7-e4e7060703e1`

[19] Transport Airplane Directorate. *Advisory Circular 25.773-1 - Pilot Compartment View Design Considerations.* Federal Aviation Administration (1993).

[20] Honeywell. *IntuVue (RDR-4000) Weather Radar.* Retrieved December 01, 2020, from `https://aerospace.honeywell.com/en/learn/products/weather-radar/rdr-4000m`

[21] R.E. Bellman (1957) *Dynamic Programming.* Princeton University Press, Princeton

[22] R. Schmidt , M. Voigt, R. Mailach (2019) *Latin Hypercube Sampling-Based Monte Carlo Simulation: Extension of the Sample Size and Correlation Control.* In: Uncertainty Management for Robust Industrial Design in Aeronautics. Notes on Numerical Fluid Mechanics and Multidisciplinary Design, vol 140. Springer, Cham. `https://doi.org/10.1007/978-3-319-77767-2_17`

[23] Parapy. *Parapy: Knowledge Base Engineering Platform.* Retrieved December 02, 2020, from `https://www.parapy.nl/`

[24] D. Wagner, J.A. Birt, M. Snyder, J.P. Duncanson. *Human Factors Design Guide.* Federal Aviation Administration, Springfield, Virginia (1996).

[25] NASA. *Man-Systems Integration Standards* National Aeronautics and Space Administration. (1995) `https://msis.jsc.nasa.gov/`

[26] R. Goossens, C. Snijders and T. Fransen (2000). *Biomechanical analysis of the dimensions of pilot seats in civil aircraft.* Applied ergonomics. 31. 9-14. DOI: 10.1016/S0003-6870(99)00028-9.

[27] *Stanford University Unstructured (SU2).* Retrieved December 01, 2020, from `https://su2code.github.io/`

[28] D. P. Raymer. *Aircraft Design: A Conceptual Approach.* American Institute of Aeronautics and Astronautics, (2004), ISBN: 0-930403-51-7

[29] J. H. Ferziger, M. Perić, and R. L. Street, Computational Methods for Fluid Dynamics (2020), 4th ed., ISBN 9783319996912.

[30] J. Tu, G. H. Yeoh and C. Liu. *Computational Fluid Dynamics: A Practical Approach* (2019, 3rd Edition). Butterworth-Heinemann. ISBN: 978-0-08-101127-0

[31] Airbus. *A319/a320/a321 flightdeck and systems briefing for pilots.* Airbus (1998).